University of Windsor

Scholarship at UWindsor

2012

Development of A Restraint Device for Low Birth-weight Infants

Xilin Chen
University of Windsor

DEVELOPMENT OF A RESTRAINT DEVICE FOR LOW BIRTH-WEIGHT
INFANTS

by

Xilin Chen

A Thesis
Submitted to the Faculty of Graduate Studies
through
the Department of Mechanical Engineering
in Partial Fulfillment of the Requirements for
the Degree of Master of Applied Science at the
University of Windsor

Windsor, Ontario, Canada

2011

DEVELOPMENT OF A RESTRAINT DEVICE FOR LOW BIRTH-WEIGHT INFANTS

by

Xilin Chen

APPROVED BY:

_____

N. Zamani

Department of Mechanical, Automotive,

and Materials Engineering

_____

A. Snowdon

Odette School of Business

_____

W. Altenhof, Advisor

Department of Mechanical, Automotive,

and Materials Engineering

_____

C. Novak, Chair of Defense

Department of Mechanical, Automotive,

and Materials Engineering

DECLARATION OF ORIGINALITY

I hereby certify that I am the sole author of this thesis and that no part of this thesis has been published or submitted for publication.

I certify that, to the best of my knowledge, my thesis does not infringe upon anyone's copyright nor violate any proprietary rights and that any ideas, techniques, quotations, or any other material from the work of other people included in my thesis, published or otherwise, are fully acknowledged in accordance with the standard referencing practices. Furthermore, to the extent that I have included copyrighted material that surpasses the bounds of fair dealing within the meaning of the Canada Copyright Act, I certify that I have obtained a written permission from the copyright owner(s) to include such material(s) in my thesis and have included copies of such copyright clearances to my appendix.

I declare that this is a true copy of my thesis, including any final revisions, as approved by my thesis committee and the Graduate Studies office, and that this thesis has not been submitted for a higher degree to any other University or Institution.

ABSTRACT

This research focuses on the development of the restraint device for low birth-weight infants to reduce the risk for respiratory compromise without influencing the crash protection performance of a car seat. In-vehicle on-road experiments were conducted in this research in order to provide better kinematic data of daily driving conditions which infants might experience in vehicles. In addition to normal driving conditions, crash events were investigated during the development of the restrain device. A material parametric study was conducted to investigate the effect of three foam candidates. A foam material with high stiffness tended to reduce peak head accelerations and neck joint forces while it resulted in a second head contact with the restraint device. No significant differences were predicated in normal driving conditions among three foam material candidates due to the low acceleration levels. A restraint device geometry parametric study was conducted. Three different geometries of the preemie positioning device which resulted in different initial neck angles were investigated. Large neck angle position configuration was beneficial to reducing airway compromise at the cost of potential over-extension of neck in an event of frontal impact. The influence of the incorporation of the restraint device into regular child seat was investigated. The restraint device illustrated advantage in terms of preventing potential airway collapse for infants in a daily driving condition. The neck angles were generally maintained above 90 degrees under most of normal driving conditions. The device also showed improvement, approximately 55% reduction in HIC value, under a side impact event due to the addition of side support. It reduced the frontal impact protection due to the introduction of more material between the infant and the CRS.

DEDICATION

For my loving parents and brother without whose love, support and patience the completion of this thesis would not have been possible; and to all the people in my life who have encouraged me to achieve my Master's degree.

ACKNOWLEDGEMENTS

TABLE OF CONTENTS

LIST OF TABLES

LIST OF FIGURE

LIST OF ABBREVIATIONS

ASTM	American Society for Testing and Materials
ATD	Anthropomorphic Testing Devices
CMVSS	Canadian Motor Vehicle Safety Standards
CRABI	Child restraint AirBag Interaction
CRS	Child Restraint System
FMVSS	Federal Motor Vehicle Safety Standards
HIC	Head Injury Criteria
NICU	Neonatal Intensive Care Unit
PPD	Preemie Positioning Device
V&V	Verification and Validation

1. INTRODUCTION

Road traffic accidents are a major public health challenge. Motor vehicle crashes cost Canada 3067 lives, 30932 hospitalizations, 7738 permanent partial disabilities, and 760 permanent total disabilities [1]. These victims include the most vulnerable and valuable members of the society - children. Children are involved in great amount of road travelling due to the heavy use of automobiles as a mean of transportation in our society. In 2005, there were 103 deaths and 13649 injuries to children under the age of 14 due to automobile crashes [2]. When children become victims, families suffer both emotionally and financially.

The proper use of a child restraint system (CRS) can significantly reduce the chance that children sustain serve injuries. In a crash, the proper use of infant or child car seats can reduce the risk of death by 71% and the risk of injury by 67% [3, 4]. In 1990, the American Academy of Pediatrics recommended that all newborn infants discharged from hospitals should be transported in infant car safety seats [5, 6]. CRSs are extremely effective when correctly installed and used in passenger cars, reducing the risk of death by 71% for infants and 54% for children aged 1 to 4 years, and reducing the need for hospitalization by 69% for children aged 4 and under [7].

Compared with normal children, infants with special needs require more protection during the travelling. Those infants include preterm and low birth weight infants, who are at a higher risk of respiratory compromise. Premature infants are now widely recognized to be at a higher risk of oxygen desaturation and secondary central apnea while restrained in infant car seats [8, 9]. Preterm infants are subject to an increased risk of oxygen desaturation, apnea, and/or bradycardia, especially when placed in a semireclined position in car safety seats [10]. 12% to 30 % of premature infants have been reported to have episodes of desaturation and bradycardia while in car seats [8, 11-13]. Federal Motor Vehicle Safety Standard (FMVSS) 213 [14] and Canada Motor Vehicle Safety Standard (CMVSS) 213 [15] have established the performance and design standard of CRSs. The norms outline which class/stage of CRSs is suitable for the child

according to the size and weight of the child, using age as a guideline. However, some clinical reports [10] point out that the standard has no minimum weight limit and does not address the relative hypotonia and risk of airway obstruction in preterm or low birth weight infants. Most rear-facing car safety seats are designed by the manufacturer for use by infants weighing more than 4 or 5 lb. Studies by Bull et al [16] suggest that a car bed can be adapted to accommodate very small infants. The American Academy of Pediatrics in 1996 recommended that each preterm infant be monitored in a car safety seat before hospital discharge and that infants with documented desaturation, apnea, or bradycardia should travel in a supine or prone position in a car bed [17,18]. The recommendation is based on the assumption that a flat position provided by car bed is less likely for preemies to have episodes of oxygen desaturation and bradycardia. However, some studies [19, 6] suggest that there is no significant difference between car safety seats and car beds in term of respiratory physiologic features of infants. Additionally, car safety seats do provide much better protection during the event of vehicle collision than infant beds. According to Webber [3], in a car-bed restraint, the infant lies flat, preferably on its back or side, and the bed is placed on the vehicle seat, with its long axis perpendicular to the direction of travel and the baby's head toward the center of the vehicle. In a frontal crash, the forces are distributed along the entire side of the infant's body, while a harness or other containment device keeps the baby in place during rebound or rollover. In a side impact, however, the infants' head and neck are theoretically more vulnerable in a car bed than in a rear-facing restraint, especially if the impact is on the side nearest the head and there is significant intrusion.

The above mentioned statistics and issues show the significant demand of improvement and innovation of safety devices for infants with special needs. The purpose of this research project is to develop a safe restrain system which is suitable for low birth-weight infants, especially prematurely born children (preemies), for the purpose of both travelling and home use. The project was carried out by engineers, paediatricians, parents, and car seats manufacturers working in collaboration.

2. LITERATURE REVIEW

2.1 Statistics

Traffic related injuries and fatalities are major public health challenge nowadays. Traffic incidents result in not only the property lost, but also life lost, which includes our most valuable society members, children.

In 2004, transport incidents in Canada accounted for 3067 deaths, 30932 hospitalizations, 7738 permanent partial disability, and 760 permanent disabilities [1]. Health care costs and economic losses resulting from motor vehicle crashes totalled $3.7 billion in 2004 [1]. According to National Highway Traffic Safety Administration [20], every day in the United States, an average of 5 children age 14 and younger were killed and 568 were injured in motor vehicle crashes during 2006. Figure 2-1 illustrates the number of occupant fatalities (age 0-14) from 2002 to 2006 in Canada and the US. When considering the trend over the those five years (2003 – 2007), it can be stated that in Canada there has been no significant decrease in the number of child fatalities (13 percent drop from 2003 to 2007), while there was a 20 percent decrease in the US over this five-year period [21].

Road traffic accident related injuries result in heavy economic burdens to society. The direct and indirect costs of road traffic accidents are paid by the tax-payer everyday. Injuries, in general, cost Canadians $19.8 billion and 13,667 lives in 2004. During the year 2004 in Canada, traffic incidents were the third leading cause of overall injury costs, accounting for $3.7 billion or 19% of total cost of injury and economic losses. It was also the leading cause of indirect costs (the value lost to society as a result of the illness in question) of injury, accounting for $2.1 billion (23% of total indirect costs). In Ontario, motor vehicle incidents resulted in 400 deaths, 4805 hospitalizations, 1249 permanent partial disabilities, and 126 permanent total disabilities in 2004. These incidents brought heavy economic burden to every Ontarian with $599 million in total costs, including $280 million in direct costs (the value of resources used to treat the persons incurring the illness), and $319 million in indirect costs [1].
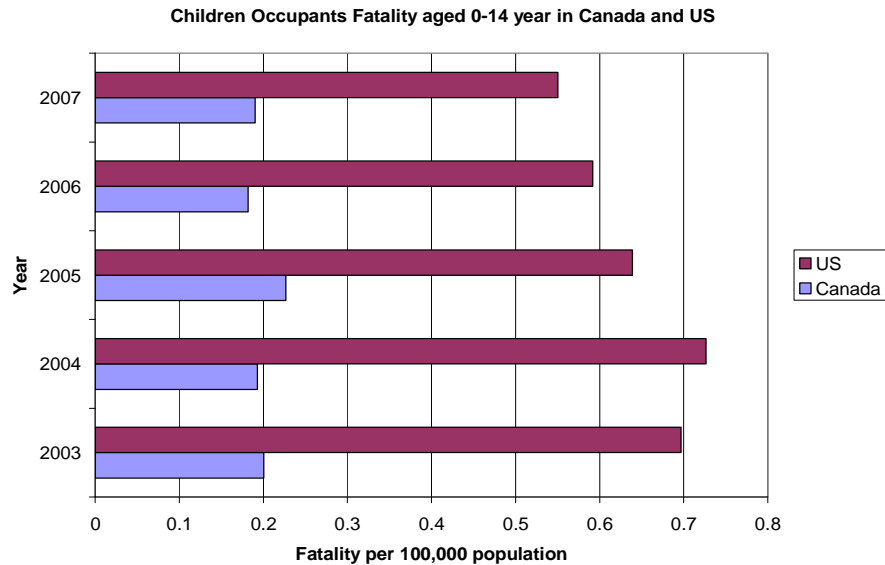
Figure 2-1. Occupant fatalities in Canada and the US per 100,000 population [21].

The vehicle safety has been improved significantly due to the use of advanced material, vehicle structural design, more strict regulation, and improved education level of drivers. However, the progress made in child safety has not been as significant as that made in adult passenger safety. This might be caused by the lack of knowledge on the injury mechanisms of children, and the biomechanical properties of this younger population. Since children are not just scaled version of the adults, special considerations are demanded when designing safety devices for children.

2.2 Low birth-weight infants' special needs

Low birth-weight infants require special considerations when travelling in vehicles. Improved survival rates and earlier discharge of preterm (less than37 weeks gestation at birth) and low birth weight (less than 2500 g at birth) infants have increased the number of small infants who are being transported in private vehicles [10]. The immaturity of the infants must be taken into consideration when positioning such infants.

The infant car seats play a critical role in the safe transportation of young infants and have reduced the rates of deaths and injuries during motor vehicle accidents [19]. However, there are limitations of those infant seats. Respiratory instability is a potential concern because of the upright position in the car seat. This is particularly true for premature newborns, which has resulted in the recommendation for car safety seat testing before discharge from the hospital for such infants [19]. Studies [24,25] show that mean oxygen saturation declined for both term and premature infants, reaching a nadir of 95% after approximately 70 minutes of placement in a car safety seat; 7% of infants were noted to have oxygen saturation values of less than 90% for over 30 minutes.

It is also mentioned in some reports [6] that 12% to 30% of premature infants have been reported to have episodes of desaturation and bradycardia while in car safety seats. The misuse of the child car seats tends to increase the risks of cardio-respiratory instability to infants. The child car seats are expected to use only when necessary, like transportation in vehicles. However, many parents use them as accommodation devices. It is mentioned [19] that the portability of car seats and busy contemporary lifestyles are resulting in infants spending extended periods of time in car seat for reasons other than transports. Of 187 infants, 94% spent over 30 minutes in seating devices (including car seats) every day. The mean time spent in seating devices was 5.7 ± 3.5 hours (range:0-16 hours). Prolonged use of car seats by infants too young to sit unsupported also may result in prolonged periods of oxygen desaturation. According to Tonkin et al.[24], premature infants are now widely recognized to be at high risk of oxygen desaturation and secondary central apnea while restrained in infant car seats. Despite use of rear facing, reclining car seats, up to 30% of premature infants may fail a car seat test, which is recommended by the American Academy of Pediatrics. Figure 2-2 and 2-3 illustrate the car seat testing results obtained at McMaster University. The figure shows the oxygen level of infants during the stay in the car seat.
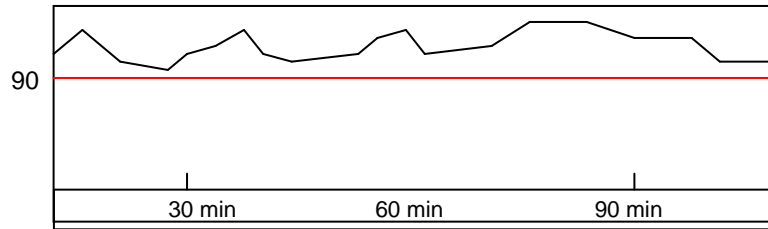
Figure 2-2. Pass: Infants oxygen saturation levels maintained above 90 during 1.5 hour in-hospital car seat evaluation.
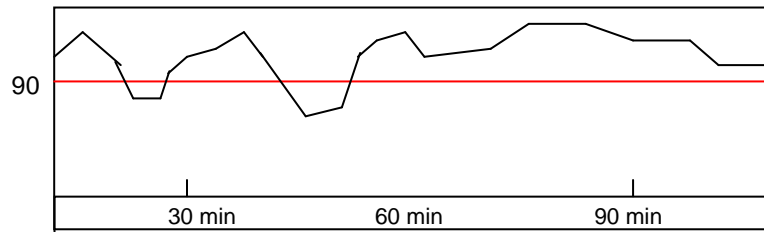
Figure 2-3. Failure: Infants oxygen saturation levels drop below 90 twice during 1.5 hour evaluation.

Researchers investigated the causes that infants are at high risk of oxygen desaturation when placing in upright position. Stark and Thach [25] reported that small, preterm infants are vulnerable to hypoxia and apnea when their neck is flexed either by external pressure or spontaneously. They found that infants were particularly prone to head flexion when the infant had been placed in a more upright position. Wilson et al. [26] determined the influence of transmural pressure and neck posture on upper airway patency in infants after death. They collected nine infants whose masses were from 760 to 3,500 g. Figure 2-4 [26] illustrates the experiments diagram of the system utilized to measure post-mortem airway closing and opening pressures. They found that neck flexion raised closing pressure, making the airway more susceptible to collapse, whereas neck extension lowered closing pressure, making the airway more resistant to collapse. Closing pressure is plotted against degree of neck flexion or extension in Figure 2-5 [26]. Pressures above the corresponding closing pressure were required to reopen the closed airway, suggesting that the walls of the closed airway tended to adhere and implying that surface forces can impose an added load to airway-maintaining musculature during obstructive apnea in the living infants [26].
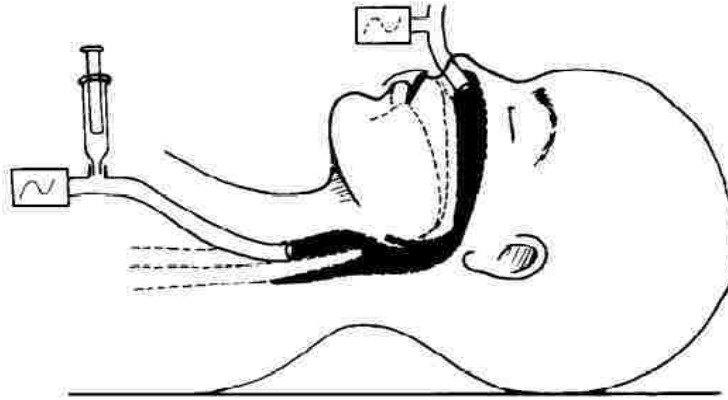
Figure 2-4 [26]. Post-mortem airway closing and opening pressures experiment scheme.
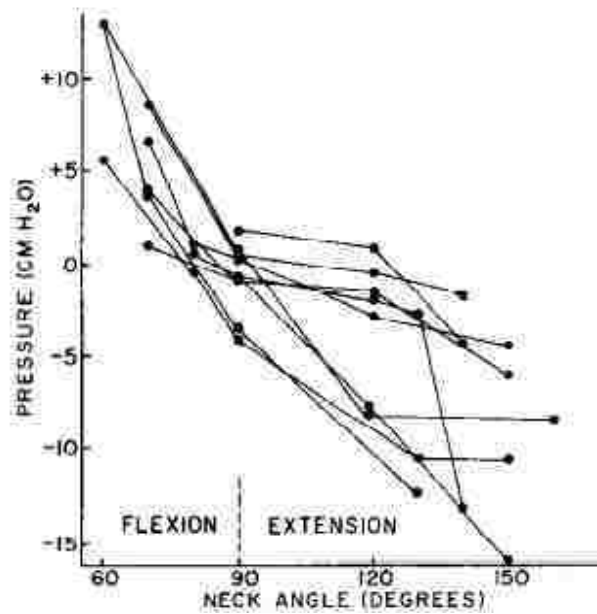
Figure 2-5 [26]. Airway closing pressure versus neck angle curves.

Kinane et al. also indicated in [19] that the hypoxia while in the car safety seat is most likely attributable to the relative vulnerability of the airway in premature and term infants. The cause of the airway narrowing is slouching of the head forward while the infant is asleep in the car seat, which results in closure of the mouth, pressing of the tongue against the posterior pharynx, and flexion of the airway.

Some [6] suggest that a car bed can be adapted to accommodate very small infants. In the report, it mentioned that the American Academy of Pediatrics in 1996 recommended that each preterm infant be monitored in a car safety seat before hospital

discharge and that infants with documented desaturation, apnea, or bradycardia should travel in a supine or prone position in a car bed. This recommendation is based on an assumption that these events are less likely in a car bed than in a car seat. However, some researchers did find that car beds do not necessarily have an advantage over child car seats in term of preventing hypoxia. Kinane et al. [19] recruited 67 healthy term infants and assigned random monitoring in either a car bed or a car safety seat. Physiologic data, including oxygen saturation and frequency and type of apnea, were obtained and analyzed in a blinded manner. They concluded that the respiratory physiologic features of infants in the 2 car safety devices were observed to be similar. They indicated that it is possible that the desaturation is attributable to a cause other than airway closure. The tensioned harness may contribute to the vulnerability to desaturation. It was also mentioned that it is possible that compression on the abdomen is a factor contributing to respiratory compromise.

Some researchers seek methods to solve the respiratory compromise issue when infants, especially preterm infants, are placed in a more upright position. Tonkin et al. [24] conducted a research study regarding a simple car seat insert to prevent upper airway narrowing in preterm infants. The hypothesis was that an infant car seat modification to allow the infant's head to rest in a neutral position on the trunk would prevent narrowing of the upper airway and thus reduce oxygen desaturation in preterm infants who are restrained in car seats. Figure 2-6 [24] illustrates the infant car seat modification. A simple H-shape foam insert, which was 2.5 cm thick, was added to the seat.

Figure 2-6. Simple insert in infant car seat [24].

A total of 17 infants, born at 32.0 ± 3.5 weeks, weighting 1792 ± 599 g, were studied. The report [24] states that with the insert in place, all infants were able to maintain their head in a neutral position. When the insert was removed, in the majority of infants, the head tended to slump forward, with the chin pressed on the chest. Figure 2-7 [24] illustrates the infant posture with and without the insert in place.

(a) **(b)**

Figure 2-7. Infant placed in car seat (a) with insert; (b) without insert [24].

9

Respiration timed radiographs for assessment of upper airway dimensions were taken during quite sleep in each position. Infants were monitored in each position for 30 minutes with continuous polygraphic recoding of respiratory, cardiac, and nasal airflow activity and pulse oximetry [24]. Placement of the insert was observed to be associated with a larger upper airway space, reduction in the frequency of episodes of oxygen desaturation, of bradycardia, and of arousal [24]. Figure 2-8 [24] illustrates the radiographs of infant's airway with and without the foam insert in place. Figure 2-9 [24] illustrates the airway size comparisons at various locations (MAS to PAS). The detailed results were tabulated in Table 2-1 [24].

(a)   **(b)**
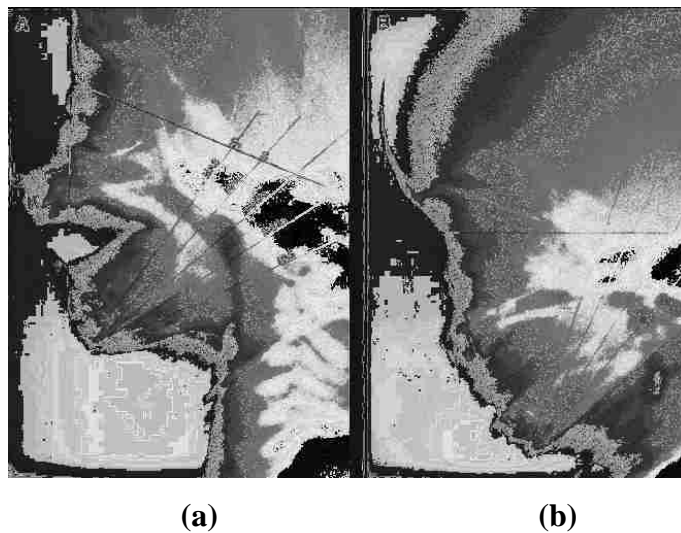
Figure 2-8. Example of respiration timed radiographs: (a) with simple insert; (b) without insert [24].
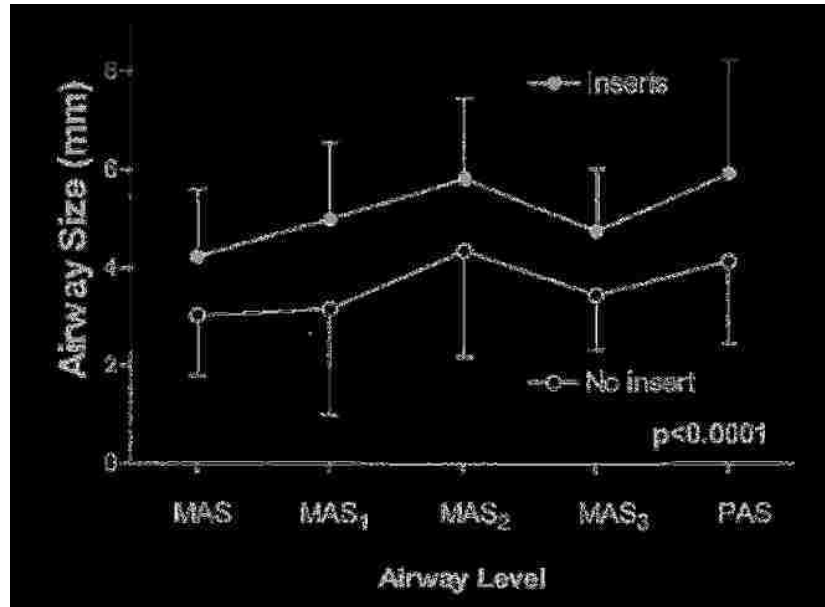
Figure 2-9. Airway measurements with and without the foam insert [24].

	CRS ONLY	CRS with the simple INSERT
Upper airway space (mm)	3.6 ±1.4	5.2±1.3
Frequency of oxygen desaturation [<85%] (epidodes/infant)	3.5 ±3.5	1.5 ±2.1
Frequency of bradycardia [<90 bpm] (episodes/infant)	1 ±1.7	0.1 ±0.3

Table 2-1. Simple insert car seat experiment results [24].

2.3 Anthropomorphic Testing Devices

Anthropomorphic Testing Devices (ATDs) are mechanical surrogates designed to be biofiedelic (they mimic pertinent human physical characteristics including size, shape, mass, stiffness, and energy absorption/dissipation) [27]. They are classified according to size, age, gender, and impact direction. Due to the ethical issues, the biomechanical properties of human beings are rarely obtained. Currently, the properties of human tissues are obtained from animals, cadavers, and research from real world crashes.

11

The Hybrid III ATD was designed to mimic human responses for forehead impacts, neck extension and flexion, distributed sternal impacts, and knee impacts [27]. The head consists of a hollow, cast aluminium shell of uniform thickness covered by vinyl skin. The thickness of the skin gives human-like head accelerations during forehead impacts. The neck consists of rubber segments bonded to aluminium disks. A braided cable attached to end plates passes through the center of the neck. The top end plate is linked to the head with a single pivot joint to represent the atlanto-occipital joint in humans. This neck mimics human neck bending responses for flexion, extension, and lateral bending [27].

The chest of the Hybrid III consists of six steel ribs linked on one end to a leather component that represents the sternum. On the other end the ribs connect to the spine. Dampening material is bonded to the inside of each rib to mimic the energy dissipation of the human thorax. The ribs are sized to mimic the sternal force-deflection response of the human thorax [27].

The Hybrid III 3 Year Old child dummy is often used to assess car seat performance and injury risks. The dummy design was based on a combination of the 3-year-old "Air Bag" dummy, scaled-down version of the Hybrid III 50th percentile male and scaled-up versions of the CRABI (Child Restraint AirBag Interaction) dummy [27].

The Q-series dummy family is mainly used in Europe. Specific design features of the Q-dummies include: anatomical representation of body regions, use of advanced materials, dummy-interchangeable instrumentation, multi-directional use (front & side impact) and easy handling properties (limited components, easy assembly/dis-assembly, and simple calibration) [28]. The Q0 represents a 6 week old infant weighing 7.5 lbs with a sitting height of 14 inches. It was designed for frontal, side, rear, and roll over crash configurations and allows for the measurement of head chest, and pelvis accelerations as well as upper neck forces and moments. The neck (cervical spine) is a series of rubber and metal disks connected at one end to the head which consists of a hard plastic covered with vinyl skin [48].

2.4 Validation techniques

Verification and validation (V&V) are the primary means to assess accuracy and reliability in computational simulations [32]. The method proposed by Oberkampf and Trucano [32] appears to be quite thorough and provides a validation metric as a function of relative error. The validation metric (*V*) is calculated as presented in Equation as shown below.

$$V = 1 - \frac{1}{L} \int_0^L \tanh \left| \frac{y(x) - Y(x)}{Y(x)} \right| dx$$

Where *y(x)* is the measured value, *Y(x)* is the expected value and L is the range of the independent variable. The advantages of using the Oberkamf and Trucano's scheme [32] are as follows. This validation metric normalizes the difference between the computational results and the experimental data. Secondly, the absolute value of the relative error only permits the difference between the computational results and the experimental data to accumulate, therefore positive and negative differences cannot offset one another. Thirdly, when the difference between the computational results and the experimental data is zero at all measurement locations, then the validation metric is unity, therefore perfect agreement between the computational results and the experimental data. In addition, when the summation of the relative error becomes large, the validation metric approaches zero [32].

3. FOCUS OF RESEARCH

The literature studies have shown that the motor vehicle collisions cost tremendous amount of lives of children and millions of dollars every year. The child restraint systems have been proved that they can provide proper protection to children and reduce the risk of death and serve injuries to children.

With the increase of the survival rates and earlier discharge of preterm (less than 37 weeks gestation at birth) and low birth weight (less than 2500 g at birth) infants, the number of infants who are being transported in private vehicles [5] has risen as well. Although child seats manufactures have labelled the proper user group of their products and the seats are tested accordingly, there are no suitable child seats available for low birth-weight infant currently. Most car safety seats are designated by the manufacturer for use by infants weighting more than 4 or 5 lbf, while others are designated for newborns regardless of their weight [5].

Although extensive experimental and numerical studies have been done on the child safety seats utilizing dummy models, few are focused on the preemies/low birth-weight safety during the travelling probably due to the lack of biomechanical knowledge of preemies and the small population. However, these infants require special treatment during transportation. Preemies are at a higher risk of oxygen desaturation, apnea, and/or bradycardia in a semi-recline position. Moreover, their weak neck muscle provides almost no resistance to any disturbance when their head are subject to any external acceleration. Most low birth-weight infants, even full term infants, can not hold their hand straight up for certain period of time. All of these facts put preemies in an unstable state in car safety seats.

This research will utilize numerical analysis to develop low birth- weight infants or preemie positioning device (PPD) to provide protection in terms of respiratory stability without compromising crash protection from car seats. A fully deformable child safety seat was be utilized in the numerical analysis. A low-birth weight infant finite element

model was developed along with the design of the device by another Master's candidate, Matthew J. Bondy.

Based on the lack of proper restraint and protection devices for these special infants (low-birth weight infants), the research will focus on the following areas:

1) To develop a restraint device for low birth-weight to reduce respiratory issues in two different scenarios: normal driving and crash. The device is expected to assist infants maintain respiratory stability while seated in CRS.

2) To conduct a material parametric study to investigate various foam materials for the insert. In collaboration with industry partners, prototypes are expected to be manufactured. The design iteration will be performed numerically. The selection of the foam material will be based on the numerical results.

3) To investigate influence of different PPD geometric. A PPD geometrical parametric study will be conducted. Various scenarios will be simulated to investigate the PPD performance.

4) To investigate the effectiveness of the PPD on the crash protection performance of the CRS. The PPD is expected to reduce the respiratory compromising issues without the cost of crash protection performance. The results in the presence and absence of the PPD will be compared.

4. IN-VEHICLE EXPERIMENT

In-vehicle on-road tests were performed to assess typical accelerations that CRS experienced under various normal driving conditions. The obtained accelerations were implemented into numerical simulations to assess the PPD. Four scenarios that infant passengers will encounter during the travelling in vehicle were created and performed: sudden stop, roundabout turning, speed bumps, and sharp-turn driving conditions. The testing was performed locally in Windsor, Ontario, Canada, under a safe condition. This chapter describes the details of the experiment procedures and data analysis.

4.1 Experiment set-up

The experiment was performed in a Ford Freestar SEL mini-van. According to the manufacturer, the gross weight, length, width, and height of the vehicle is 2,658 kg, 5,105 mm, 1,946 mm, and 1,748 mm. Figure 4-1 illustrates the vehicle in the test field.

Figure 4-1. The test vehicle in test field.

Two CRSs were utilized to measure and compare the accelerations exerted by external disturbances. One was the Evenflow infant seat, and the other was the Graco convertible safety seat as shown in Figure 4-2. Both seats were set up in the vehicle in rear-facing configurations. The seats were positioned with the presence of a roll of towel, which assisted in keeping the seats in an acceptable inclination level. The inclination meter, as shown in Figure 4-2, assured that the child seat was installed properly. The foam covers were removed for both seats for the purpose of easy access to the installation of measuring instruments. It was assumed that the foam covers of CRS had negligible influence on the results.

(a)   **(b)**
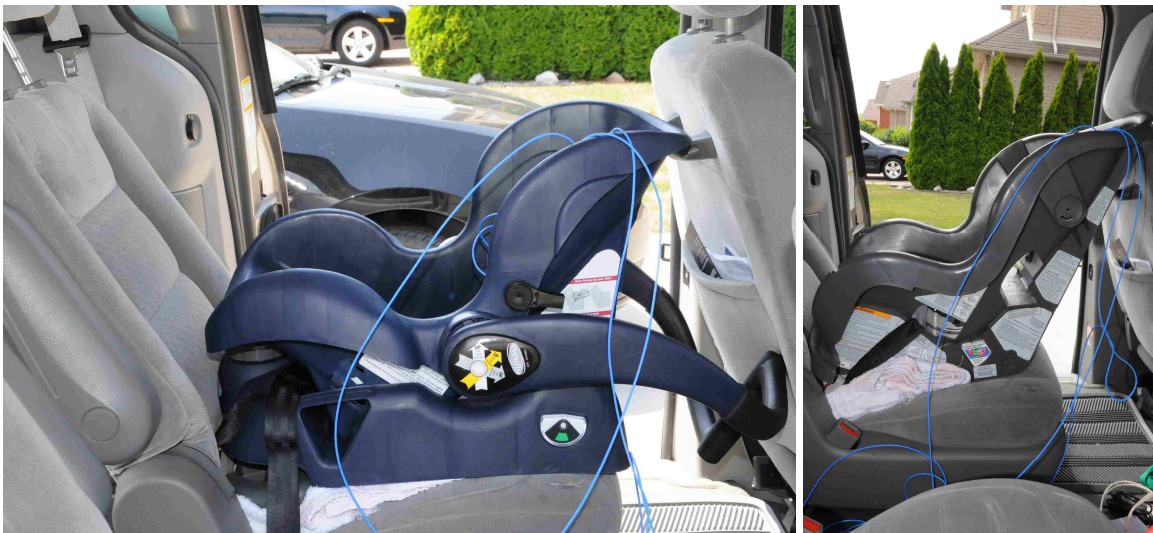
Figure 4-2. (a) Evenflow infant seat, and (b) Graco convertible.

Three accelerometers were attached on a metal cube, which was mounted on the back of the CRS. The accelerometers were orientated according to SAE J211 norm as shown in Figure 4-3. The data acquisition system consists of one Hi-speed USB carrier NI USB-9162 which carries NI 9215 with BNC, 4-ch ± 10 V. The measured data was recorded in Labview on a Dell workstation. The sampling rate was 5 kHz. Figure 4-4 illustrates the data acquisition system setup with Graco convertible seat. The accelerometers utilized were PCB MEMS based accelerometers [41]. This MEMS DC Accelerometers were suitable to perform ride quality assessments of elevators, automobiles, trains, and amusement park rides.

Figure 4-3. The orientation of the accelerometer accordance to SAE J211 standard.
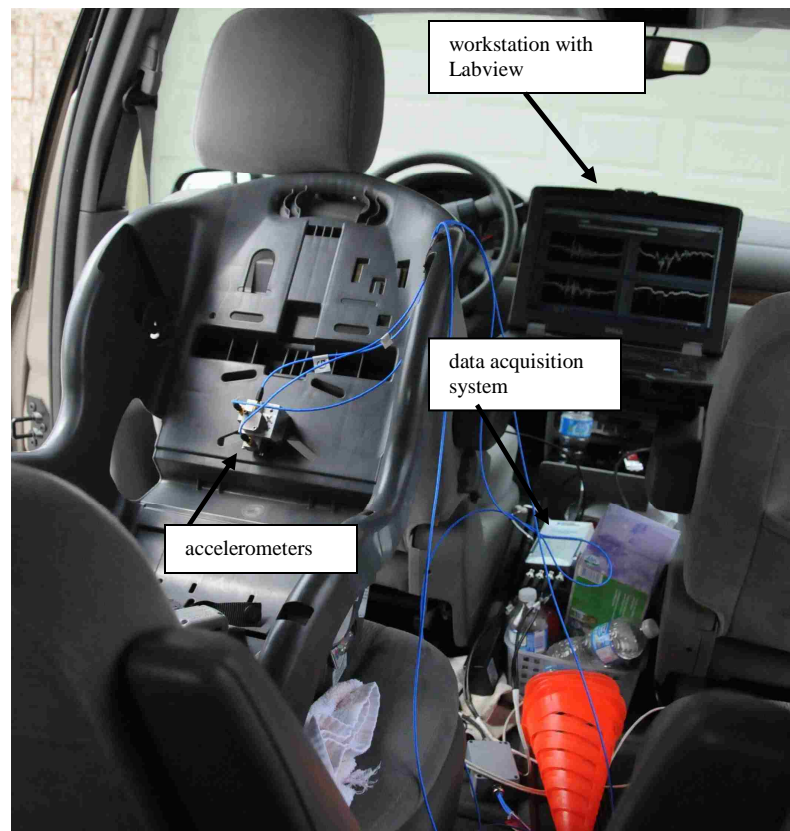
Figure 4-4. Data acquisition system setup with Graco convertible seat.

4.2 Experiment event

Four different driving conditions were selected as potential scenarios to be utilized into numerical simulations. Those four scenarios were referred to as braking, roundabout turning, speed bump, and sharp-turn conditions. All scenarios were conducted three times for each CRS.

4.2.1 Braking event

Braking was intended to simulate a scenario of sudden stop. The initial vehicle speed was approximately 40 km/h, and then full brake load was applied. The recording of the acceleration pulses started prior to the application of the brake, and ended when the vehicle came to a full stop. The distance for the vehicle to come to a full stop was measured. Three runs were carried out with each child seat. Table 4-1 tabulates the braking distance for each run. The average braking distance was approximately 10.5 meters.

Case CRS	Braking distance [m]				Average acceleration (g's)
	Run1	Run2	Run3	Average	
Evenflow	9.83	11.23	10.97	10.68	0.59
Graco	9.55	10.49	11.18	10.40	0.60

Table 4-1. Braking distance for each run.

4.2.2 Roundabout turning event

A roundabout turning provides a relatively constant lateral acceleration. The driving speed was approximately 25 km/h in the roundabout. The radius of the roundabout is approximately 8 meters. Therefore, the lateral acceleration was calculated to be approximately 0.61 g's. The recording of the accelerations started prior to the entering of the roundabout, and ended at the exit.

4.2.3 Sharp-turn event

A sharp-turn driving condition was expected to be relatively aggressive driving. The speed of the vehicle entering the corner was controlled at approximately 30 km/h, and exiting speed approximately 20 km/h. The recording of the accelerations started prior to the start of the turn and ended after the vehicle came to rest after the turn. The turn also involved a small ramp. It was expected that the acceleration from this event would be observed in all three directions.

4.2.4 Speed bump event

A speed bump driving condition was tested in a parking lot. The vehicle went over three speed bumps in a row at a speed of 25 km/h. Overall, the measured accelerations were not significant compared with other driving conditions. Thus, this event was not considered.

4.3 Data analysis

To implement measured acceleration pulses into the numerical models, a series of data analysis was required to make the data feasible for the application. The data aftertreatment consisted of data filtering, sample data selection, curve smoothing, and numerical model creation. All the procedures listed above were aimed to convert the raw data into an appropriate form for numerical analysis while the basic phenomenon was

preserved. Figure 4-5 illustrates the flow chart of the entire in-vehicle on-road test data aftertreatment process. The following sections describe the details of each step.

Raw data

- Filter data based upon SAEJ211 norms

Data set 1

- Find initial average acceleration & offset data in acceleration domain

Data set 2

- Consistency check among different runs under identical testing conditions
- Compare Evenflow & Graco seat
- Select sample data of representative for a give testing condition

Data set 3

- Apply Matcad smooth algorithm to representative data sets
- Create piece-wise linear data points to represent the acceleration pulse

Data set 4

- Check velocity and displacement using validation metric

Final data

Figure 4-5. In-vehicle on-road test data treatment flowchart.

Figure 4-6 illustrates the raw data of the braking scenario with the Graco convertible seat. High frequency signals were observed. The y-axis represents acceleration in unit of gravity [g's], and the x-axis represents time in seconds. The raw acceleration data were shifted in time domain so that the all events had same starting time. The major acceleration components were expected to be in the horizontal direction,

21

which is the vehicle travelling direction. Due to the orientation of the accelerometer, the horizontal acceleration was the resultant of the accelerations in x-direction and in z-direction. As expected, the acceleration in y-direction, whose magnitude was fluctuating between 0 to 0.2 g's, was noticed to be relatively small and negligible comparing to the other two components. For the braking event, only accelerations in x- and z-direction were preceded.
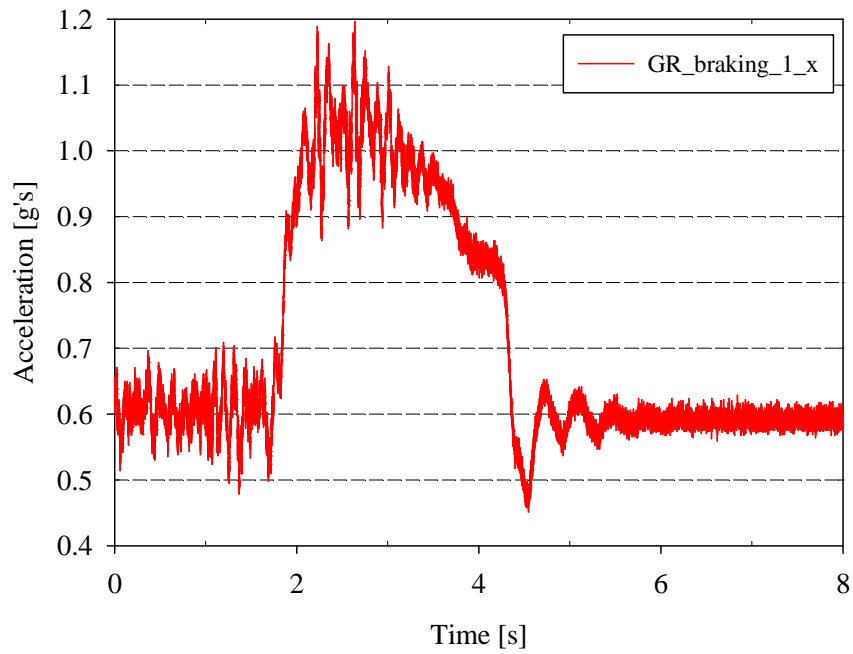
(a)
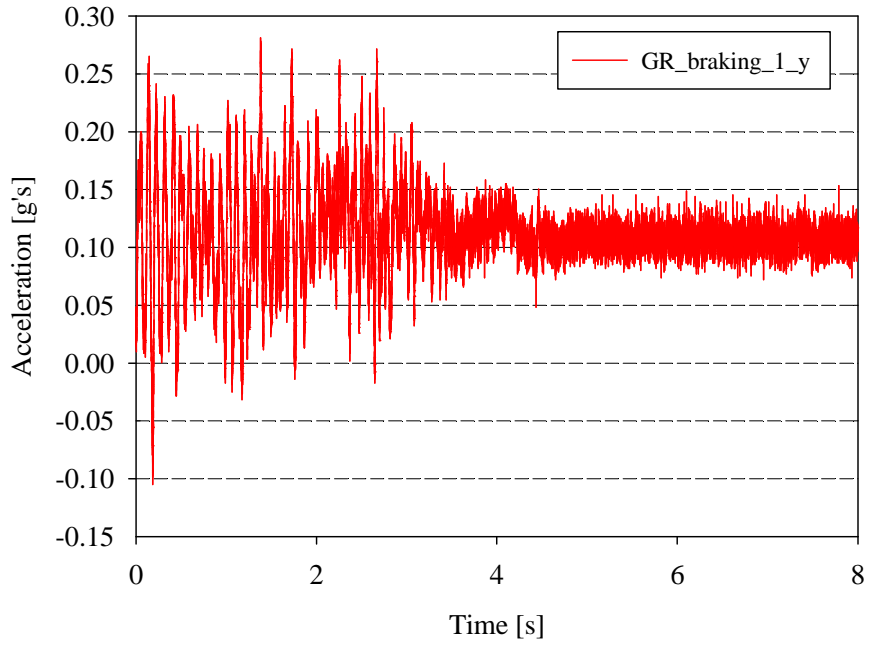
(b)
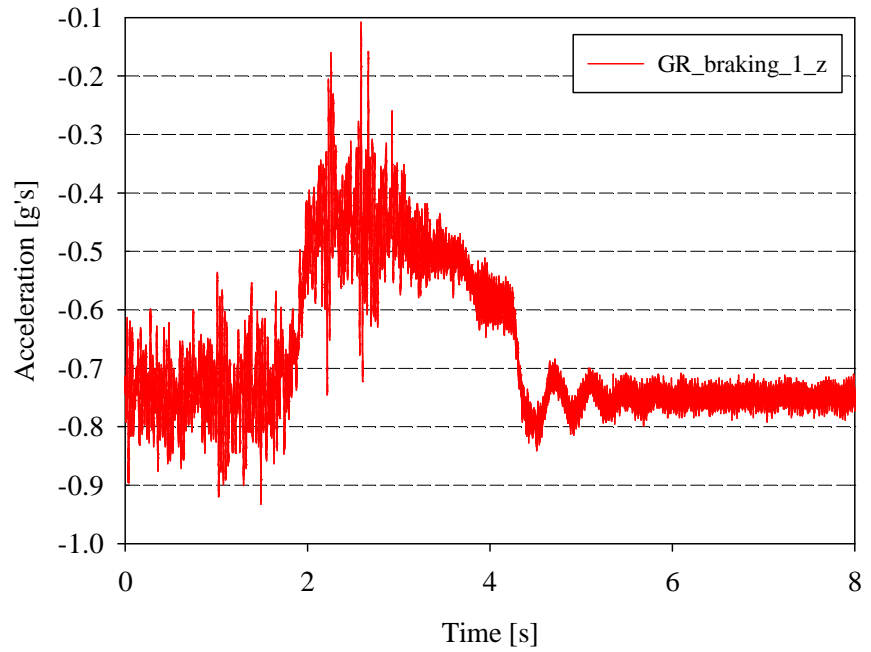
(c)

Figure 4-6. The measured accelerations for Graco seat during braking event (a) x-component, (b) y-component, and (c) z-component.

23

The data were filtered utilizing SAE J211 filter with 60 Hz cut-off frequency. Figure 4-7 illustrates the raw data and filtered data. The data were offset in both time domain, and acceleration domain to align them in the way that each acceleration pulse started at the same time with zero g's. The difference in the starting time was due to the various recording starting timing. The non-zero initial acceleration was due to the small vibration during the travelling. Figure 4-8 illustrates the initial offset value for each direction. The average accelerations when the vehicle was stationary before and after the tests were calculated as the offset value. The data from three runs were compared and one representative was selected.

(a)
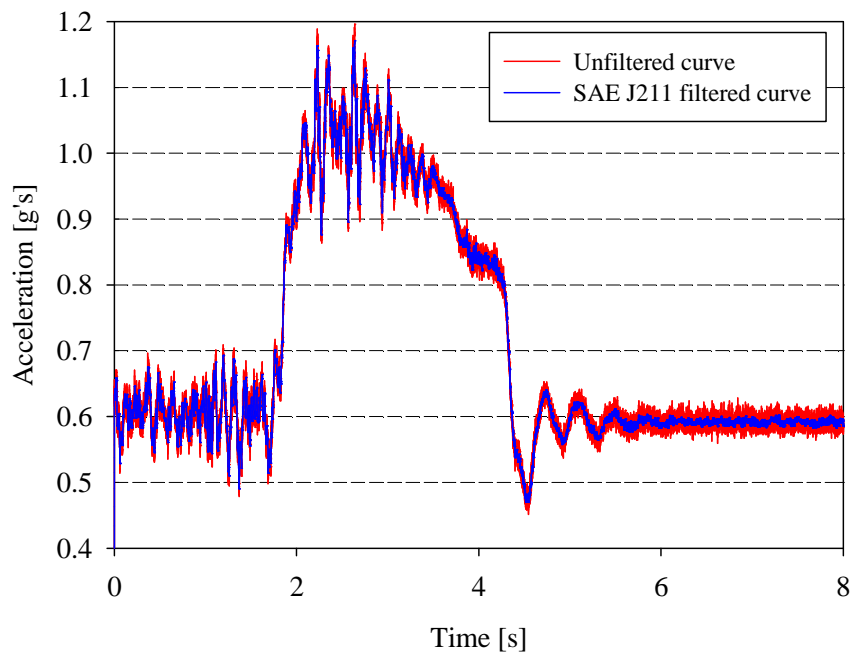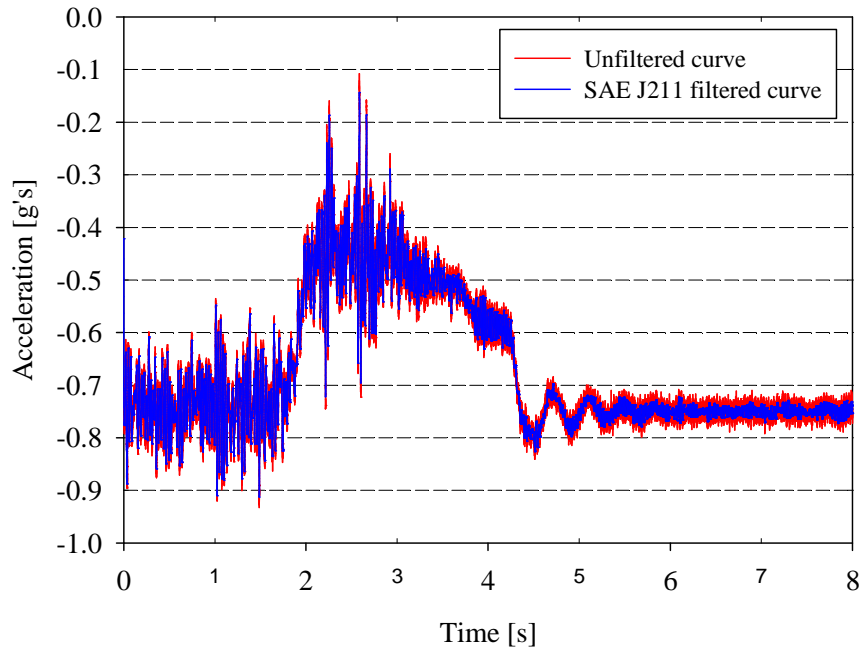
Figure 4-7. The filtered data curves (a) x-component, (b) z-component.

(a)
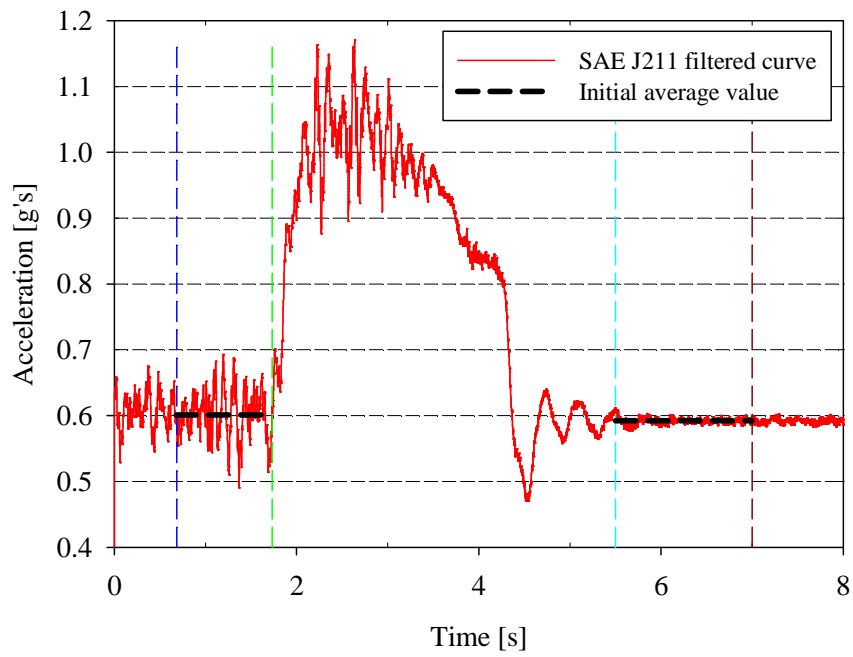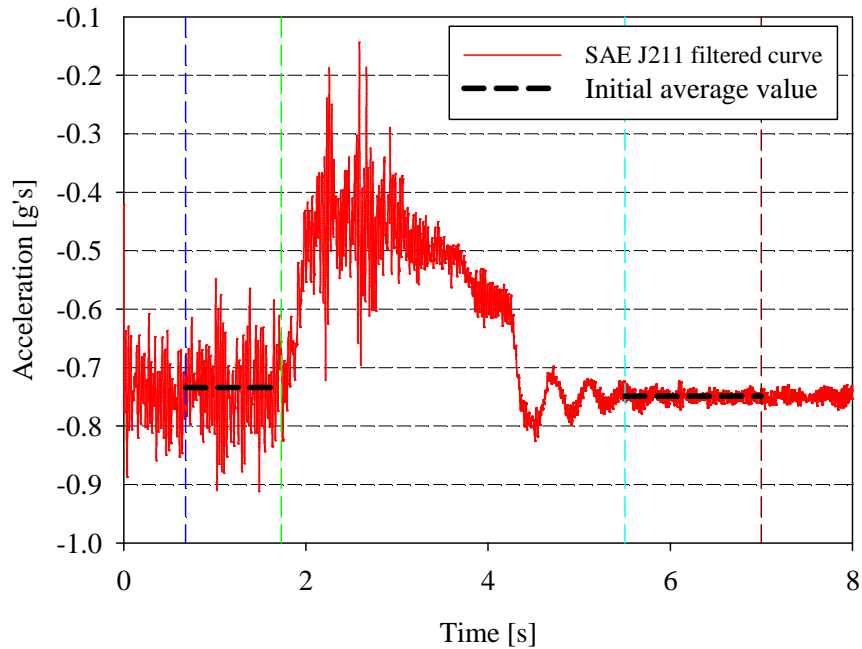
Figure 4-8. The obtaining of initial acceleration offset values.

These accelerations describe the kinematic characteristics which the CRS experienced in various scenarios. These events usually elapsed over 2 to 4 seconds. Due to this fact, unlike a crash acceleration pulse, the global phenomena were more important in this application, rather than capturing high frequency behaviour. Moreover, to have a reasonable size of input to the numerical model, a further data smoothing and reducing was required. The median smooth function with window size of 1000 data points in Mathcad [39] was utilized to further smooth the curve. According to Mathcad manual, Medsmooth is moving window smoothing, using a symmetric window. But rather than using a mean or a polynomial fit it uses a median as the smoothed value. Median smoothing is particularly useful in cases where there are sudden high frequency responses or incidents of corruption in the data. Figure 4-9 illustrates the smoothed and unsmoothed data curve for braking events with Graco convertible seat. Fifteen points were selected on the smoothed curve as input data for later numerical simulations applications.
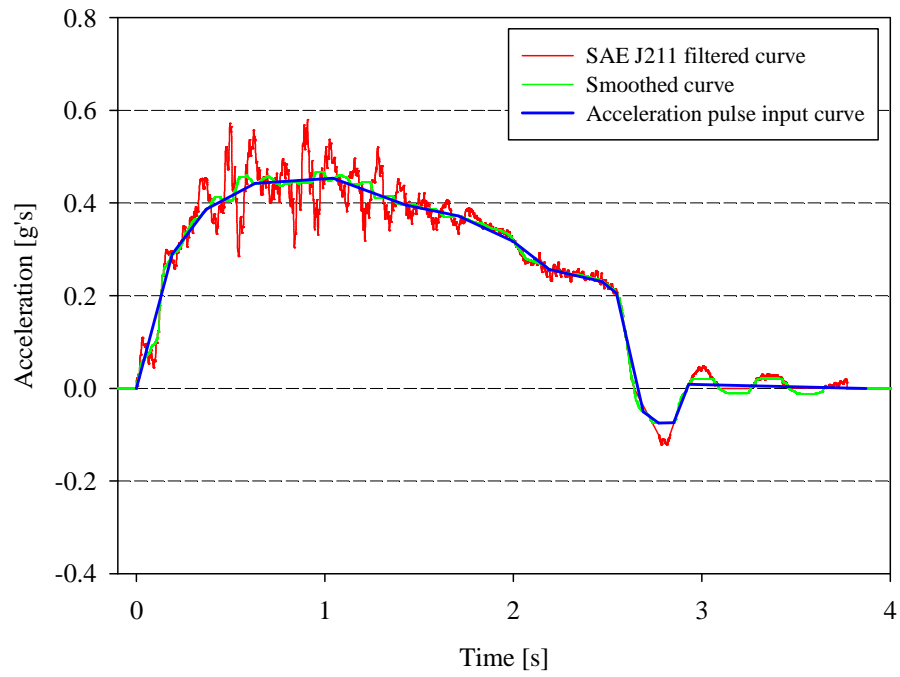
(a)
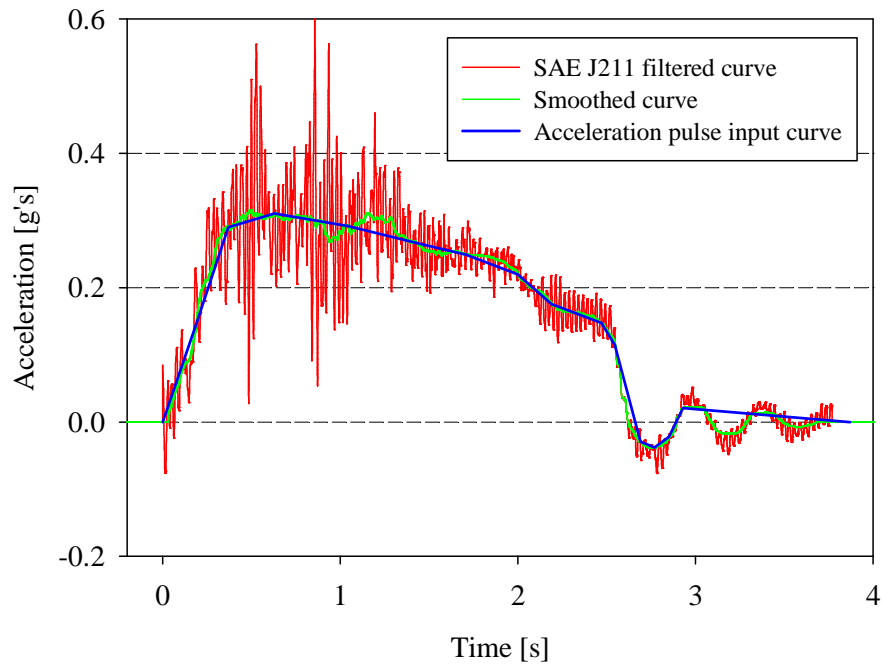
(b)

Figure 4-9. The final breaking event numerical simulation acceleration pulse (a) x-component, (b) z-component.

To ensure the final data preserved basic phenomenon of the real test results, the integrated results, and double integrated results, which are velocity, and displacement, respectively were calculated. Figure 4-10 and Figure 4-11 illustrates the comparison of velocity, and displacement curves based on filtered curve and acceleration pulse input curve for braking event, respectively. The validation metrics of the velocity data were calculated for braking scenario to be 0.987 and 0.979 in x-direction and z-direction, respectively. The validation metrics of the displacement data were 0.991 and 0.985 in x-direction and z-direction, respectively. The validation metrics results showed good agreements between the raw data and the final data sets which would be implemented into later simulations. Validation metrics were implemented to validate the final acceleration pulse input curve for all other scenarios. The results for all three events are tabulated in Table B-1 in Appendix B. The final curves which were implemented in the numerical simulation of roundabout, and sharp-turn events are illustrated in Figure B-1 and Figure B-2 in Appendix B, respectively.
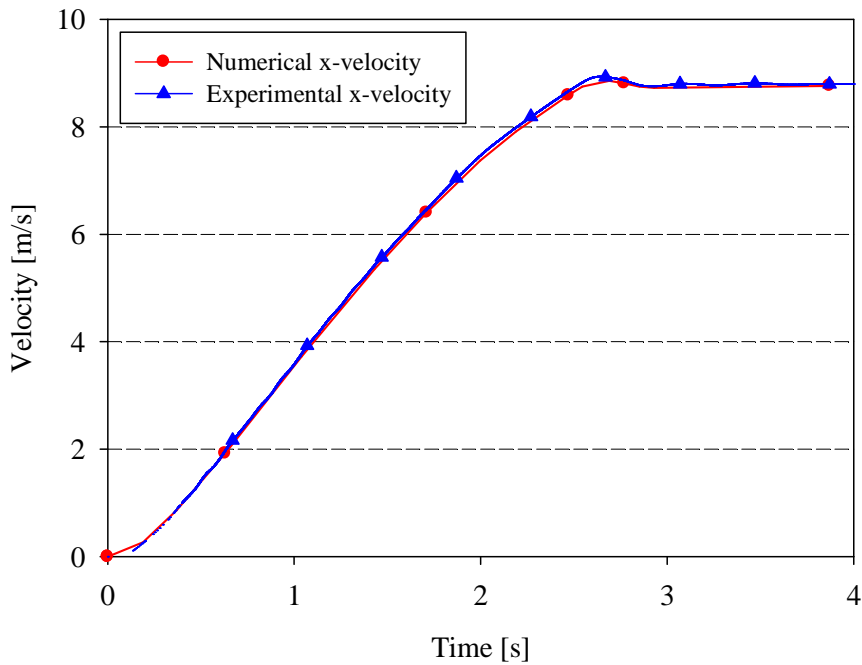
(a)
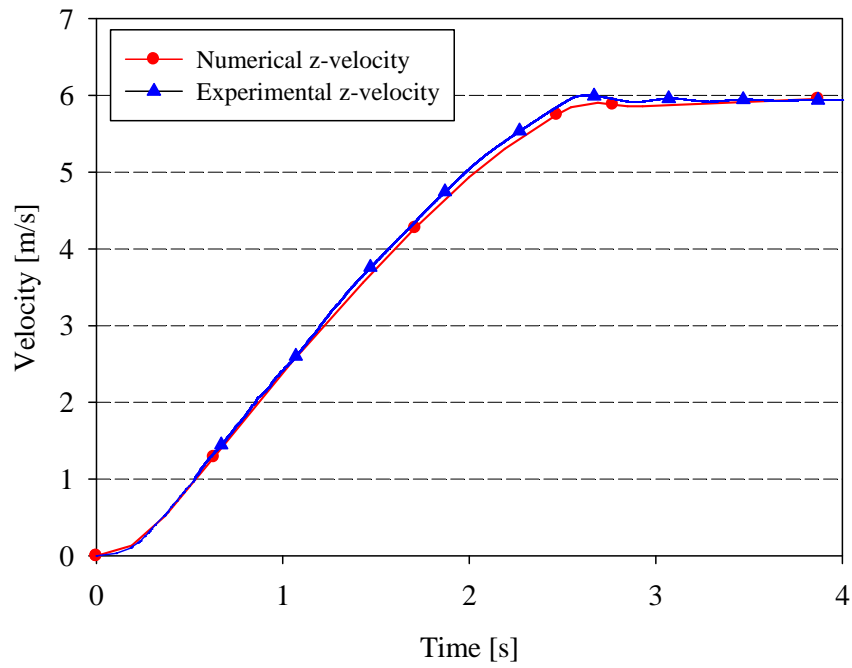
(b)

Figure 4-10. The velocity curves comparison for braking event with Graco convertible seat (a) x-component, (b) z-component.

(a)
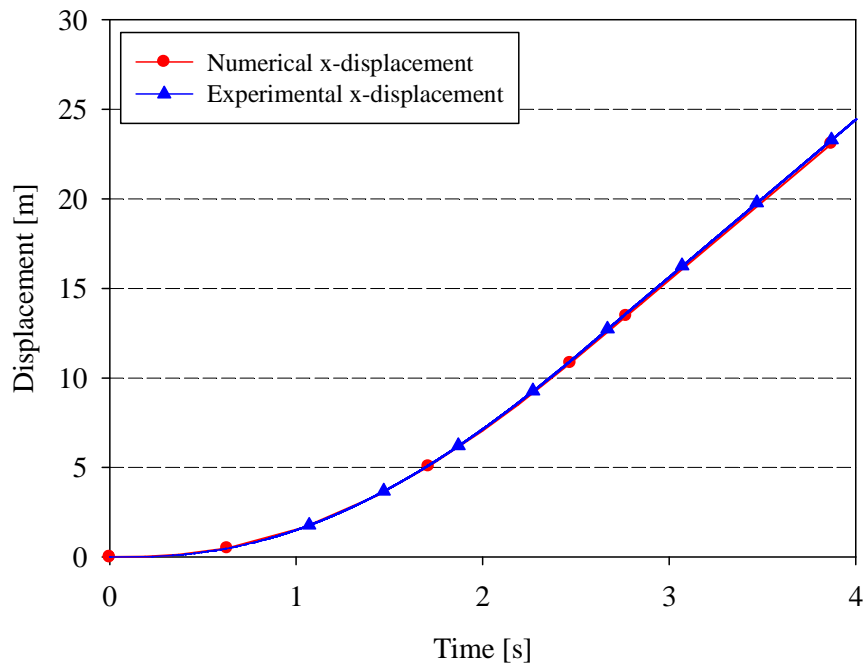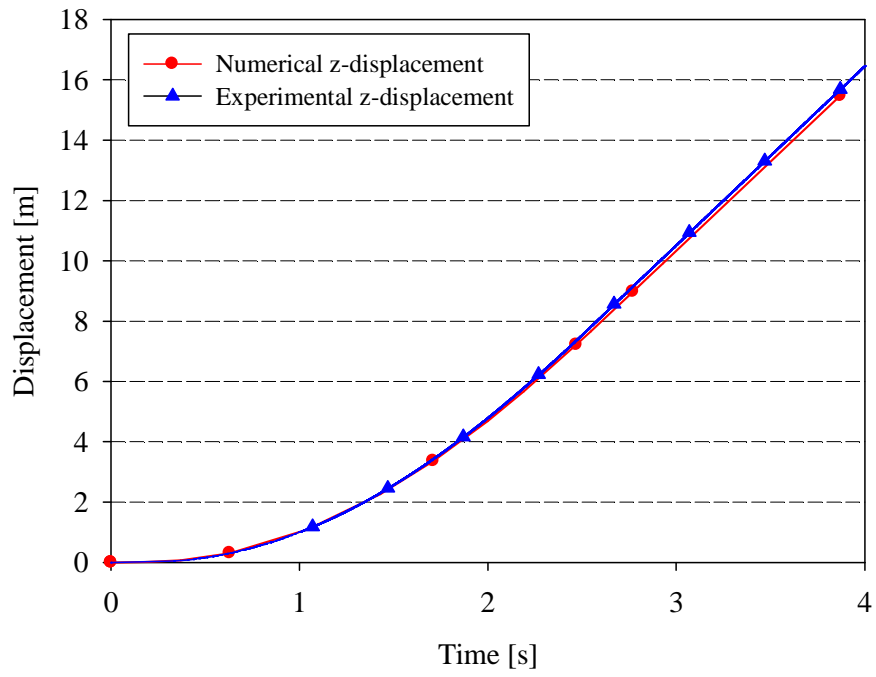
Figure 4-11. The displacement curves comparison for braking event with Graco convertible seat (a) x-component, (b) z-component.

5 NUMERICAL MODEL DEVELOPMENT

5.1 Deformable CRS

The deformable finite element child seat model was originally developed and validated by Kapoor et al. [29]. The child seat was modeled using surfaces provided by Century/Graco Corp. The determination of mechanical characteristics of the CRS polypropylene material was completed by the tensile tests in accordance with American Society for Testing and Materials (ASTM) D638 [30]. Figure 5-1 [29] illustrates a numerical and actual CRS.

(a)　　　　　　　**(b)**

(c)　　　　　　　**(d)**

Figure 5-1. Front (a) numerical and (b) actual; Rear (c) numerical and (d) actual view of the deformable Child Restraint System (CRS) [29].

5.2 PPD model

A CAD model of the PPD was based on the finite element model of the deformable CRS described above. The PPD geometry was designed and created with the assistance of the CRS and infant dummy CAD models. Figure 5-2 illustrates the design process.

```
┌──────────────────────────┐          ┌──────────────────────────┐
│   CRS surface geometry    │          │  Infant dummy geometry    │
│      (Figure 5-3)         │          │      (Figure 5-4)         │
└──────────────────────────┘          └──────────────────────────┘
              ↘                              ↙
                    ┌──────────────────┐
                    │    Foam block     │
                    └──────────────────┘
                              ↓
                    ┌──────────────────┐
                    │   PPD geometry    │
                    │    (Figure 5-5)   │
                    └──────────────────┘
```
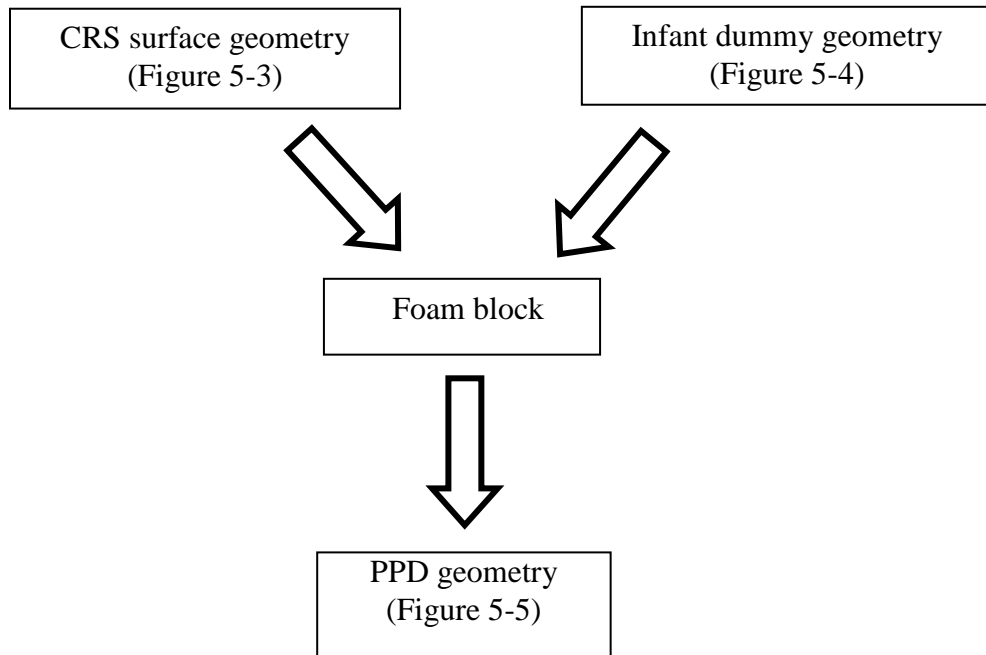
Figure 5-2. PPD geometry design flow chart.

With the surrounding (i.e. CRS and dummy) geometry input, the PPD shape was obtained. The back surface of the CRS was extracted. Both the CRS and the PPD CAD models were created in Catia V5R20. Figure 5-3 illustrates the CRS back surface CAD model.

32
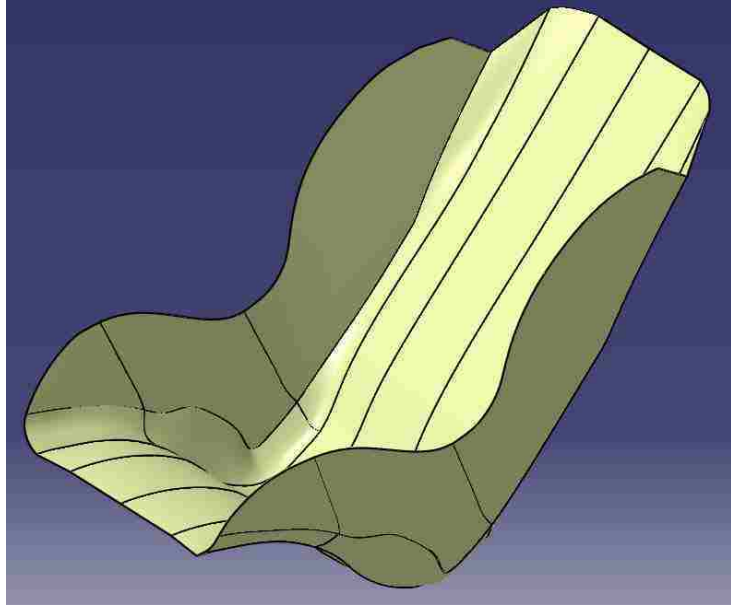
Figure 5-3. CRS surface CAD model.
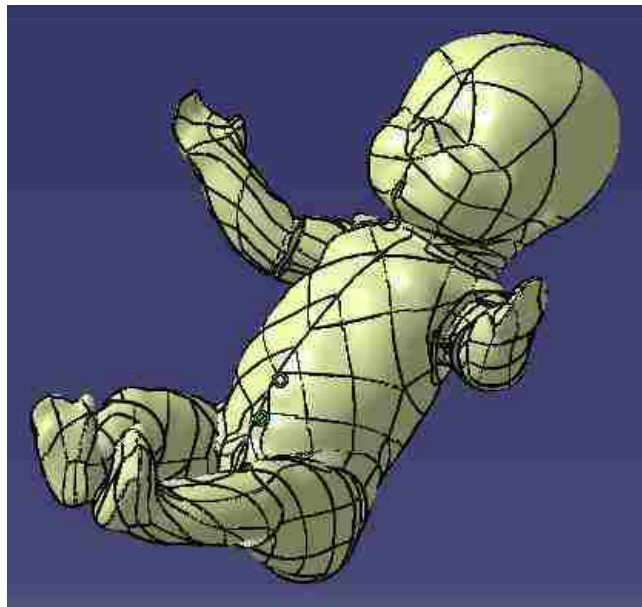
Figure 5-4. Infant dummy CAD model.

For the sake of proper supports to infants in an oversized CRS, the PPD was carefully designed based on infant geometry. The infant CAD model, as shown in Figure 5-4, was created using light scan. Details of the infant model development are presented in subsequent section. The shape of the foam insert allows infants to maintain a neutral position instead of head flexion posture while sitting in the CRS. Figure 5-5 illustrates the foam insert with/without infant dummy. Parametric studies were conducted to

optimize the foam insert design to provide respiratory stability without compromising crash protection performance expected from original CRS.
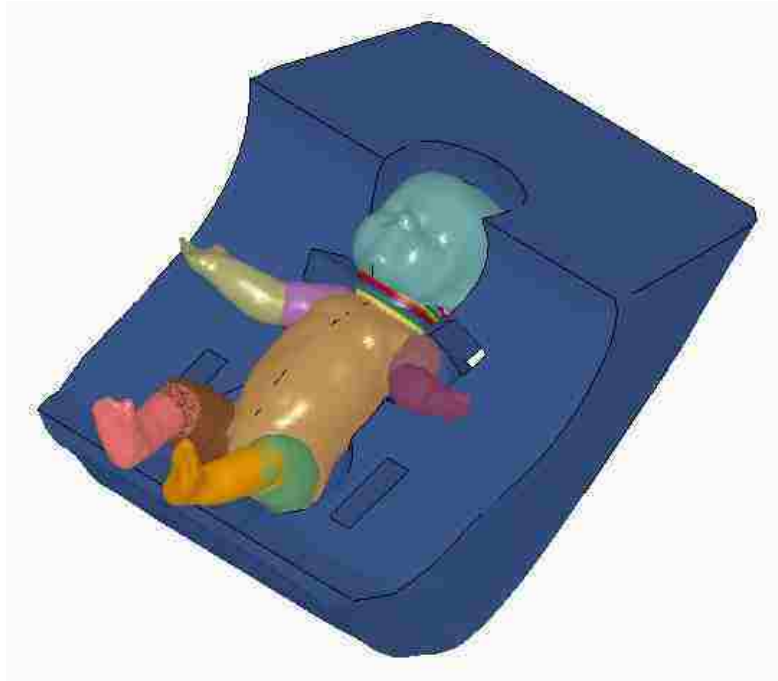
(a)
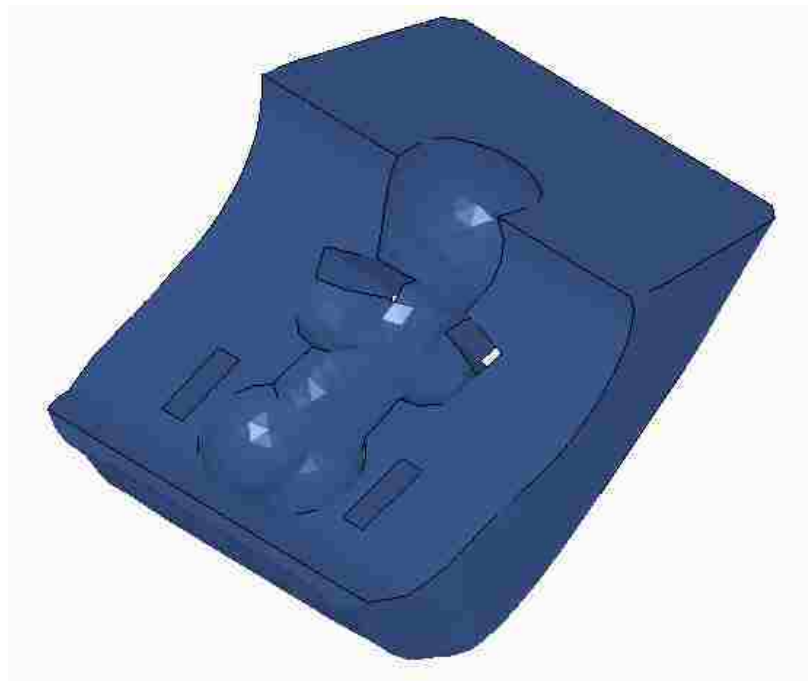
(b)

Figure 5-5. PPD (a) with infant; (b) without infant.

The CAD model was discretized using HyperMesh version 8.0. Due to the complexity and irregularity of the insert geometry and the requirement of design iterations, tetrahedron elements were implemented during the meshing phase instead of hexahedron elements. A surface mesh was first created using automesh. Table 5-1 tabulates the element quality index utilized to check the element quality. The enclosed surface discretization was utilized to create three-dimension tetrahedron elements. The foam insert mesh was illustrated in Figure 5-6.

Element quality index	Value
warpage	> 5
aspect ratio	> 5
length	< 5
jacobian	< 0.7

Table 5-1. Element quality index

Figure 5-6. PPD discretization.

5.3 Foam material

One of the most crucial aspects of this project was the selection of the proper foam material for the insert device. A series of experiments on different foams were conducted previously by Altenhof's research group at University of Windsor. In a preliminary study earlier, the foam material, referred to as A9_002, was used to assist the development of FE model. With the assistance from the foam manufacturer, the Woodbridge Foam Corporation, nine foam material candidates were provided along with their material properties and test processes. A total of ten candidates were under investigation, including Foam A9_002. Two kinds of foam material were provided by Woodbridge Foam Corporation: high resilience foam and viscoelastic foam. The viscoelastic foam is defined in ASTM3574 [31] as a specially formulated urethane foam characterized in slow recovery, low resilience, and high hysteresis loss. For the sake of simplicity, the foam candidates were assigned with individual foam number and were referred to as the number assigned in the rest of the thesis, as shown in Table 5-2.

Foam name as received	Foam name assigned
A9_002	Foam#1
A2@500 mm/min	Foam#2
#12@500 mm/min	Foam#3
#8	Foam#4
#11	Foam#5
#12	Foam#6
A12	Foam#7
B2	Foam#8
D2	Foam#9
D2@500 mm/min	Foam#10

Table 5-2. Foam candidates list.

5.3.1 Foam tests procedures

The foam tests were conducted at Woodbridge Foam Corporation based on ASTM3574 protocol [31]. The density of the foam was determined by calculation from the mass and volume of the specimen. The test specimen on the supporting plate of the apparatus was compressed at a rate of 50 ± 5mm/min.

Tests results were reported as force versus displacement, shown in Figure 5-7, which were converted into stress-strain curves in order to implement into FE model. For the sake of reasonable simulation run time, only three foam materials were selected to perform the foam material parametric study. These three materials were: Foam#1, Foam#2, and Foam#3. There were two major reasons for the selection of Foam#2, and Foam#3: (1) they are typical representation of high and low stiffness for the available samples; (2) they have the viscous characteristics, which will stiffen the material when experiencing elevated strain rates, typically present in crash events. All of the three foam materials were investigated in all scenarios: crash events and normal driving conditions. The stress-strain curves of these three foam materials are illustrated in Figure 5-8.
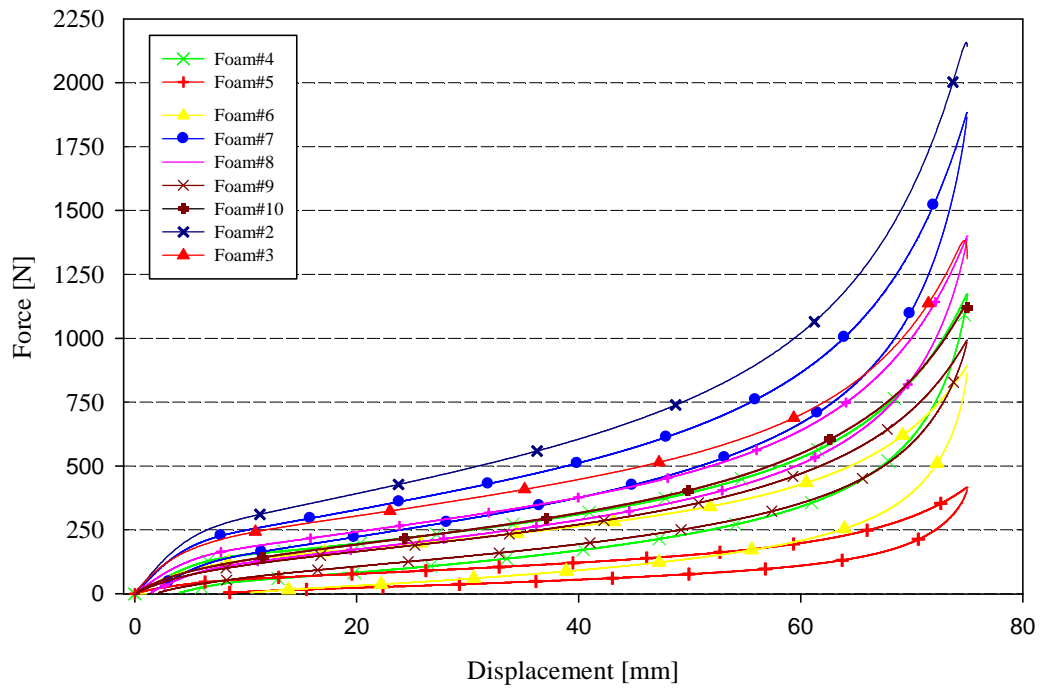
Figure 5-7. Experimental results of the foam materials - force versus displacement curves.
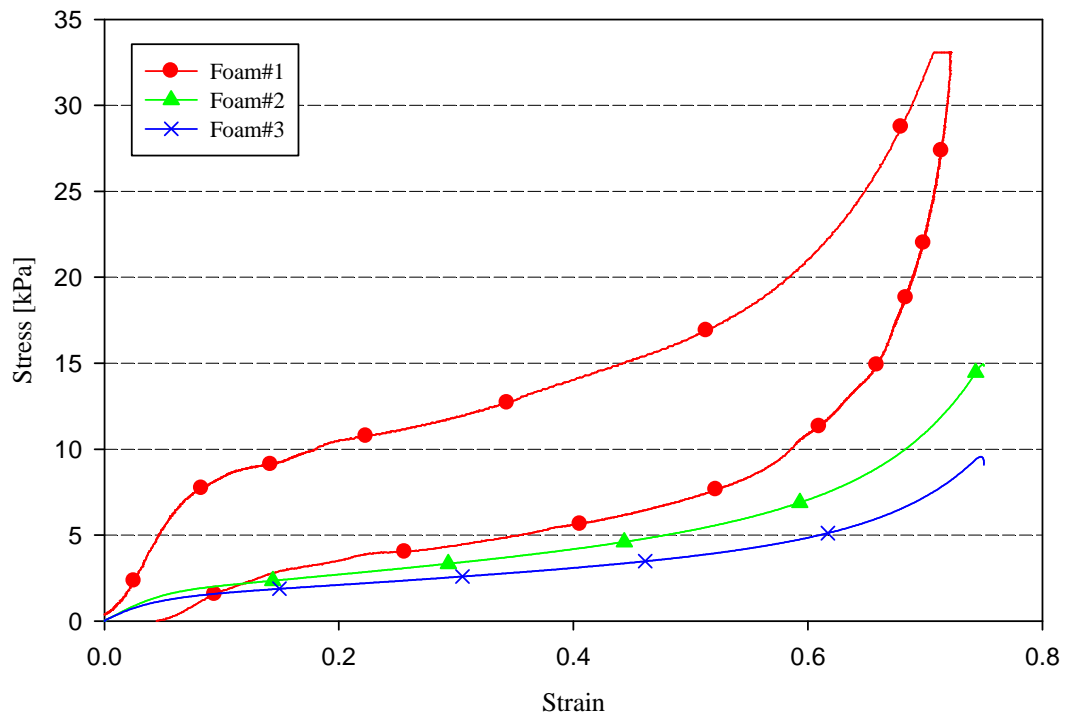
Figure 5-8. Stress versus strain response of the foam materials.

5.3.2 Foam material numerical model development

The foam was modeled using material model which is applicable for modeling highly compressible low-density foams. The material model is referred to as MAT_057 or MAT_LOW_DENSITY_FOAM in LS-Dyna keyword user's manual [36]. The material density, load curve, hysteretic unloading factor, and shape factor were inputted to define the behavior of the foam material.

Mathcad script created by Altenhof was utilized during this process. This Mathcad script is presented in Appendix A. The script is capable of importing experimental data (force-displacement data), calculating, and plotting stress/strain curves. Approximately 15 points were selected for each material, and curves were created using cubic spline interpolation function, which is referred to as cspline in Mathcad, to fit those points to mimic the nonlinearity behaviours of experiment results. Cubic spline interpolation passes a curve through a set of points in such a way that the first and second derivatives of the curve are continuous across each point. The fitted curves were exported and implemented into the numerical foam material models.

The obtained loading curves were implemented into crush block model, as shown in Figure 5-9, to assist investigating hysteretic unloading factor (HU) and shape factor for unloading (SHAPE), which define unloading characteristics of the foam material. The crush block model was utilized to perform a numerical experiment to validate the foam material model. The geometry of the foam block was adjusted according to the physical test specimen. The base (not shown in the figure) and indentor were modeled as rigid wall. The indentor/foam contact and the base/foam contact were modeled using surface-to-surface contact definition with a static friction coefficient of 0.20 and a dynamic friction coefficient of 0.17. The diplacement was imposed on rigid indentor to result in an approximately 75% deflection of the foam block. The numerical results, the force and displacement from the crush black model simulations were obtained for the sake of model validation. The hysteretic unloading factor (HU) and shape factor (SHAPE) were

calibrated based on the validation results. Figure 5-10 illustrates the stress-strain curves with different unloading parameter setups.
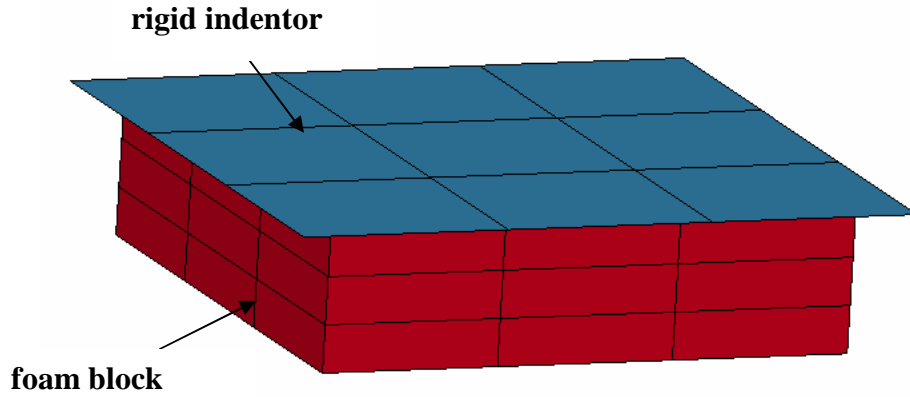
Figure 5-9. Crush foam block finite element model.
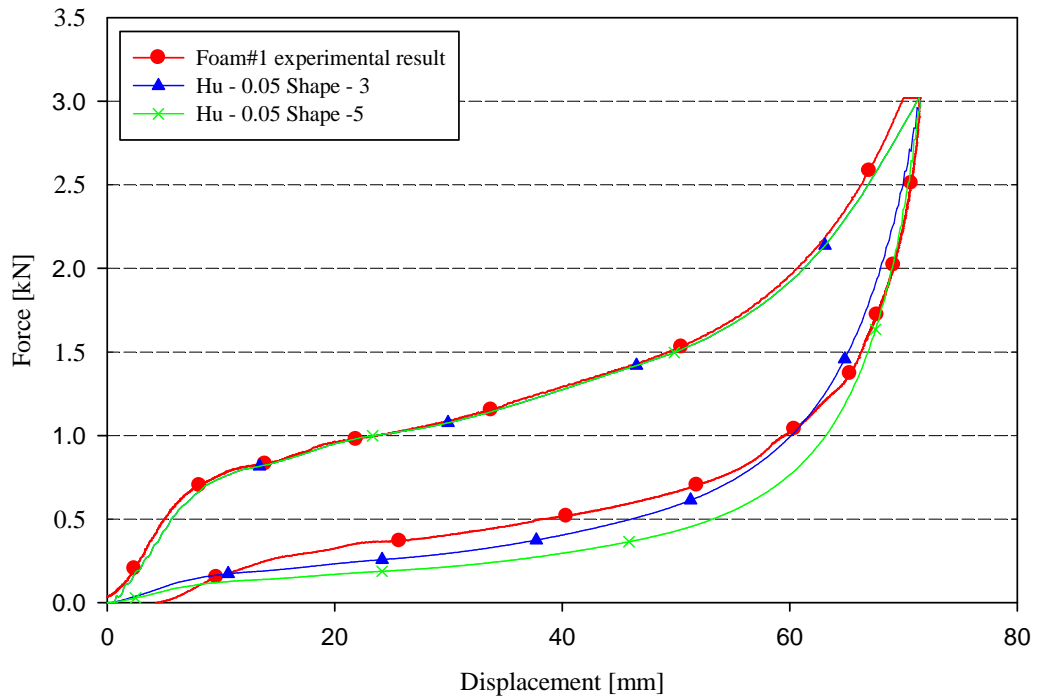
Figure 5-10. Loading and unloading curves corresponding to different HU and SHAPE values.

The loading-unloading curves for foam material Foam#1, Foam#2, Foam#3, Foam#6, and Foam#7 are shown in Figure 5-11, Figure 5-12, and Figure 5-13, respectively. These figures also present the corresponding experimental findings. For Foam#2 and Foam#3, only the loading curves were available. All numerical models were validated using Model Validation Metric [32]. Details of model validation metric are presented in Chapter 2. The results of the validation metric for the foam models are tabulated in table 4-1. The validation metric was calculated with regarding the time domain due to the requirement of ascending of the independent variable.
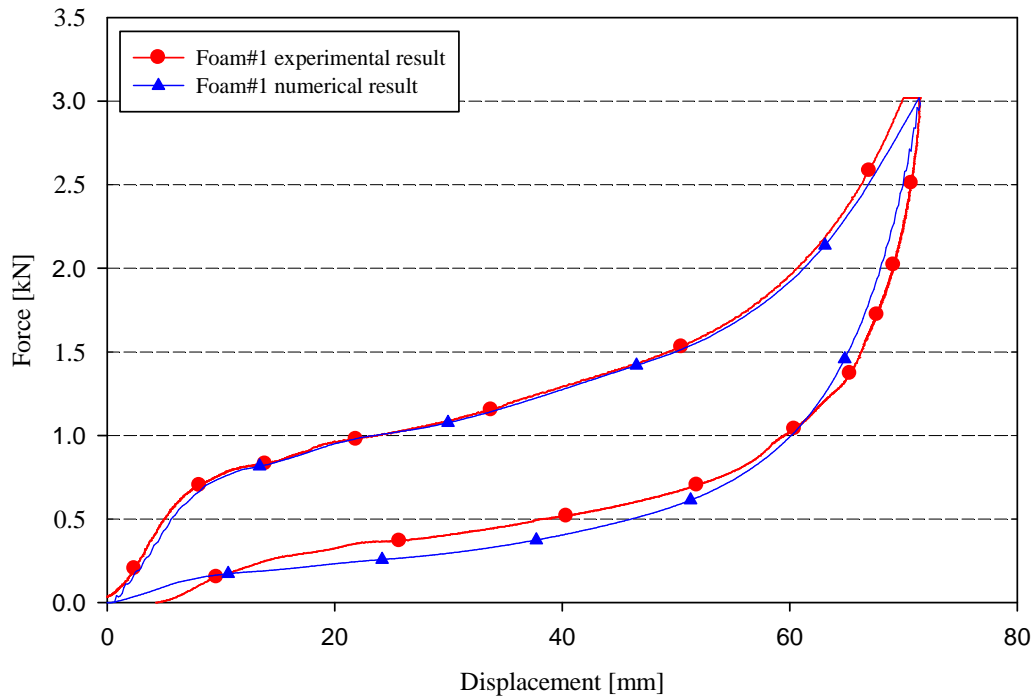
Figure 5-11. Force versus displacement response of Foam#1.
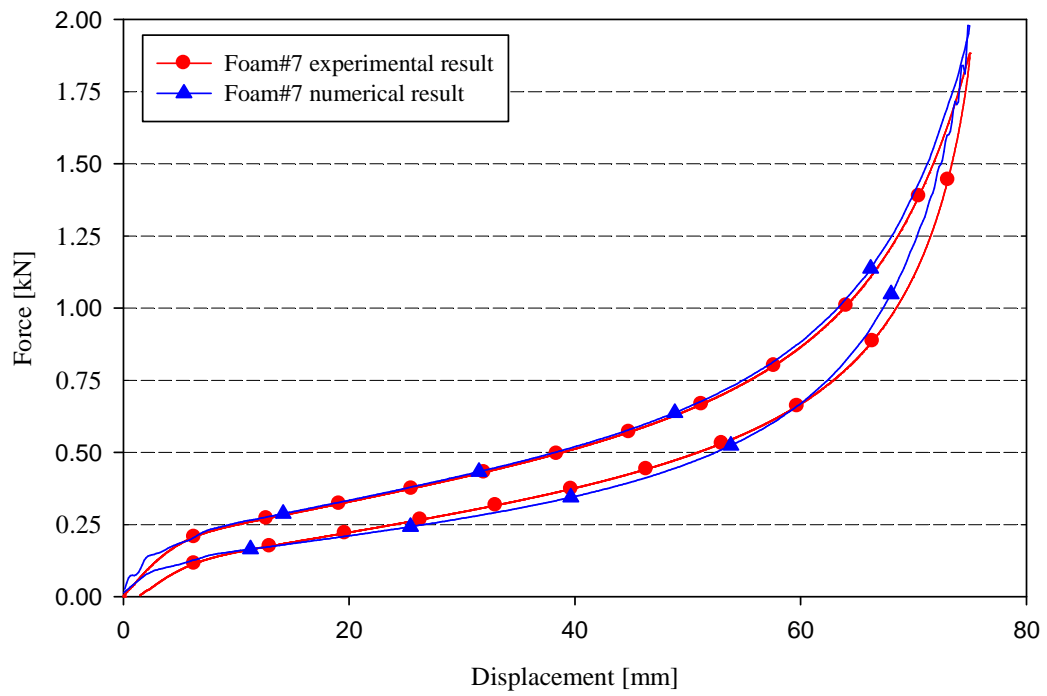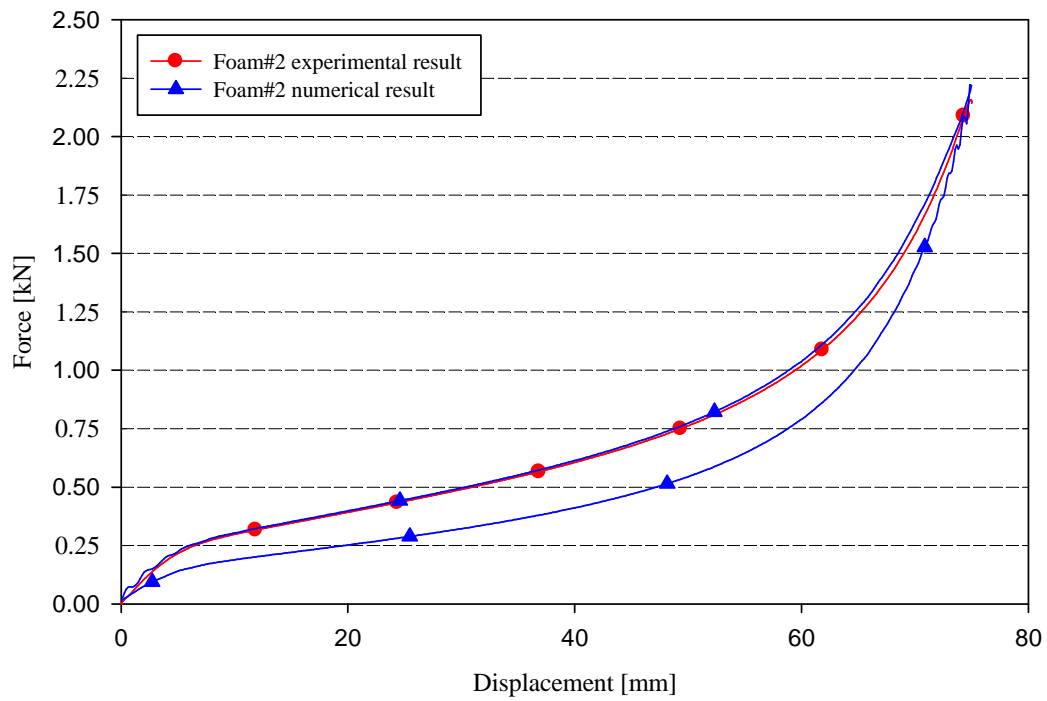
Figure 5-12. Force versus displacement response of : (a) Foam#7; (b) Foam#2.
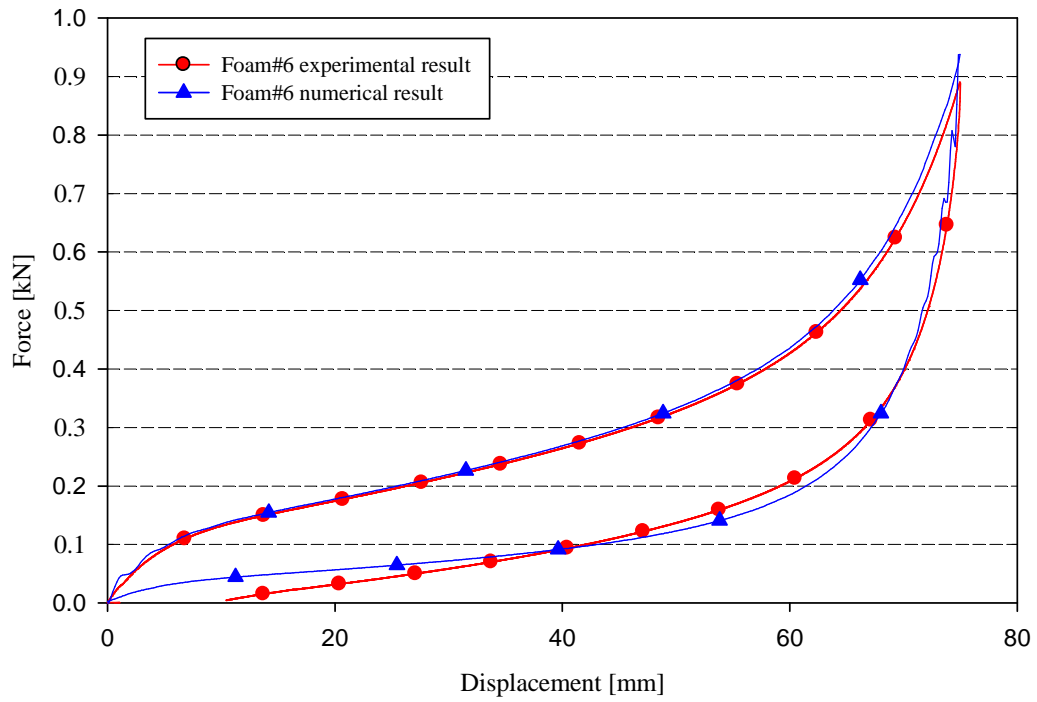
(a)
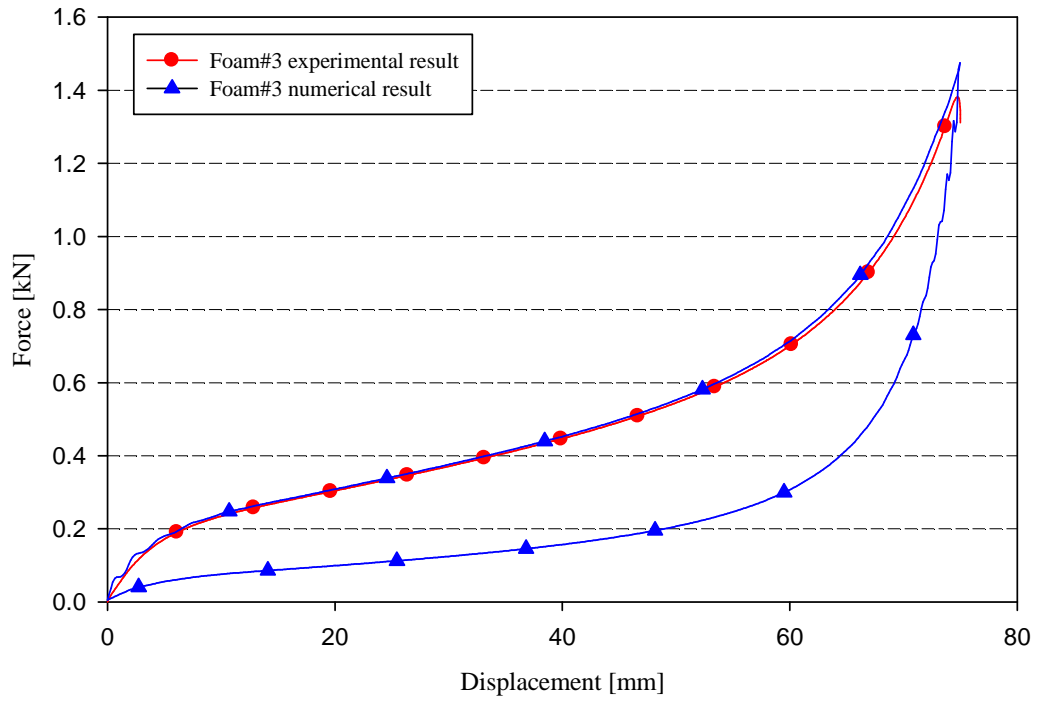
(b)

Figure 5-13. Force versus displacement response of : (a) Foam#6; (b) Foam#3.

Foam	Foam#1	Foam#7	Foam#2	Foam#6	Foam#3
Validation metrics	0.826	0.926	0.977	0.852	0.976

Table 5-3. Foam validation metrics summary.

5.4 CRS restraint system

The CRS five-point restraint system was modeled and routed to fit around the infant as in the actual CRS. The seatbelt was modeled as a combination of shell elements, one-dimension seatbelt elements, two-dimension seatbelt elements and slipring elements. Figure 5-14 illustrates the finite element model of the five-point restraint system.

2D seatbelt element (red)

shell element (yellow)

1D seatbelt element (pink)
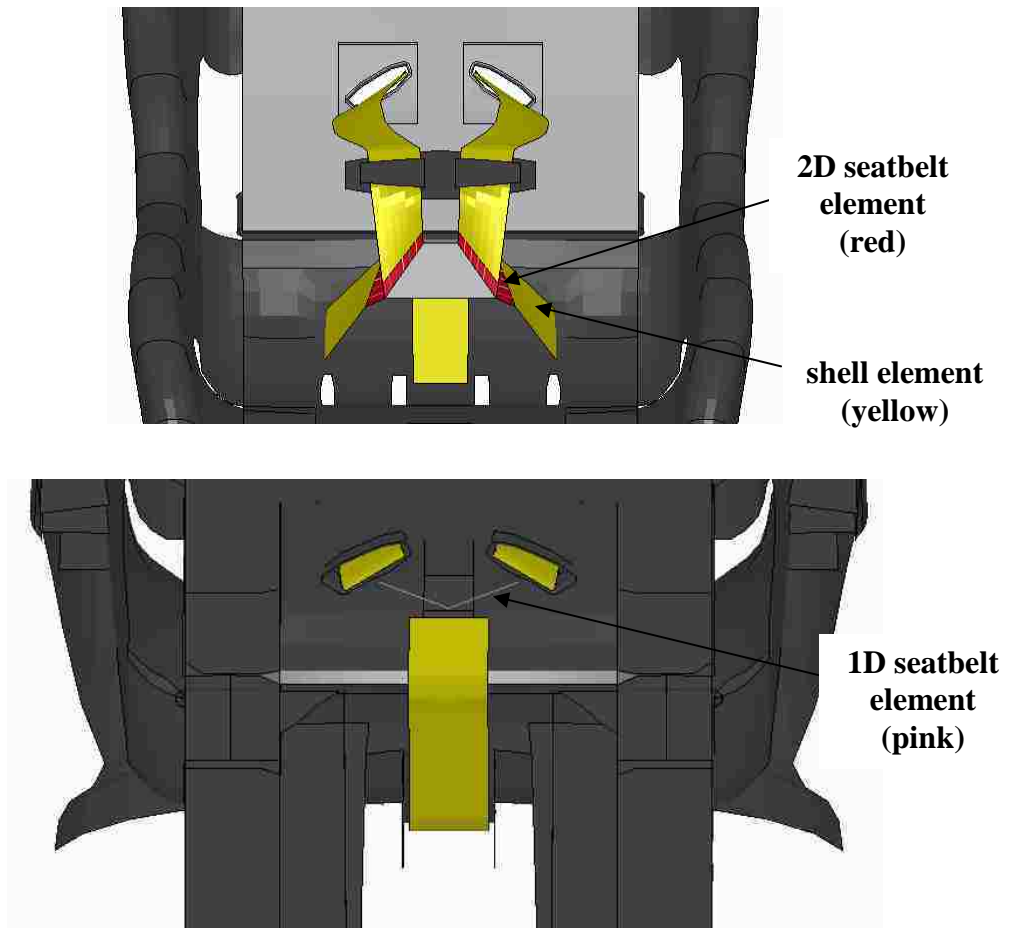
Figure 5-14. The CRS five-pint restraint system.

5.4.1 Modeling of CRS restraint system

The portion of the seatbelt, where contact is present between the infant and harness, was modeled as shell elements to provide good contact quality. The region where two webbings were merged at the back of CRS was modeled as one-dimensional beam elements for the sake of computational efficiency. One-dimensional beam elements were defined by *ELEMENT_SEATBEL. The connections between beam seatbelt element and shell element were achieved by using the keyword *CONSTRAINED_EXTRA_NODES_SET. The section where the seatbelt goes through the crotch clasp and experiences folding was modeled using two-dimensional seatbelt element. Two-dimensional seatbelt element provides better contact definition when comparing with simplified one-dimensional seatbelt element, while keeping the capability of sliding through slipring element. Two-dimensional seatbelt elements were defined by *ELEMENT_SEATBELT_SLIPRING. The drawback of two-dimensional elements is the computational instability and more simulation cost. The shape of the elements plays a crucial rule in determining the stability level of those elements. Two-dimensional seatbelt elements are expected to be rectangle as close as possible to maintain computational stability. In addition to two-dimensional seatbelt elements, the mechanism of belt slipping was achieved by defining series of slipring elements. Those elements were defined by *ELEMENT_SEATBELT_SLIPRING. Sliprings allow continuous sliding of a belt through a sharp change of angle [36]. The card requires the definition of a series of nodes sets, and element sets, which indicate the elements on each side of the slipring. With the combination of two-dimensional seatbelt elements and slipring elements, this finite element harness is able to provide good contact definition and capability of belt slipring, which in turn allows the load passing through entire belt. All of those features allow the finite model to mimic the mechanical characteristics of real CRS seatbelt webbing.

5.4.2 Modeling of seatbelt material

The seatbelt material used in the research by Kapoor [29] was implemented in this research project. The experimental loading/unloading behaviour was incorporated in one-dimensional seatbelt elements [29]. Figure 5-15 shows force versus engineering strain response of the CRS webbing. A fully integrated Belytschko-Tsay membrane element formulation was utilized for both shell elements and two-dimensional seatbelt elements. Isotropic material behaviour was assumed. The material model was defined in *MAT_FABRIC, that invokes a special membrane element formulation which is more suited to deformation experienced by fabrics under large deformation [36]. The density, elastic modulus, and Poisson's ratio was specified as 890.6 kg/m^3, 2.068 GPa and 0.3 respectively [29].
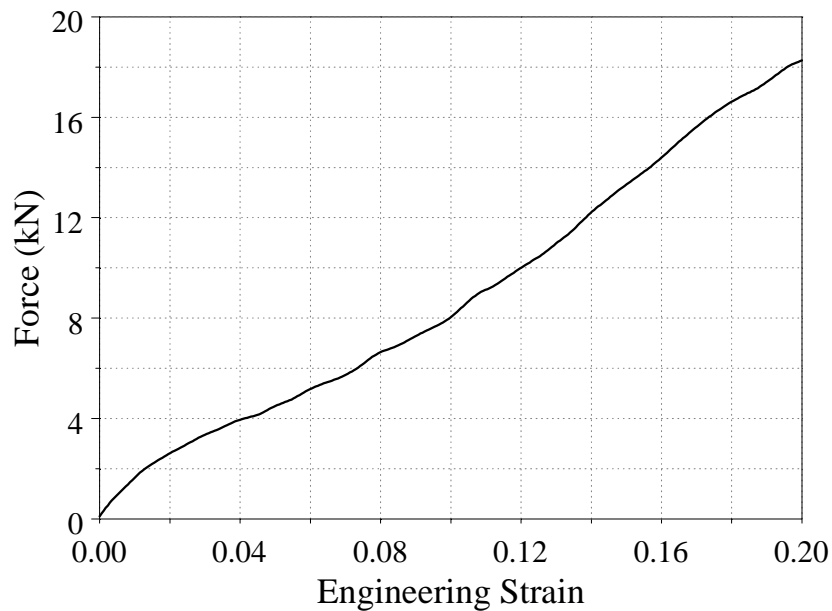
Figure 5-15. Force versus engineering strain response of the CRS webbing [29].

5.5 Low birth-weight infant ATD

One of the challenges of this research project was the availability of the proper ATD finite element model. Although there are a number of ATD which have been implemented in industry, to the best of the author's knowledge, there is no existing ATD finite element model for infants at such small age and weight (less than 5 lbf). One of the outcomes of this research project was the creation of low birth-weight finite element ATD model. This work was mostly done by another Master's candidate, Matthew J. Bondy. This section briefly describes the process of the creation of the ATD finite element model.

5.5.1 Modeling of low birth-weight infant ATD

The geometry of the low birth-weight infant finite element model was obtained by light scanning the Nita Newborn mannequin, which was provided Windsor Neonatal Intensive Care Unit (NICU). Figure 5-16 illustrates the mannequin for light scanning. The point cloud, as a result of the light scanning, was then transformed into pieces of surfaces. The finite element model was meshed based on those surfaces. Important geometry parameters, such as head circumference, chest circumference, etc., were compared with the measurements obtained from Windsor NICU. The finite element model was also compared with a newborn skeleton at the Ontario Science Center, which also assisted to justify the neck joint locations. Figure 5-17 shows the finite element model overlapping the photograph of skeleton.

Figure 5-16. Nita Newborn mannequin ready for light scanning.

Figure 5-17. The finite element model and the infant skeleton.

The body segments, except the neck, were all meshed as two-dimension rigid shell elements, with the mass and inertia properties assigned at certain. A thorough study was conducted by Matt to determine the inertia properties of these. The neck was modeled as seven neck segments, which were connected by series of spherical and translational joints. The biomechanical properties for the neck were based upon the research results from Luck et al. [37] and Ouyang et al. [33]. Other joints, such as the hip, shoulder, elbow, knee joints, have also certain degree of freedom. Figure 5-18 illustrates the low-birth weight infant finite element model in the CRS seating configuration.
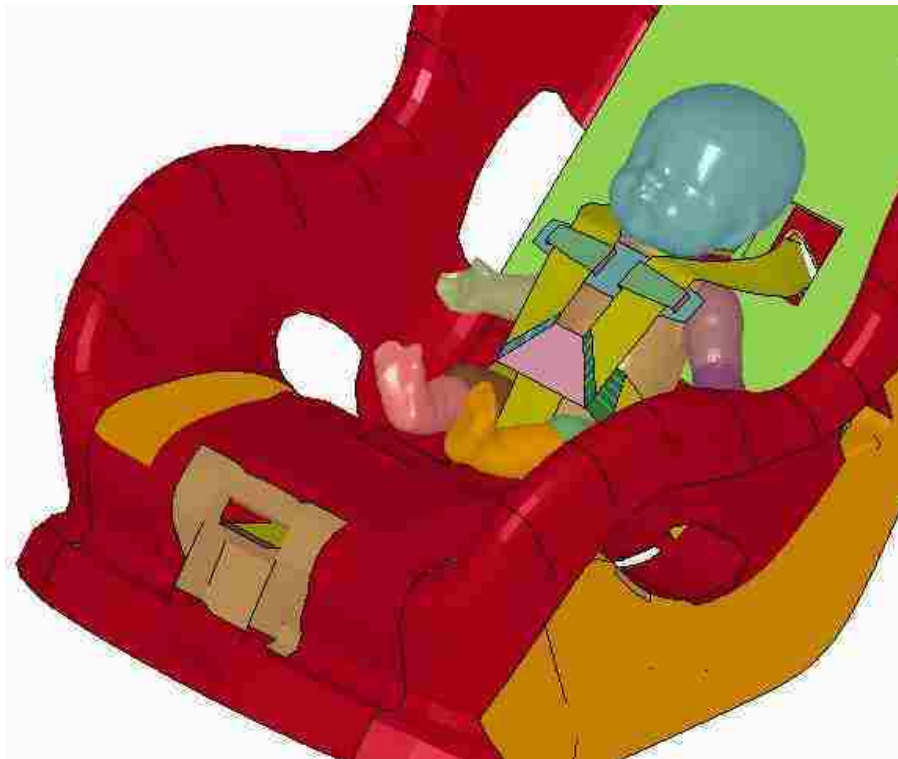
Figure 5-18. Low birth-weight finite element model in CRS.

5.6 Simulation Procedure

Simulations consisted of two stages namely, (i) tightening of the harness strap and (ii) application of acceleration (e.g. side crash acceleration pulse, etc.).

The first simulation stage was achieved through the process of dynamic relaxation. Dynamic relaxation allows LS-Dyna to approximate solutions to linear and nonlinear static or quasi-static processes [38]. Dynamic relaxation is used is used in the beginning of the solution phase to obtain the initial stress and displacement field prior to beginning the analysis [38]. The front-adjusting harness strap was tightened to position the low birth-weight infant model into the foam insert or CRS by defining *BOUNDARY_PRESCRIBED_MOTION. Figure 5-19 illustrates the prescribed curve. The load assigned to the tightening force was approximately 20 N. The number of iterations between convergence checks and the convergence tolerance was set to be 250 and 0.006 respectively. Figure 5-20 illustrates the current kinetic distortional energy and maximum kinetic energy versus time responses during the dynamics relaxation stage. Distoritional kinetic energy is total kinetic energy less the kinetic energy due to rigid body motion [36].
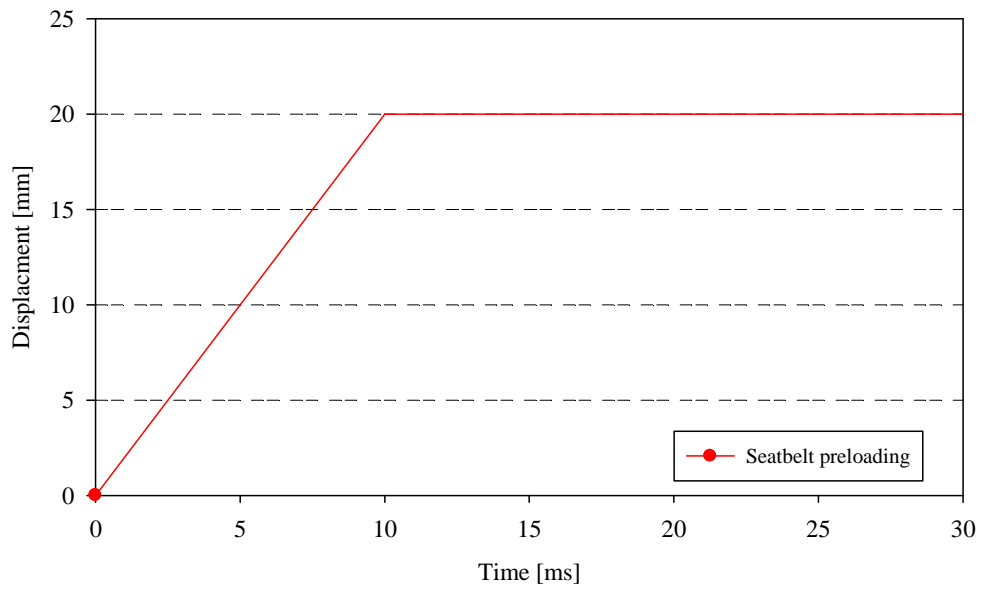
Figure 5-19. Seatbelt preloading input curve.
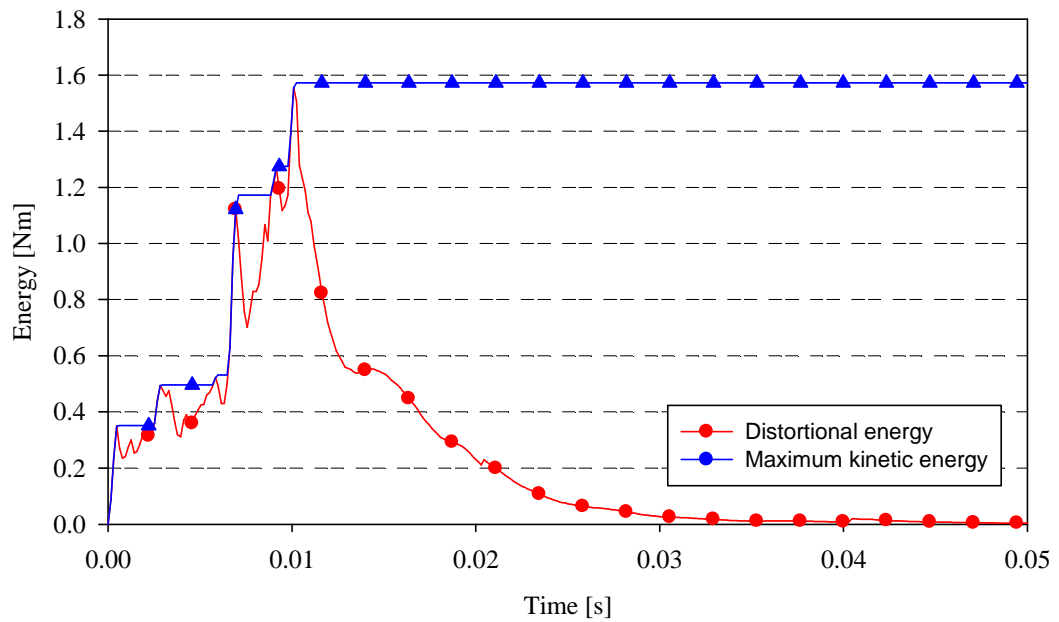
Figure 5-20. Distortional energy and maximum kinetic energy curves during dynamic relaxation phase.

The second stage was the application of acceleration. The acceleration time response was prescribed to the location on the CRS, where the accelerometer was mounted. Figure 5-21 shows the location where the acceleration was applied. The details of various events simulated are presented in the subsequent chapters.
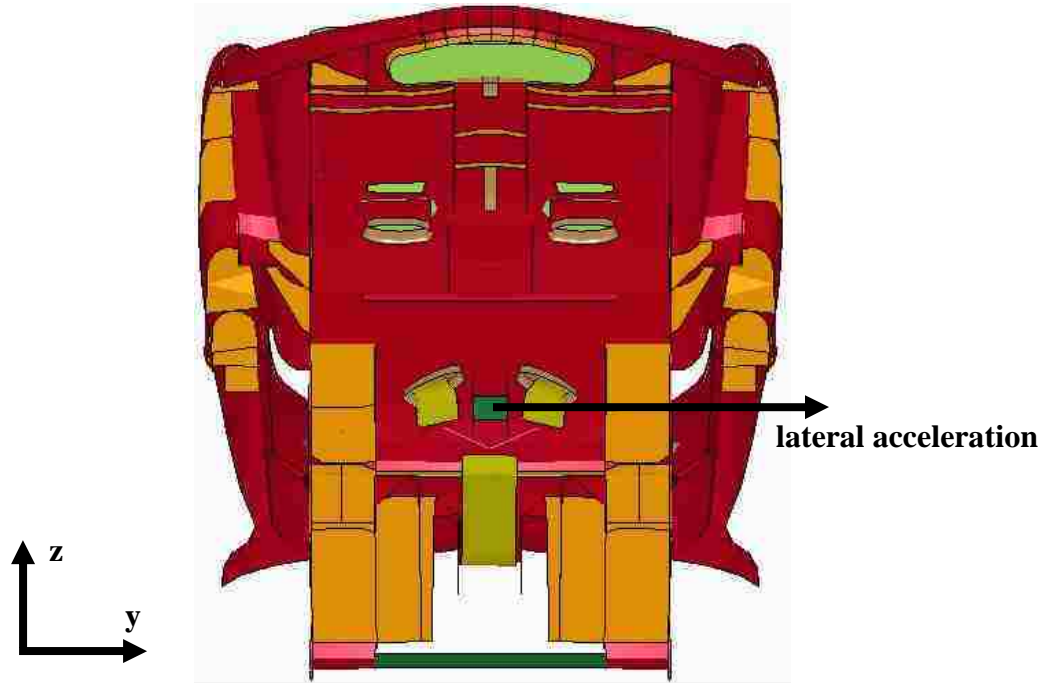
Figure 5-21. The application of acceleration pulse.

5.7 Data extraction

The performance of the foam insert device was judged based on the responses from the low birth-weight infant model under various events. One of the most important parameters was the neck angle of the infants, which has significant effect on the respiratory functionality of the child as mentioned in a number of documents from the literature review. Since there is no airway modeled in the finite element model, the neck angle becomes the indirect parameter to estimate the airway functionality. The neck angle was defined as the angle between the line from the outer canthus to the external auditory meatus and the longitudinal axis of the infant's trunk [26]. Figure 5-22 illustrates the definition of the neck angle. Point 1, 2, and 3 in Figure 5-23 defined the axis from the outer canthus to the external auditory meatus, and point 4, 5, and 6 in Figure 5-24 defined the longitudinal axis of the infant's trunk. The position of those nodes was monitored. The neck angle was calculated based upon these two defined axis. A mathcad script was created and utilized to estimate the neck angle. The script are present in Appendix C.
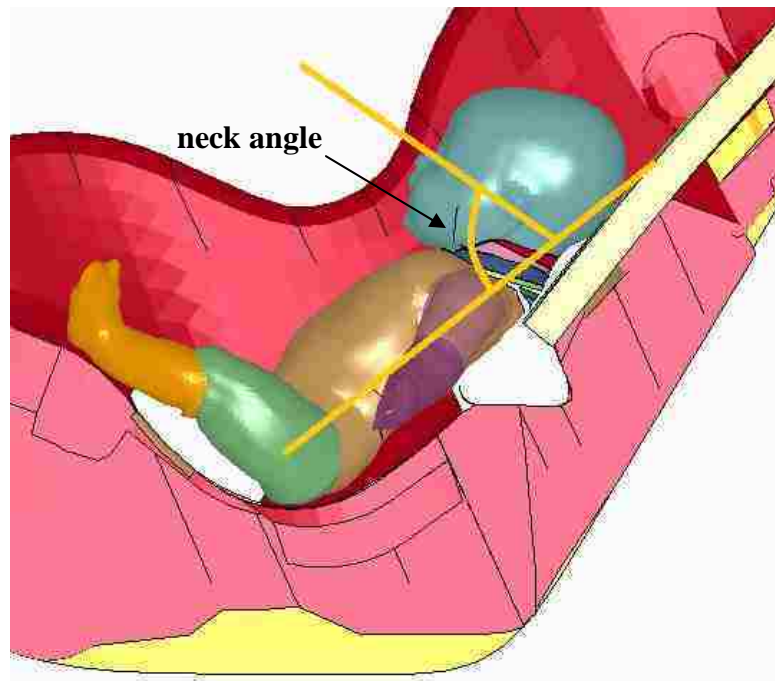
Figure 5-22. Infant's neck angle definition.
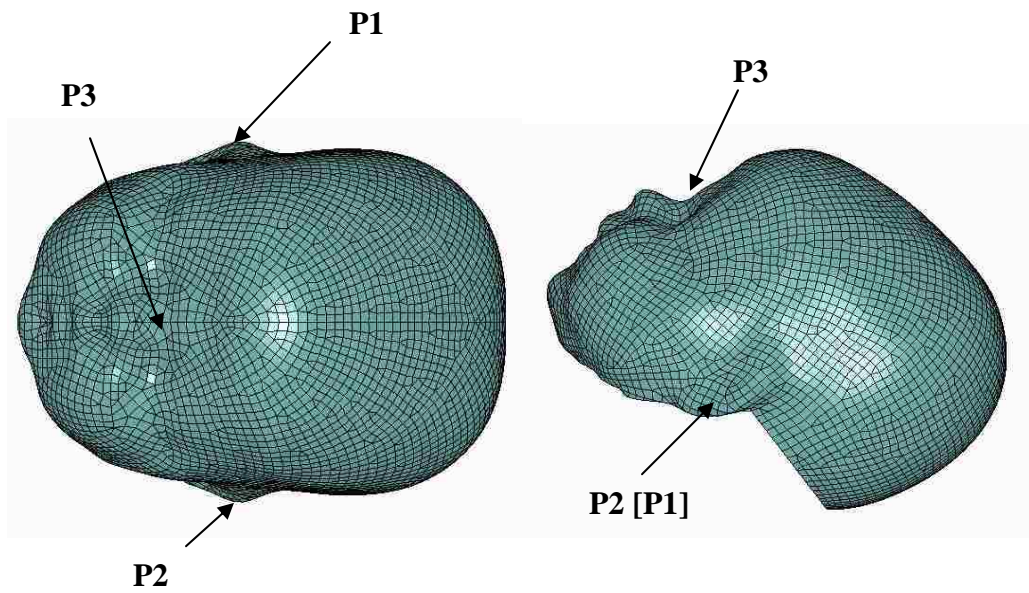
Figure 5-23. Points defining head axis locations.
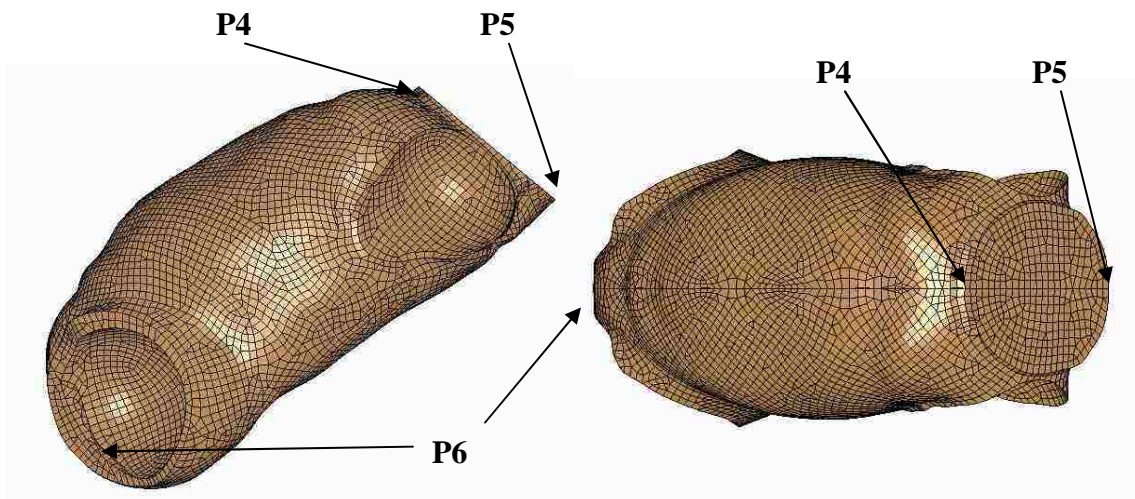
Figure 5-24. Points defining torso axis locations.

54

The "rbdout" ASCII was requested to measure the kinematics parameters at the mass centre of the infant's head, including acceleration, velocity, and displacement. The Head Injury Criteria (HIC) was calculated to assist the child occupant injury level for the crash events. The time window of the HIC was selected to be 36 ms. Although the primary goal of this project was not focused on the improvement of child crash protection, the HIC, as an integration parameter, provides quantitative evaluations of the performance of the insert foam design. The formulation of HIC calculation is present below

$$HIC_{t_2 - t_1} = \left[\frac{1}{t_2 - t_1} \int_{t_1}^{t_2} a_{resultant} \cdot dt \right]^{2.5} \cdot (t_2 - t_1) \quad [29]$$

where

$$a_{resultant} = \sqrt{a_x^2 + a_y^2 + a_z^2} \quad [29]$$

t_2 and t_1 are any two arbitrary times during the acceleration pulse. Acceleration is the resultant acceleration measured in multiples of the acceleration of gravity (g) and time is measured in seconds. The *HIC* measures the effects of head acceleration and duration [29].

The neck forces were monitored during various numerical simulations. The locations of the upper, middle, and lower neck are illustrated Figure 5-25 illustrates.
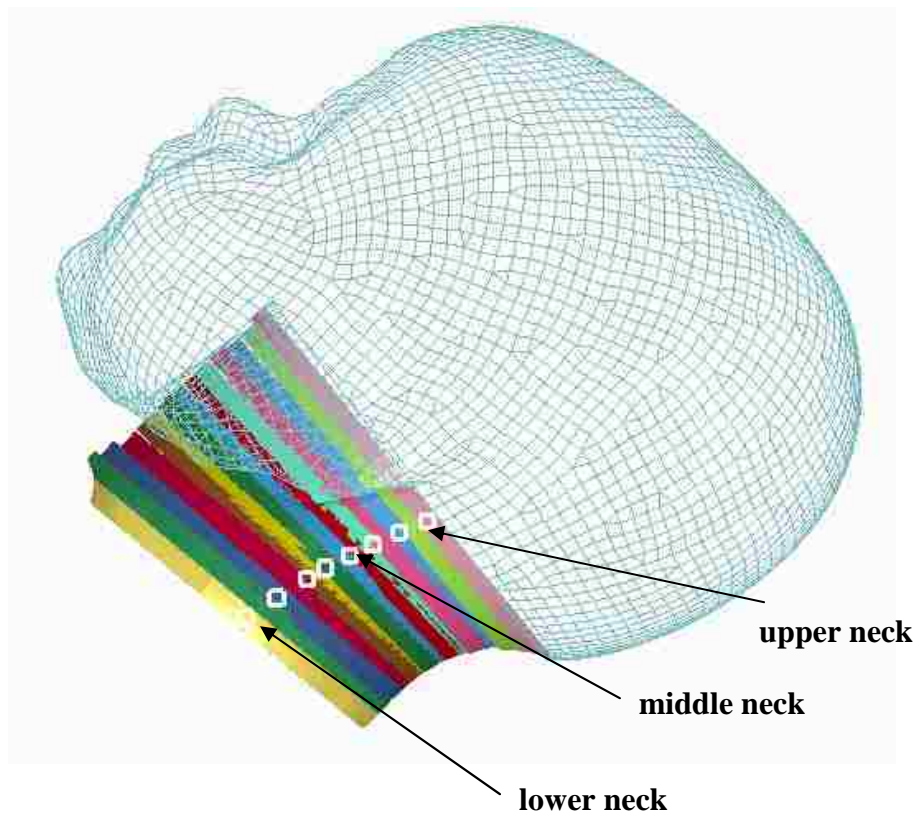
Figure 5-25. Upper neck, middle neck, and lower neck locations.

In the case of crash event simulations, all results were sampled at a rate of 10 kHz. The results were filtered in accordance to SAE J211. The crash event simulations were run for 150 milliseconds. During the normal driving condition simulations, the results were sampled at a rate of 1 kHz. The normal driving condition simulations were run for approximately 3 seconds.

5.8 Preliminary results

A preliminary simulation was run to decide which design parameters should be focused on. For normal driving condition simulations, neck angle was interested and investigated due to low accelerations (less than 1 g). Figure 5-26 illustrates the head acceleration for Foam#2 under braking event as a function of time. As expected, the head acceleration was not significant and will not be reported in the later study unless there was unexpected behaviour observed in numerical results. Figure 5-27 illustrates the upper, middle, and lower neck joint forces for Foam#2 under braking event as a function of time. The neck joint forces at three locations presented insignificant amount of neck forces. Ouyang's [33] indicated that the minimum force at failure was 494 N which is much higher than the maximum neck joint forces predicted by normal driving condition simulations. Therefore, only neck angle was measured for normal driving condition study unless abnormal phenomenon was observed from the numerical results.
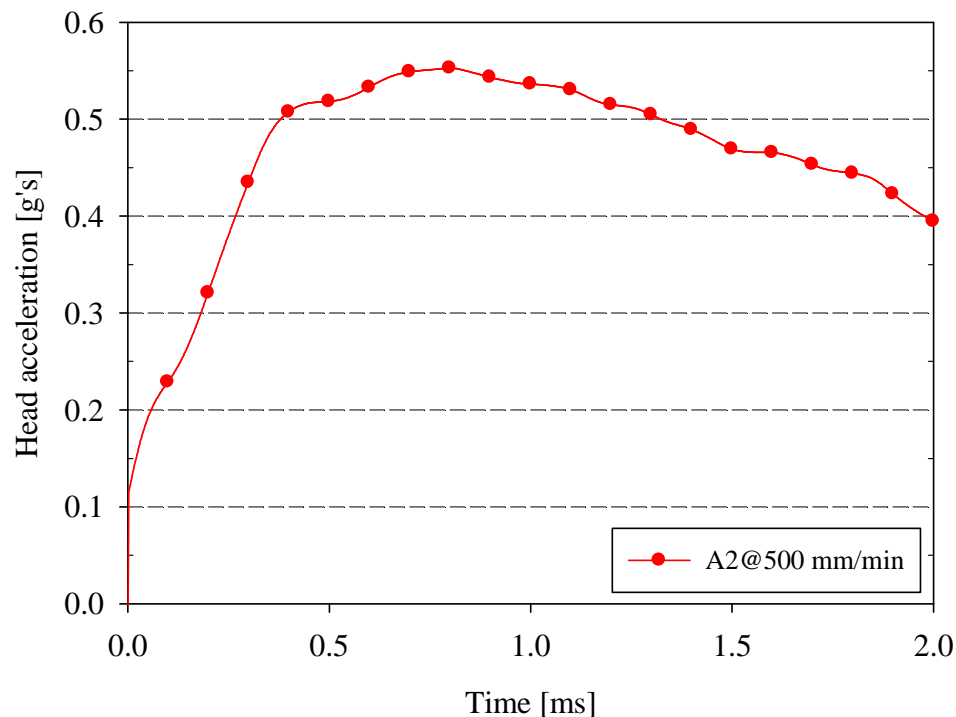
Figure 5-26. The head acceleration for Foam#2 under braking event.
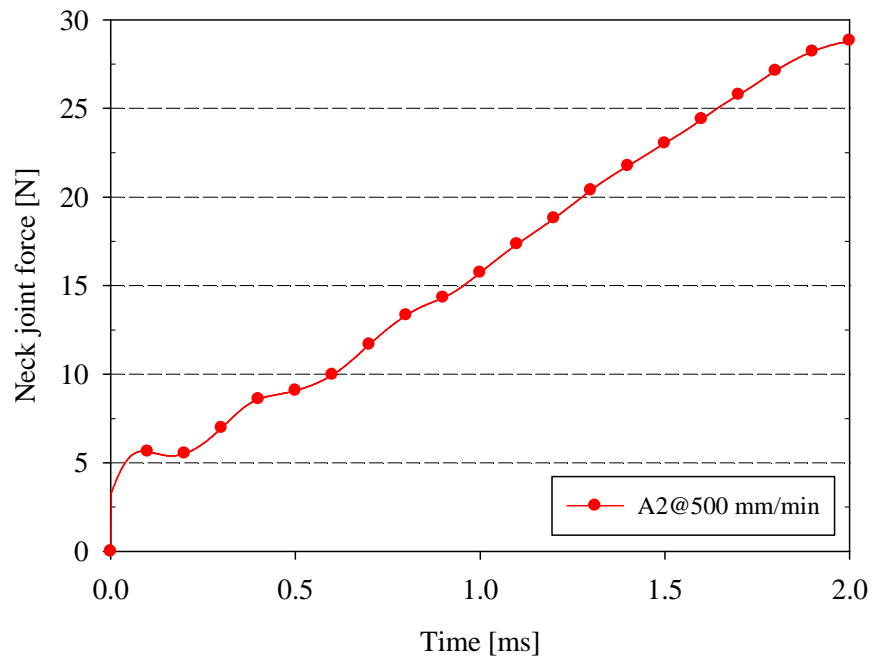
(a)
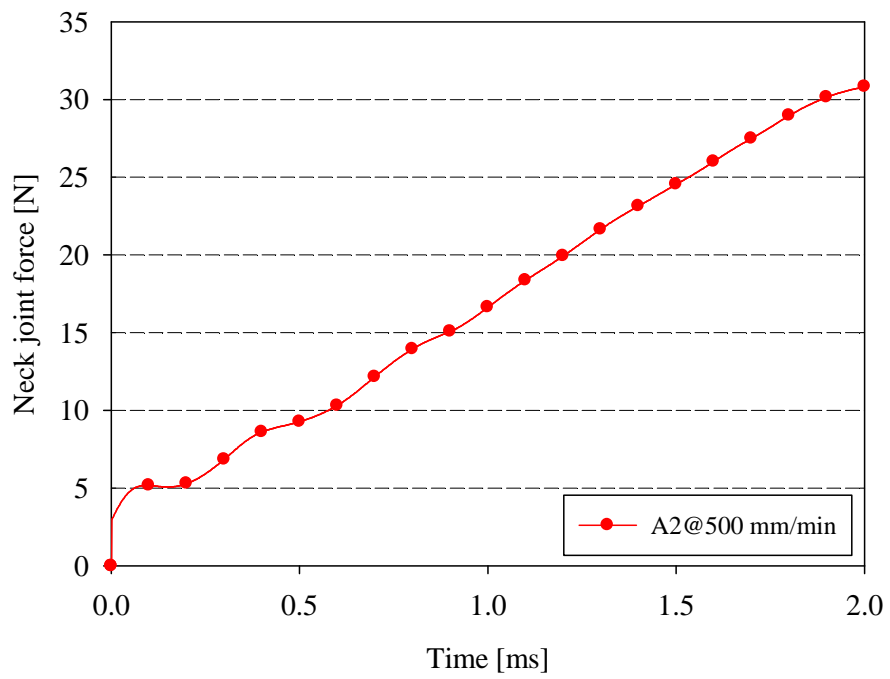
(b)
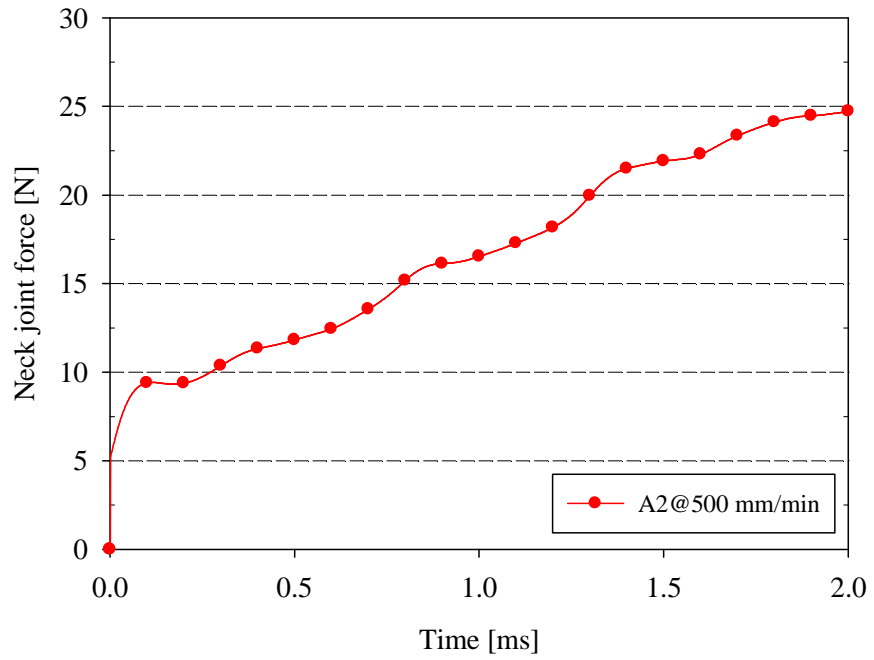
(c)

Figure 5-27. The neck joint forces for Foam#2 under braking event:
(a) upper neck joint, (b) middle neck joint, and (c) lower neck joint.

6 PPD MATERIAL PARAMETRIC STUDY - SIDE CRASH

A material parametric study was required to investigate the influence of different foam material on the performance of the PPD. The selection of the foam material was based upon the results of this material parametric study. This chapter describes the procedure and numerical results of this material parametric study under side crash. Chapter 7 and Chapter 8 describe the studies of frontal crash and normal driving condition, respectively.

The simulations were completed by utilizing the finite element analysis code LS-DYNA version 971 revision 50638 single precision (I4R4) on a personal computer with an Intel(R) Core™2 Duo CPU T9600 with an internal clock speed of 2.8 GHz, with the system having 3.00 Gigabytes of random access memory (RAM), using a 64-bit Windows 7 operating system. Typically this type of simulation took approximately 6 hours to complete.

6.1 Simulation procedure

A side crash event was simulated, to investigate the performance of the PPD under a side crash acceleration pulse. The side crash acceleration pulse, as shown in Figure 6-1, was obtained from the results of Kapoor's study [29], which forces on methods to mitigate injuries to toddlers in a vehicle crash. This method and the use of data ignored the effect of different methods that were applied to restrain the CRS to vehicles, for example, flexible latch, Lower Anchorage and Tether (LATCH), and rigid ISOFIX. The acceleration pulse illustrated in Figure 6-1 was a result from flexible latch restrain and rear-facing configuration. The acceleration was obtained at the location, as shown in Figure 5-21.
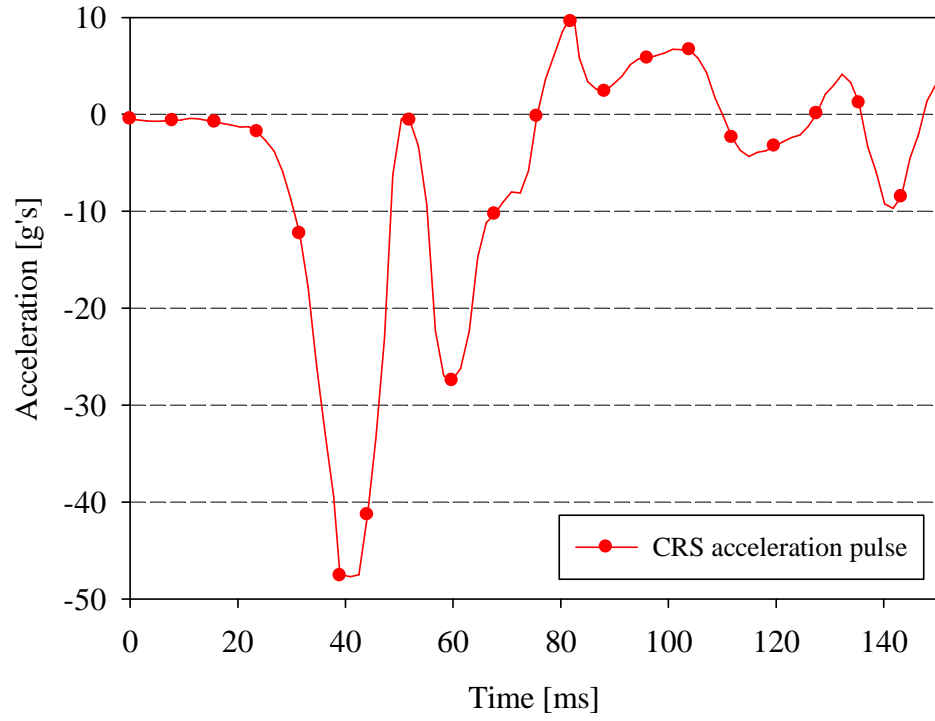
Figure 6-1. The side crash acceleration pulse applied to CRS.

6.2 Qualitative analysis

Figure 6-2 illustrates the numerical observations of a child dummy at specific instants of time through the side crash simulations when restrained in CRS with PPD made from three material candidates: (a) Foam#1, (b) Foam#2, and (c) Foam#3.

It should be noted that these observations were obtained from a transient phase of analysis, which means these simulations started after preloading of the CRS harness applied and settlement of the infant dummy. The CRS harness preloading was achieved by application of dynamic relaxation. Dynamic relaxation was described in detail in Chapter 4. The simulations observation at five different moments of time is illustrated in Figure 6-2. At t = 0, dummies were seated in their initial positions. The dummies' head started contacting with PPD at t = 50 ms. Based upon the numerical observation as shown in Figure 6-2 at t = 80 ms, the dummies were predicted to rebound back. A notable amount of deformation in the PPD was observed. Foam#3 had the largest deformation due to the least material stiffness. Part of the Foam#3 PPD was wrapped around a small portion of the dummy's face. This phenomenon was acceptable considering the duration was small, less than 10 ms, and the PPD recovered back to its original shape. It was observed that there was a contact between the dummy's head and the PPD at t = 120 ms when Foam#1 was utilized. No contact was observed for other two foams at the time of 120 ms. The final positions of dummies were at t = 150 ms.
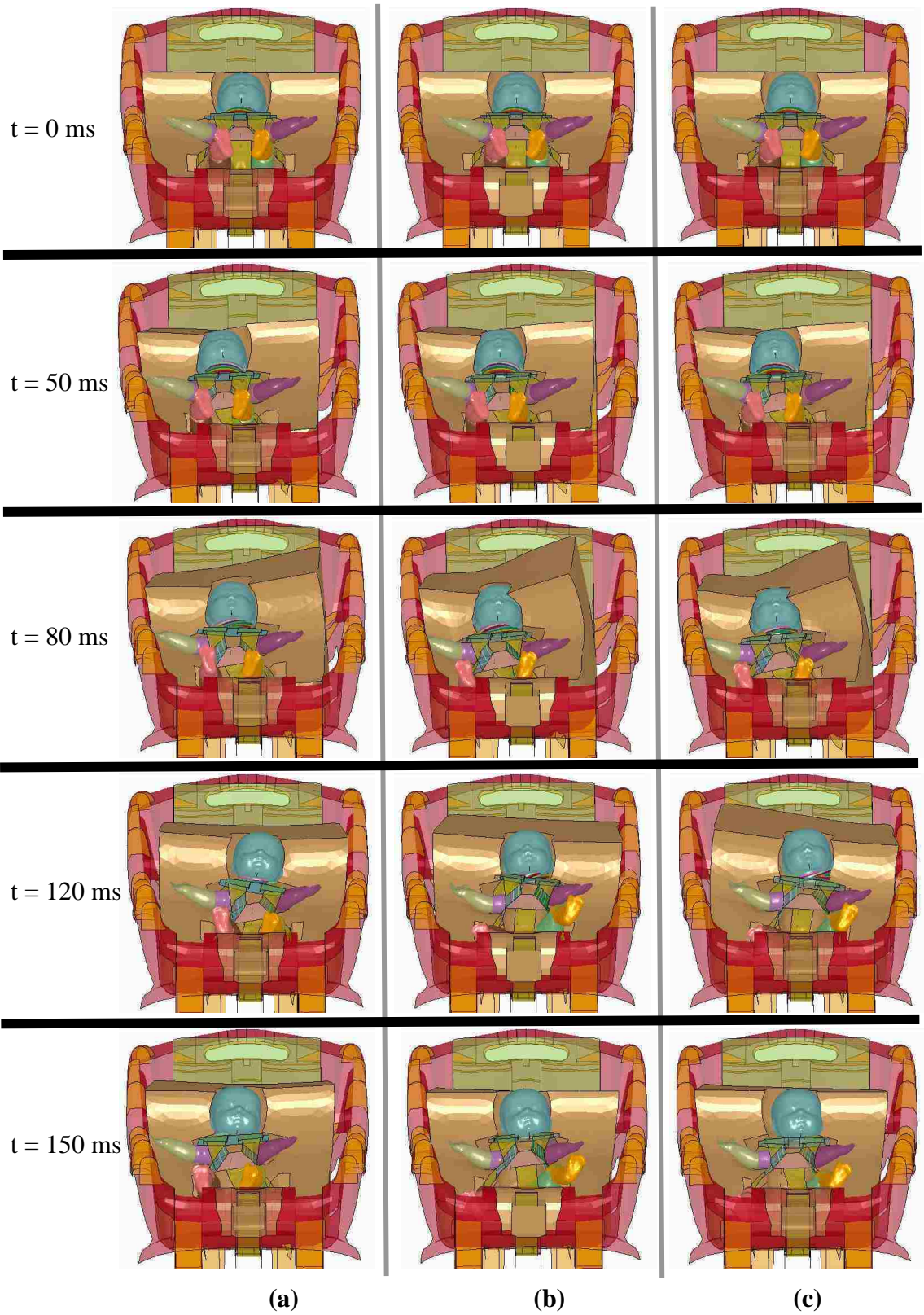
Figure 6-2. Numerical observation for CRS with PPD – side crash:
(a) Foam#1, (b) Foam#2, and (c) Foam#3.

6.3 Quantitative analysis

6.3.1 Neck angle

Figure 6-3 illustrates the neck angle profiles as a function of time for three foam material candidates under side crash event. The initial neck angle values were predicted to be 110 degrees over the first 40 ms for all three foams. At t = 58 ms, the maximum neck angles were predicted to occur. The maximum neck angles were predicted to be 118 degrees for Foam#1 and approximately 119 degrees for both Foam#2 and Foam#3. It should be noted that after those peak values, the dummy's head moved forward and consequently resulted in the reduction of the neck angles. Larger neck angles were predicted for Foam#2 and Foam#3. This can be attributed to the less stiffness of foam material. At t = 150 ms, Foam#3 was predicted to provide the largest neck angle of 95 degrees. Foam#1 resulted in the smallest neck angle of 91 degrees. For Foam#2, the neck angle was 93 degrees.
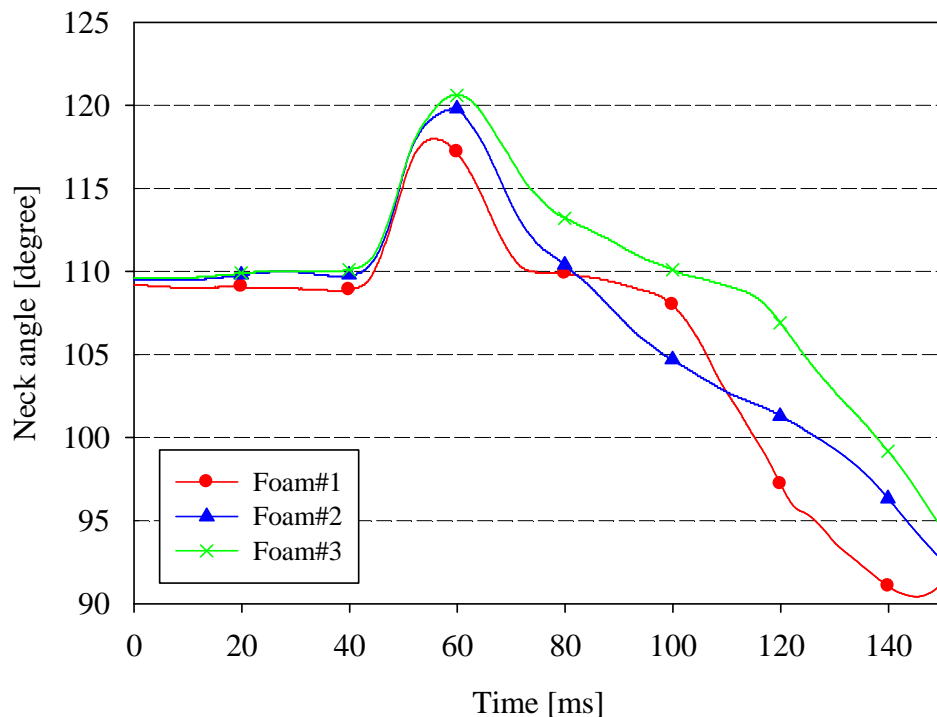
Figure 6-3. CRS with three foam candidates neck angles as a function of time – side crash.

6.3.2 Head acceleration

Figure 6-4 illustrates the head accelerations a function of time for the CRS with three material foams. Maximum values of the head acceleration were predicted to be 58g's, 58 g's, and 60 g's for Foam#1, Foam#2, and Foam#3, respectively. Similar head acceleration profiles were predicted for three foam candidates until t = 100 ms. Greater head acceleration was predicted for foam A9_002 from t = 100 ms to t = 130 ms. The contact between the head and the PPD was observed at t = 100 ms, which was responsible for the increase of the head acceleration. Figure 6-5 presents the HIC_{36} as a function of time for three foams. The maximum values of HIC_{36} were predicted to be 180, 204, and 182 for Foam#1, Foam#2, and Foam#3, respectively.
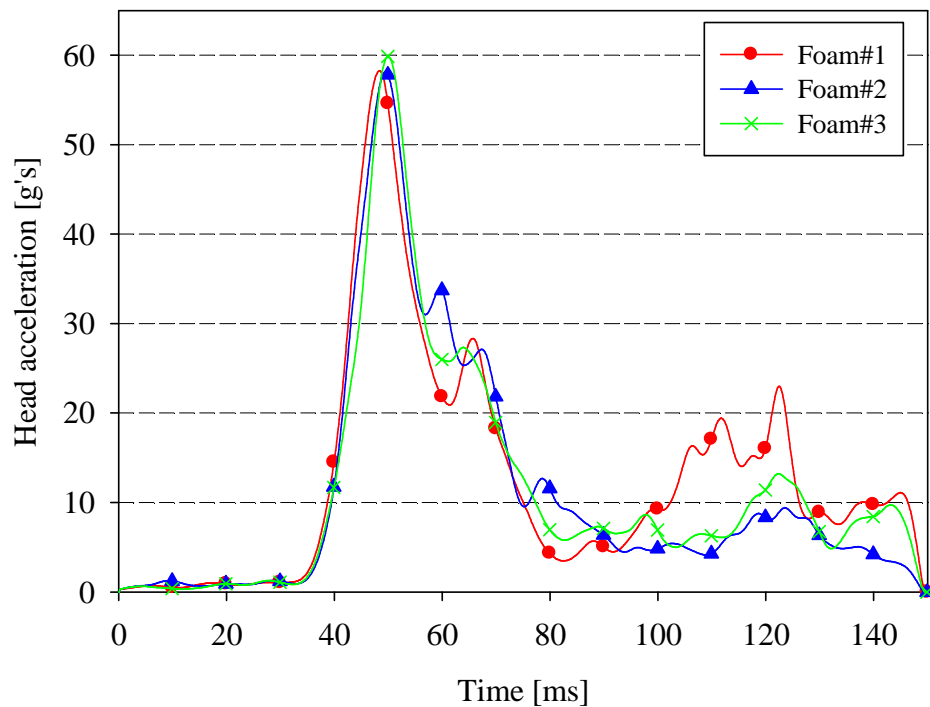
Figure 6-4. CRS with three foam candidates resultant head accelerations as a function of time – side crash.
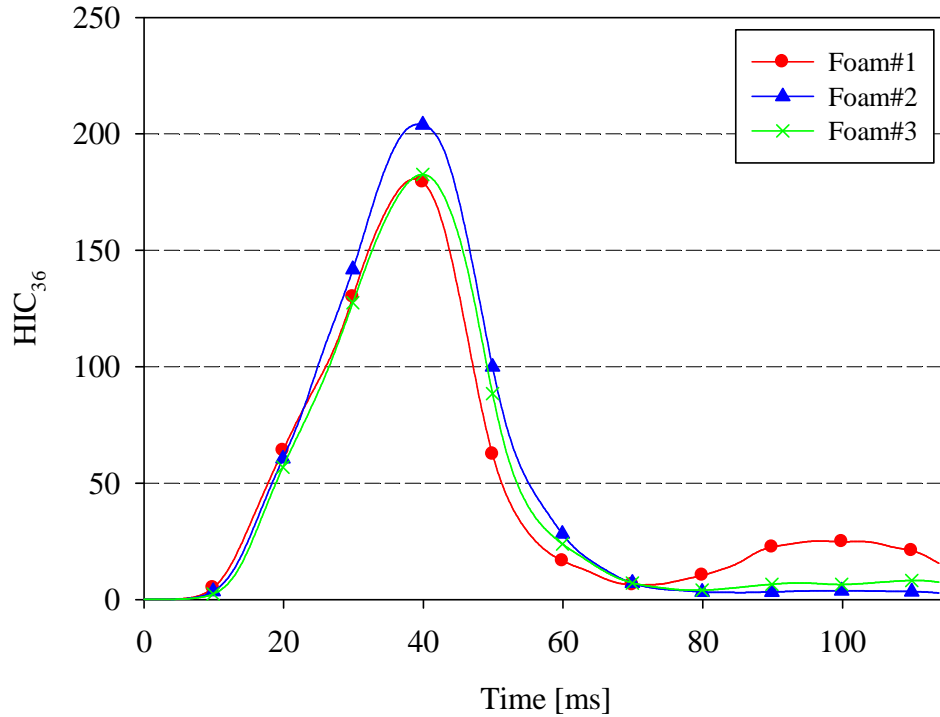
Figure 6-5. CRS with three foam candidates HIC36 as a function of time – side crash.

6.3.3 Neck joint force

Figure 6-6 presents the upper neck joint forces as a function of time for three foam candidates. The maximum values of the resultant upper neck forces predicted by the simulations occurred at t = 50 ms with values of 281 N, 333 N, and 367 N for Foam#1, Foam#2, and Foam#3, respectively. It should be noted that the initial values, from t = 0 ms to t = 30 ms, were similar for all three foams. After t = 40 ms, the heads started to move and contact with insert, as a result, the upper neck joint forces began to increase. Similar upper neck joint force profiles were observed for three material candidates over the first 100 ms. However, Foam#1 was predicted by the numerical model to cause lower neck joint force comparing with other two foams. This was believed due to the stiffer foam property, which reduced the head movement and resulted in lower neck force. A significant difference of upper neck joint forces was presented for the dummy in Foam#1 PPD from t = 100 ms to t = 110 ms. Based upon the numerical

66

observations shown in Figure 6-2, the increase of force was believed as a result from the contact between the head and the insert when the dummy's head rebounded back.

Figure 6-7 presents the middle neck joint forces as a function of time for three foam candidates. The maximum values of the resultant middle neck forces predicted to occur at t = 50 ms with values of 295 N, 374 N, and 407 N for Foam#1, Foam#2, and Foam#3, respectively. All three foams resulted in similar middle neck joint force profiles, except the greater force predicted for Foam#1 from t = 100 ms to t = 120 ms, when the dummy's head contacted with foam for Foam#1.

Figure 6-8 presents the lower neck joint forces as a function of time for three foam candidates. The maximum values of the resultant middle neck forces predicted to be 457 N, 465 N, and 571 N for Foam#1, Foam#2, and Foam#3, respectively.

Overall, Foam#1, the stiffest foam among these three candidates, was predicted to provide the lowest neck joint forces as the result of a smaller head movement. However the cost of high stiff foam based upon this material parametric study, it could potentially cause dummy's head rebound back more comparing with less stiff foams, and consequently introduced the second head acceleration peak, as shown in Figure 6-6, Figure 6-7, and Figure 6-8 from t = 100 ms to t = 120 ms. From the destructive tests with a pediatric head-neck conducted by Ouyang [33], the average tensile force at failure was 726 N with a minimum force at failure of 494 N and a maximum force at failure of 918 N. The predicted results from the numerical models showed that neck forces were below the minimum force at failure obtained by Ouyang's study [33], and expected a lower neck joint force when Foam#3 was utilized.
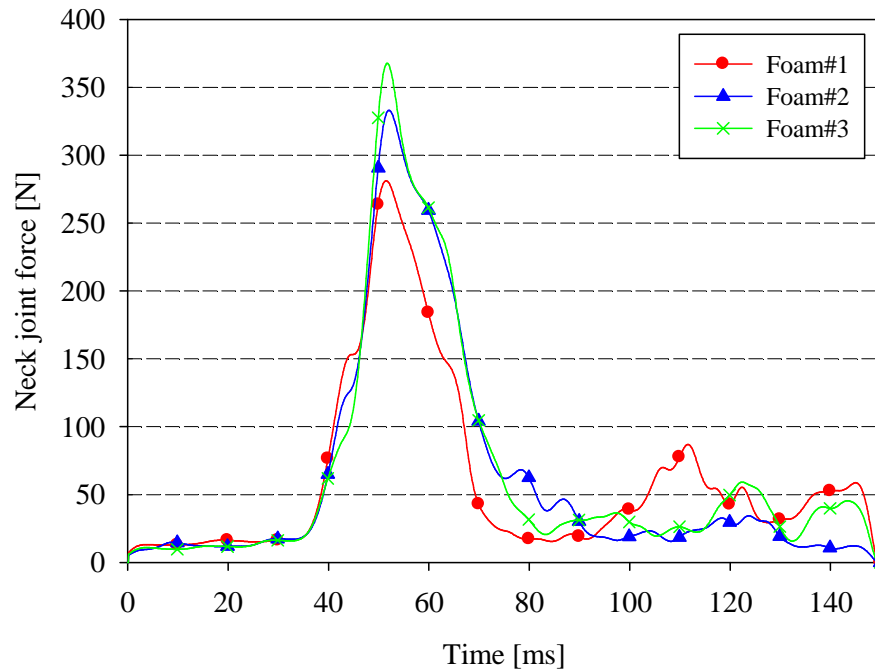
Figure 6-6. CRS with three foam candidates upper neck joint forces as a function of time – side crash.
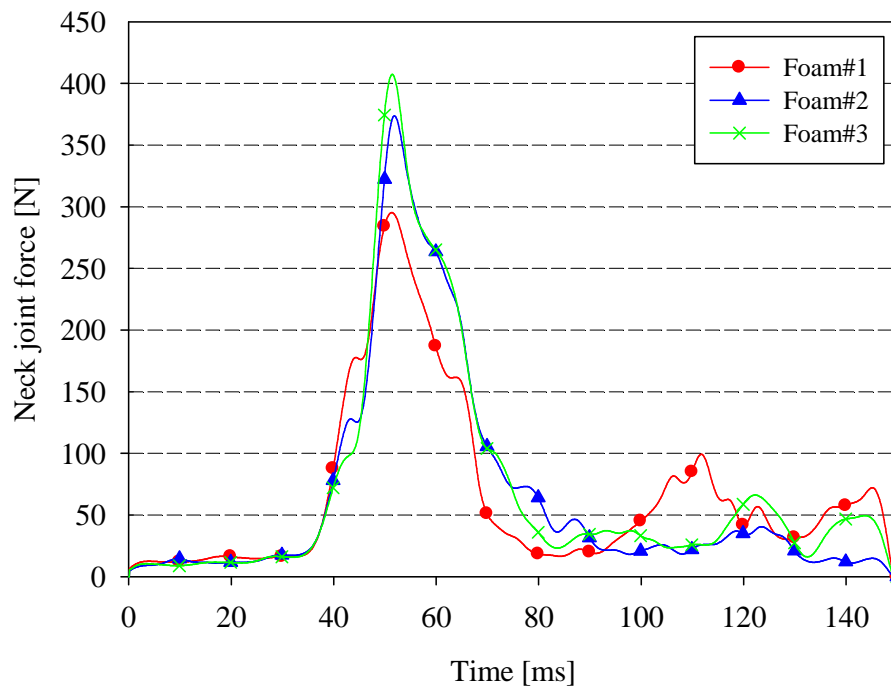
Figure 6-7. CRS with three foam candidates middle neck joint forces as a function of time – side crash.
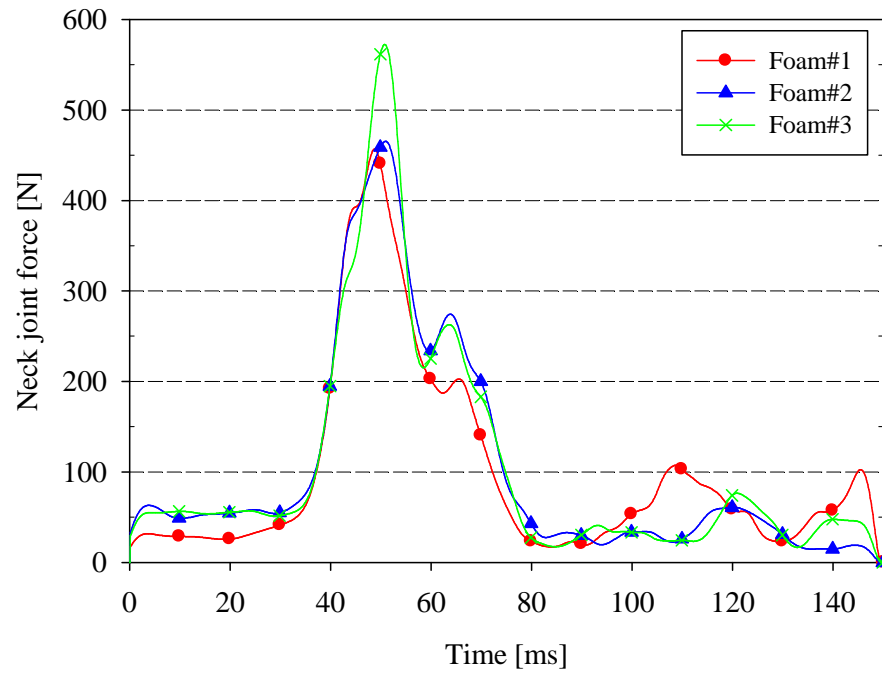
Figure 6-8. CRS with three foam candidates lower neck joint forces as a function of time – side crash.

7 PPD MATERIAL PARAMETRIC STUDY - FRONTAL CRASH

A material parametric study under frontal crash event was required to investigate the influence of different foam material on the performance of the PPD. The results from this study provided guidance of the selection of foam material. This chapter describes the procedure and numerical results of this material parametric study under front crash.

7.1 Simulation procedure

A frontal crash event was simulated, in order to test the efficacy of the PPD under a frontal crash acceleration pulse. The impact pulse was obtained by measuring the CRS displacement results from Kapoor's study [29]. The simulations completed by Kapoor utilized the CMVSS 208 acceleration pulse acquired from the accelerometers mounted in the vehicle during the experimental vehicle crash test. This method and use of data ignored the effect of different methods that were used to restrain the CRS to vehicle, for example, flexible latch, Lower Anchorage and Tether (LATCH), and rigid ISOFIX. The displacement pulse was prescribed to the CRS in the negative X-direction, while the motion of CRS in y-direction or z-direction was constrained.

7.2 Qualitative analysis

Figure 7-1 illustrates the numerical observations of the child dummy at specific instants of time through the frontal crash simulations when restrained in CRS with PPD made from three material candidates: (a) Foam#1, (b) Foam#2, and (c) Foam#3.

It should be noted that the CRS was in rear-facing configuration, thus, frontal crash will cause the dummy crash into the CRS due to mass/acceleration. At t = 0 ms, dummies were seated in their initial positions. Maximum extensions of dummies' heads were observed from the numerical results at approximately t = 55 ms and the dummy started to rebound back, head moving toward chest. Significant amount of PPD deformation was observed. The foam in the back the dummy's head was crashed significantly to dissipate dummy's kinetic energy. Noticeable separations between the PPD and CRS were observed at both t = 55 ms, and t = 90 ms for a short period (10 ms) and the PPD was settled back into CRS. It is evident from Figure 7-1 that bending of the neck, displacement of the head and torso were typically more serve for the low birth-weight infant dummy in the PPD where Foam#2 and Foam#3 were utilized.
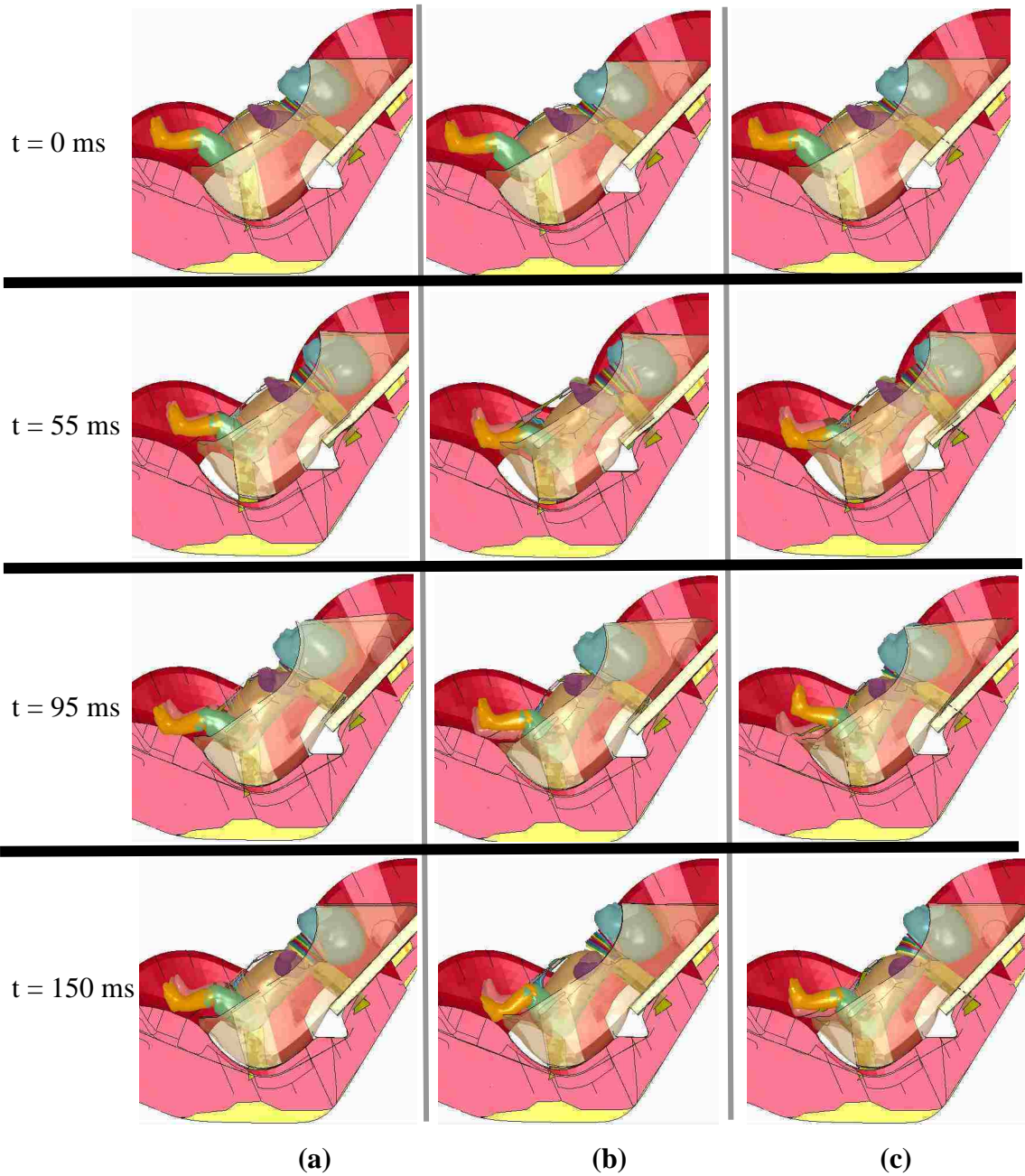
Figure 7-1. Numerical observation for CRS with foam – frontal crash:
(a) Foam#1, (b) Foam#2, and (c) Foam#3.

7.3 Quantitative analysis

7.3.1 Neck angle

The neck angles as a function of time through the frontal crash simulations are illustrated in Figure 7-2. The initial neck angle values were predicted to be 110 degrees over the first 20 ms for all three foams. At t = 68 ms, the first peak neck angles were predicted to occur. The peak neck angles were predicted to be 136, 142, and 141 degrees for Foam#1, Foam#2, and Foam#3, respectively. It should be noted that after those peak values, the dummy's head rebounded back, i.e. head moving toward chest, and consequently resulted in the reduction of the neck angles as shown in Figure 7-2 from t = 68 ms to t = 100 ms. The numerical results did not show a linear relationship between neck angle and foam stiffness. The stiffest foam among those three foam candidates, Foam#1, resulted in smallest neck angle, which indicates least head extension. However, the least stiff foam, Foam#3, caused intermediate neck angle overall. It should be noted that, the foam does not only have influence on the dummy's head but also the torso. Neck angle is determined by the kinematics of both the head and the torso. At t = 150 ms, largest peak neck angles were predicted to occur with values of 140, 146, and 150 degrees for Foam#1, Foam#2, and Foam#3, respectively.
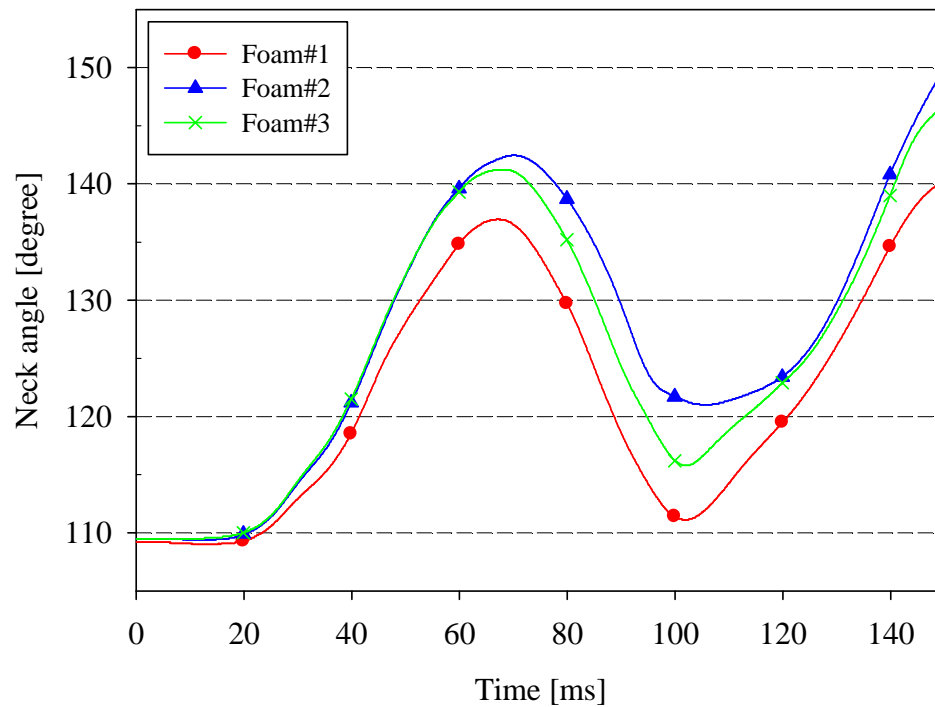
Figure 7-2. CRS with three foam candidates neck angles as a function of time – frontal crash.

7.3.2 Head acceleration

Figure 7-3 illustrates the head accelerations a function of time for the CRS with three material foams. Maximum values of the head acceleration were predicted to be 85g's, 80 g's, and 65 g's for Foam#1, Foam#2, and Foam#3, respectively. Similar head acceleration profiles were predicted for three foam candidates until t = 100 ms. A second small peak value was predicted to occur at t = 95 ms for Foam#2. Figure 7-4 presents the HIC_{36} as a function of time for three foams. The maximum values of HIC_{36} were predicted to be 370, 410, and 420 for Foam#1, Foam#2, and Foam#3, respectively. In order to estimate the injury level for dummy, the protection reference values were referenced here. To the best of author's knowledge, there is no existence of any kind of injury criteria for low birth-weight infant dummy. Due to the lack of available information, the protection reference values for Hybrid III 3-year old dummy were

utilized. The values are only applicable for frontal impact situations [34, 35]. The critical peak head acceleration is 80 g's and critical head injury criteria (HIC_{36}) is 1000. Foam#3 failed to pass with excessive peak head acceleration (over 6%). Foam#2 and Foam#1 resulted head acceleration which were equal or lower than 80 g's limit. It should be emphasized again that there is currently no injury criteria available for low birth-weight infant dummy and the protection reference values were utilized only for reference. Based upon the numerical results, the reward from stiffer PPD material was the lower peak values for head acceleration.
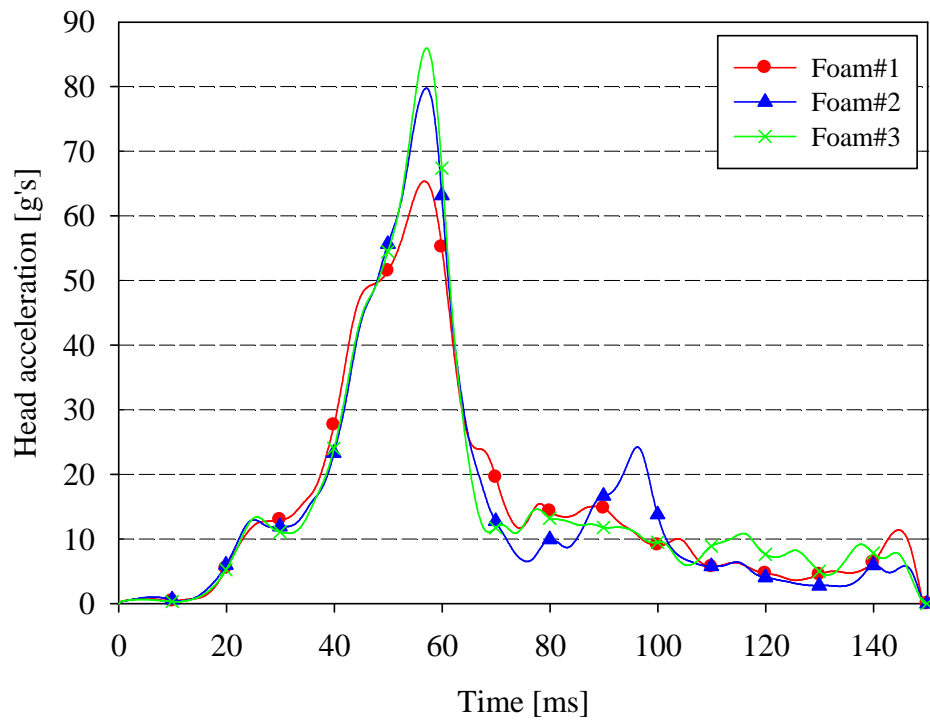
Figure 7-3. CRS with three foam candidates resultant head accelerations as a function of time – frontal crash.
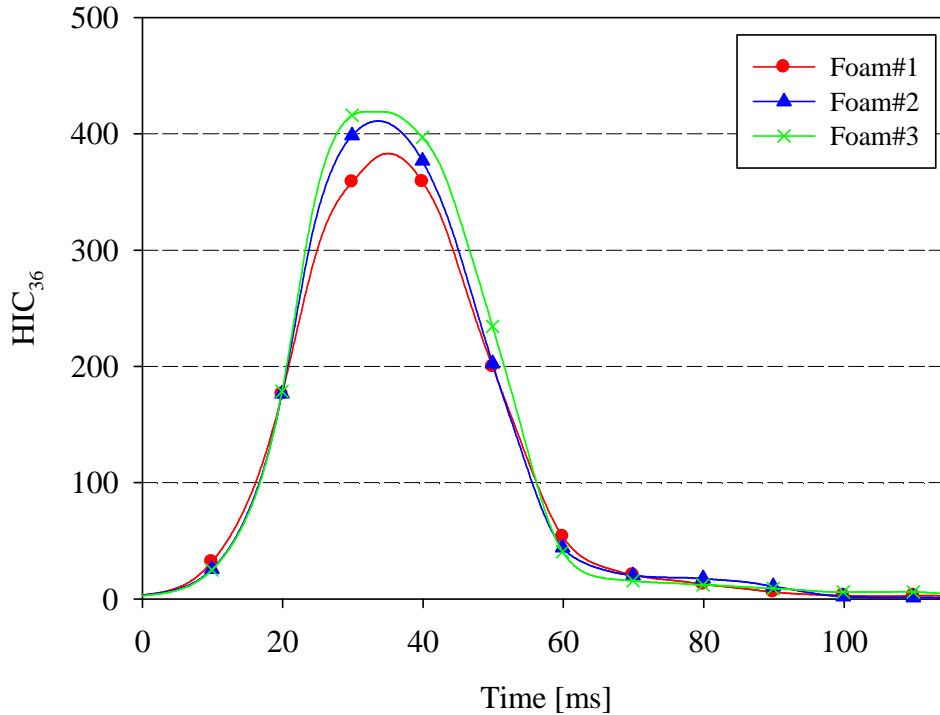
Figure 7-4. CRS with three foam candidates HIC36 as a function of time – frontal crash.

7.3.3 Neck joint force

Figure 7-5 presents the upper neck joint forces as a function of time for three foam candidates. At t = 20 ms, the upper joint forces started to ramp up to their maximum values. The maximum values of the resultant upper neck forces predicted by the simulations occurred at t = 58 ms with values of 230 N, 255 N, and 270 N for Foam#1, Foam#2, and Foam#3, respectively. After the peak values, the head started rebounding forward, i.e. the head moving toward chest. Similar upper neck joint force profiles were observed for Foam#2 and Foam#3. At t = 80 ms, the upper neck joint force for Foam#2 reached a valley point, unlike other tow foam materials, after that a noticeable increase of upper joint force was predicted by the numerical model. Based upon the numerical observation and the joint force curves, foam Foam#2 provided less

control of the neck joint force during the rebounding phase after the maximum neck joint force occurred.

Figure 7-6 presents the middle neck joint forces as a function of time for three foam candidates. The maximum values of the resultant middle neck forces predicted to occur at t = 58 ms with values of 280 N, 300 N, and 320 N for Foam#1, Foam#2, and Foam#3, respectively. All three foams resulted in similar middle neck joint force profiles, except the greater force predicted for Foam#2 at approximately t = 95 ms.

Figure 7-7 presents the lower neck joint forces as a function of time for three foam candidates. The maximum values of the resultant middle neck forces predicted to be approximately 400 N, 670 N, and 610 N for Foam#1, Foam#2, and Foam#3, respectively. The peak resultant lower neck joint forces were predicted to be significantly higher for Foam#2 and Foam#3. Moreover, second peak values were also predicted to occur at t =95 ms for Foam#2.

Overall, Foam#1, the stiffest foam among these three candidates, was predicted to provide lowest neck joint forces as a result of smaller head movement. From the destructive tests with the pediatric head-neck conducted by Ouyang [33], the average tensile force at failure was 726 N with minimum force at failure of 494 N and maximum force at failure of 918 N. In accordance to Ouyang's results, there was high risk of serve injury of lower neck joint when foam Foam#2 and Foam#3 were utilized. Both lower neck joint forces were higher than the minimum force at failure.
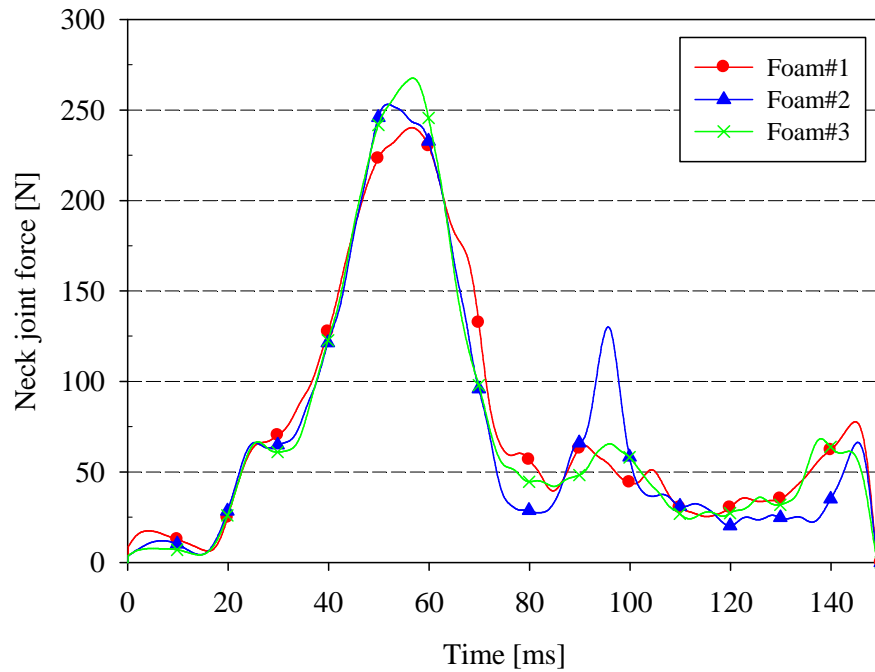
Figure 7-5. CRS with three foam candidates upper neck joint forces as a function of time – frontal crash.
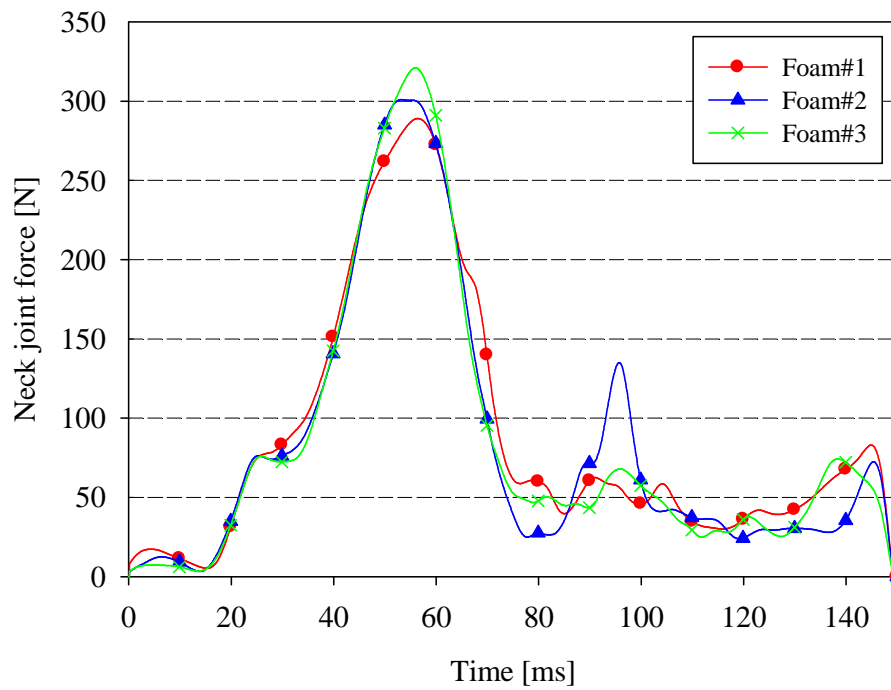
Figure 7-6. CRS with three foam candidates middle neck joint forces as a function of time – frontal crash.
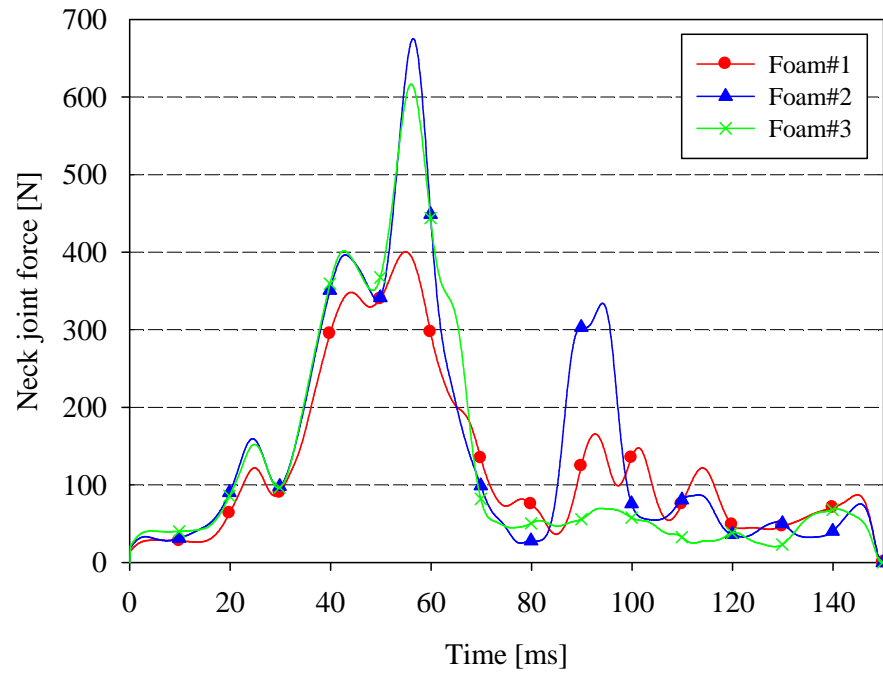
Figure 7-7. CRS with three foam candidates lower neck joint forces as a function of time – frontal crash.

8 PPD MATERIAL PARAMETRIC STUDY - NORMAL DRIVING

The primary function of the PPD is to keep low birth-weight infants in respiratory stability during daily driving. A number of on-road in-vehicle tests were conducted to collect essential data information to mimic what CRS experiences during daily driving. Three typical scenarios, which are referred to as normal driving conditions, were selected to investigate the influence of the PPD on infants. Those scenarios were braking, roundabout turn, and sharp-turn conditions. Procedures, results, and discussions of the tests were detailed described in Chapter 4. This chapter discusses the material parametric study under normal driving conditions and the results are presented.

8.1 Simulation procedure

The acceleration pulses were applied to the numerical model of the CRS at the location where the accelerometer was mounted in the physical apparatus. Figure 8-1 in chapter 4 illustrates the location. Some assumptions were made regarding the applied acceleration. For braking scenario, only longitudinal acceleration (x-direction) was imposed on CRS as shown in Figure 8-2, and the motion in global y- and z-direction was restrained. For roundabout scenario, the acceleration pulse was prescribed in latitudinal direction (y-direction), restraining in global x- and z-direction, shown in Figure 8-3. For sharp-turn scenario, accelerations in all three directions were included due to the native of the motion, which involves deceleration in longitudinal direction, latitudinal acceleration due to turning, and vertical acceleration due to the existence of a gutter. Details of those scenario and data acquisition were described in Chapter 4.
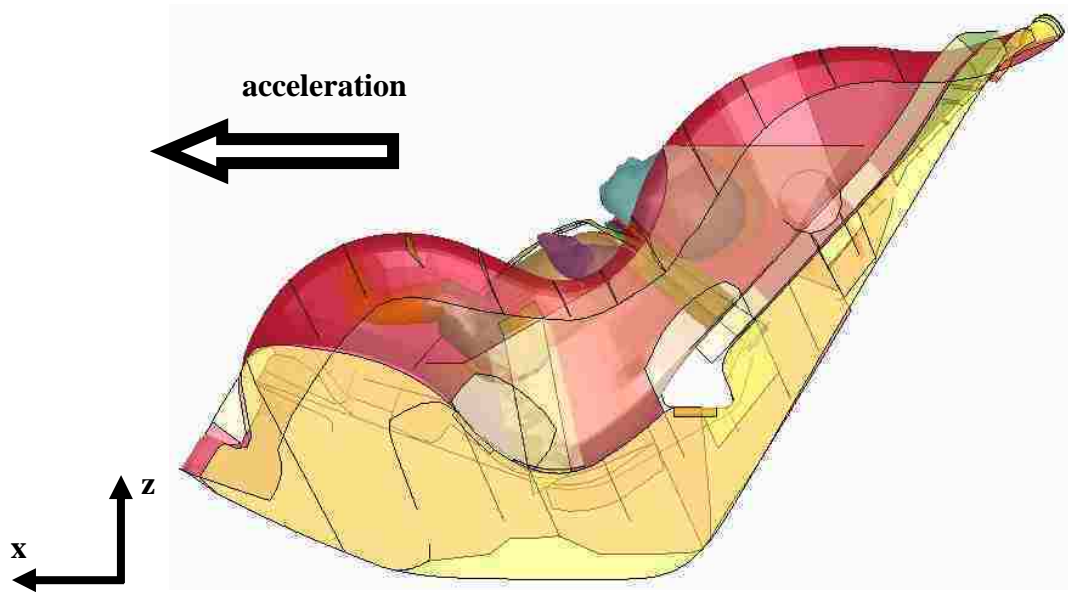
Figure 8-1. The application of acceleration for braking event.
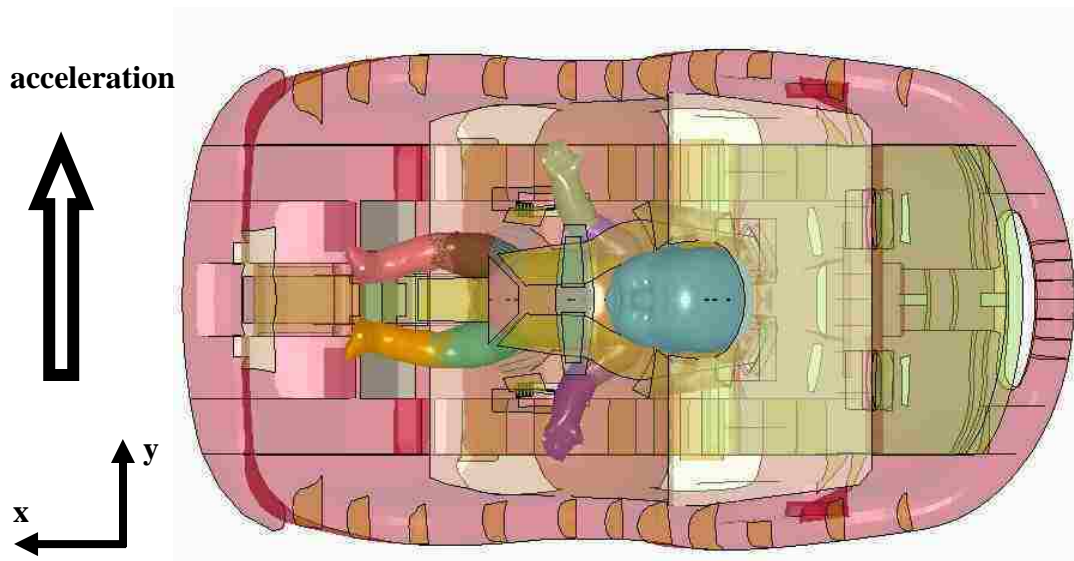
Figure 8-2. The application of acceleration for roundabout turning event.
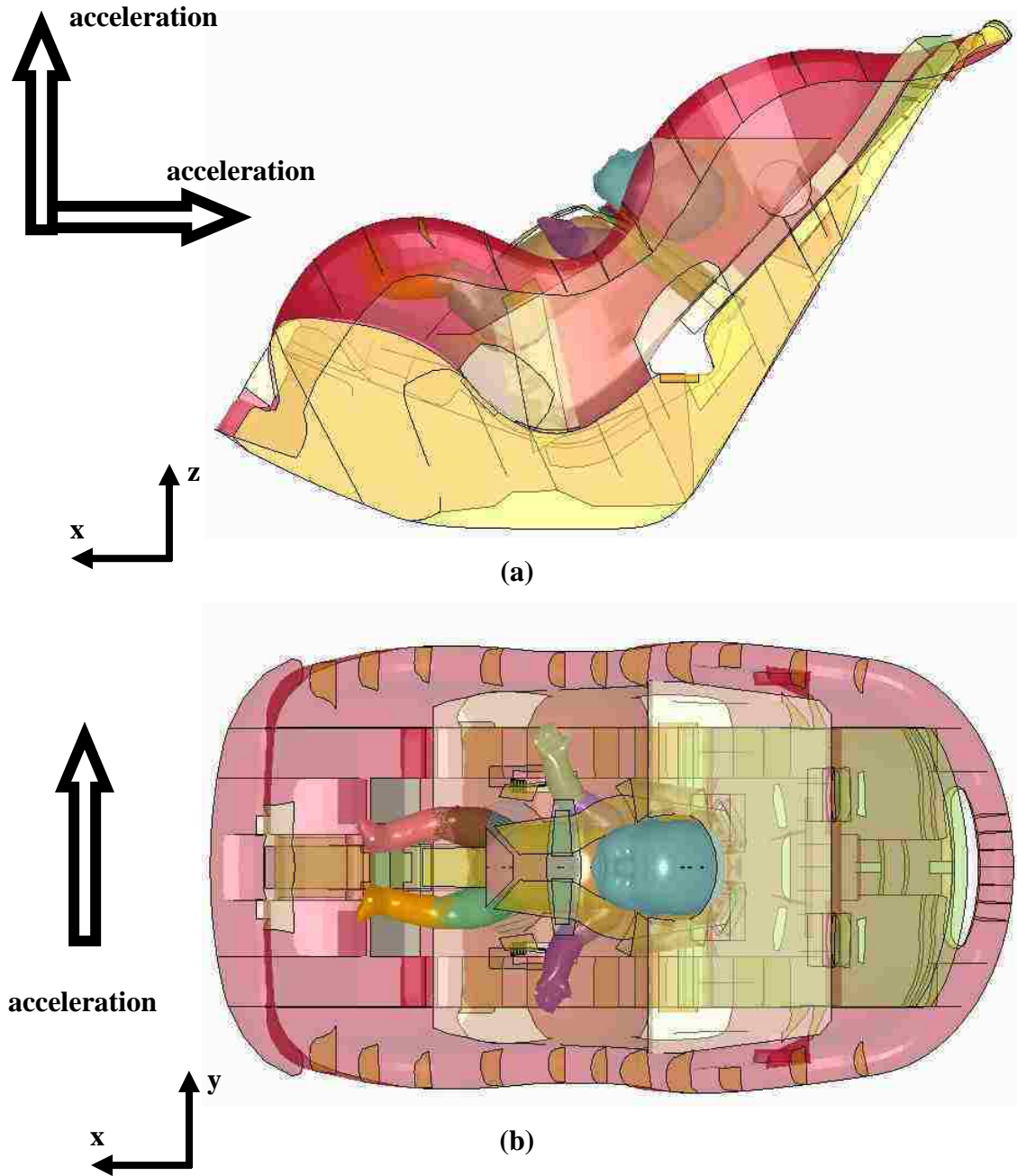
Figure 8-3. The application of acceleration for sharp-turn event:

(a) side view; (b) top view.

The timestep of this finite element model in order to keep the simulation in stable state was typically in the order of $1*10^{-7}$ second. This is acceptable for a crash event simulation, since a crash event typically elapses for 100 to 150 milliseconds. However, the duration of normal driving condition investigated in this study was typically in the order of seconds: 2~3 seconds for braking event; 10 seconds for roundabout event; and

4~6 seconds for sharp-turn event. Inevitable, it has highlighted the difficulties that are like to arise when utilizing the crash finite element model directly to simulate a normal driving condition due to unreasonable run time for this parametric study, at order of hundred of hours for one simulation. Therefore, both mass scaling and time scaling techniques were utilized. Mass scaling refers to a technique whereby non-physical mass is added to a structure in order to achieve a larger explicit timestep [36]. Both techniques always carry the burden of potentially affecting the results. However, those two techniques were justified and accepted considering following facts of this study:

1. In the normal driving condition, velocity is low and the kinetic energy is small. Unlike side and frontal crash events discussed in previous chapters, the input accelerations for normal driving condition were below 1 g while it usually reached 60 g's for crash events.

2. There is no mass added into low birth-weight infant dummy model. The infant dummy model was modeled using rigid material. The manner utilized in this study was to add mass to only those elements whose timestep would be less than TSSF*abs(DT2MS) [36]. The added mass was 137 kg, and the physical mass was 6.25 kg. The ratio was 21.9.

3. This parametric study intended to investigate how different foam materials can vary the performance of the PPD. The selection and the judgement of the foam materials did not sorely depend on the absolute values. The comparison of the results among those materials was more important.

4. The animations were carefully observed to ensure there was no unexpected or unrealistic behaviour occurring.

The normal driving condition simulations were completed by utilizing finite element analysis code LS-DYNA version 971 revision 50638 double precision (I8R8) on a personal computer with a Dual Core AMD opteron™ Processor 285 2.6 GHz (2 processors), with the system having 12 Gigabytes of random access memory (RAM), using a 64-bit Windows 7 operating system. The double precision was utilized due to the excessive simulation cycle. It was suggested by Livermore Software Technology Corporation (LSTC) the utilization of double precision when the number of simulation is over 500,000 cycles to reduce the round-off error. This type of simulations typically took approximately 50 hours to complete.

8.2 Braking scenario

Figure 8-4 illustrates the neck angles, which was defined in chapter 4, as a function of time under braking condition. It should be noted that the initial neck angles were similar for three material candidates at approximately 109 degrees.
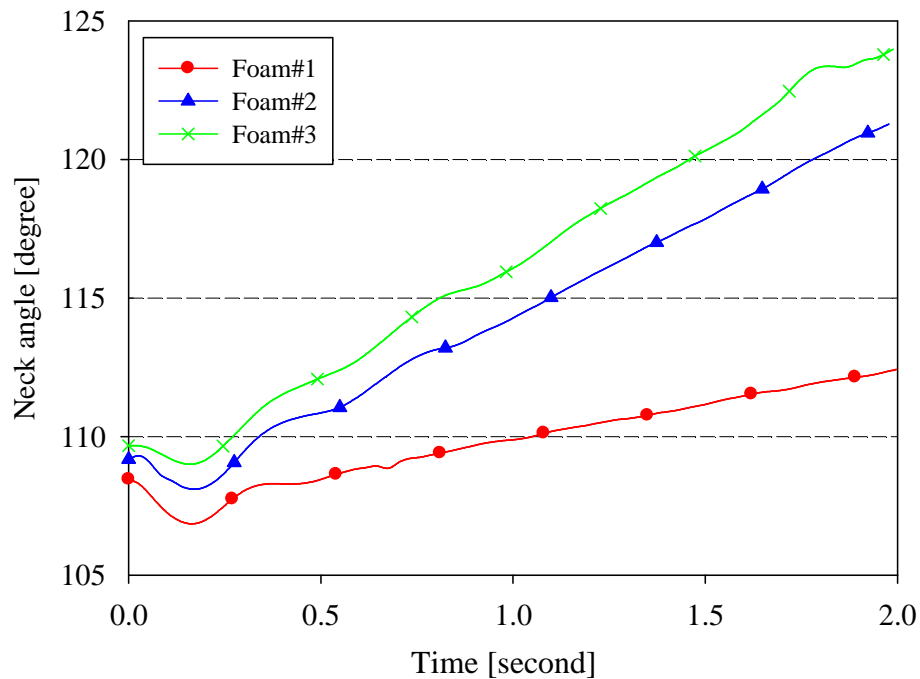
Figure 8-4. Neck angle for three foam candidates as a function of time – braking.

Three neck angle profiles presents similar pattern. They decreased slightly over first 0.2 second, and kept increasing. The final neck angles predicted by the numerical simulations were 112, 122, and 124 degrees for Foam#1, Foam#2, and Foam#3, respectively. The results indicated that the neck angle is inversely proportional to the foam stiffness under the braking condition. The foam with higher stiffness provided smaller neck angle. It should be emphasized that regardless of which foam material was used the PPD was able to keep low birth-weight dummy in extension posture (when neck angle was above 90 degrees). The study by Wilson et al. [26] indicated that neck extension lowered closing pressure, making the airway more resistant to collapse.

8.3 Roundabout scenario

Figure 8-5 shows the neck angles as a function of time under roundabout driving condition. Three foam material candidates resulted in similar neck angle history profiles, whereas the neck angle dropped 4 degrees at t = 0.2 second and was able to increase and keep in a constant level. It was observed that the resultant neck angles were very close for three foam material candidates with maximum difference of 2 degrees under the roundabout driving event. Again, the PPD was predicted to make the dummy keep in neck extension posture over the entire event and the stiffer foam resulted in smaller neck angle.
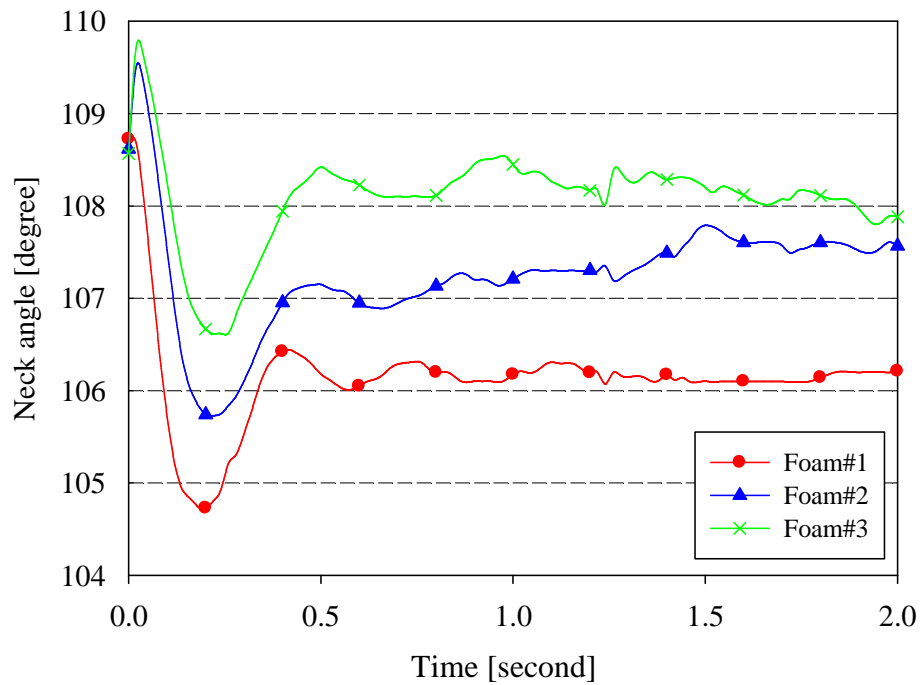
Figure 8-5. Neck angle for three foam candidates as a function of time – roundabout.

8.3 Sharp-turn scenario

Figure 8-6 illustrates the neck angles as a function of time under sharp-turn scenario. There was no significant difference in neck angles observed from the numerical results for three foam materials. The neck angles decreased from initial value of 109 degrees down to 85 degrees. Due to the direction of the acceleration pulse from this event, shown in Figure 8-3, the dummy's head moved away from the PPD, thus no significant difference among these three foam materials was expected.
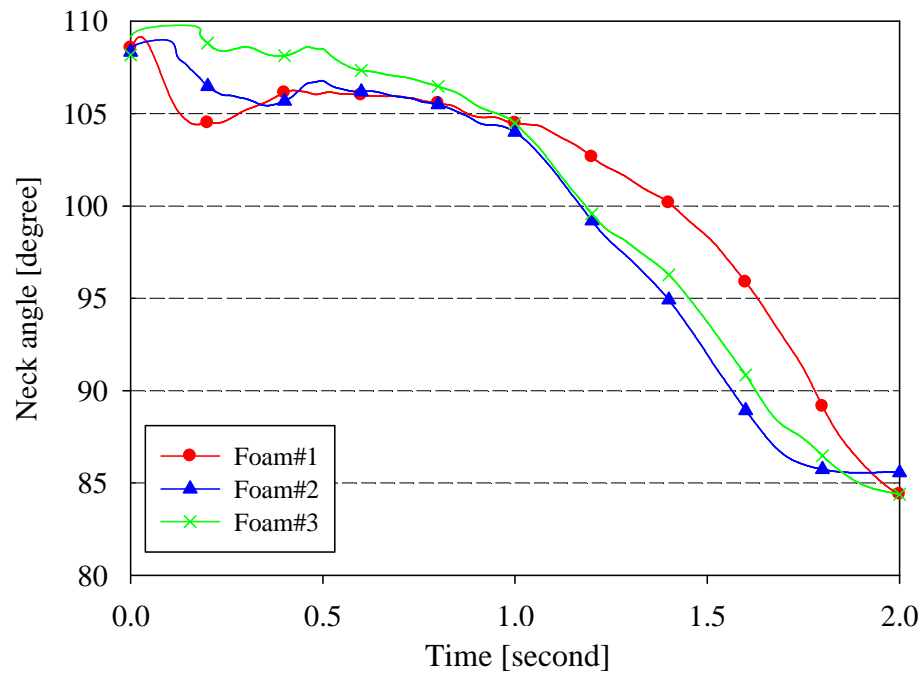
Figure 8-6. Neck angle for three foam candidates as a function of time – sharp-turn.

9 PPD GEOMETRY PARAMETRIC STUDY

Due to weak neck structure and maculation in low birth-weight infants, the geometry of the PPD plays an important role in determining the neck extension/flexion level. This chapter presents a PPD geometry parametric study conducted to focus on the influence of PPD geometry on the protection performance. Three different versions of PPD were created to result in different infant neck extension/flexion level when low birth-weight infant was constrained in the PPD. Figure 9-1 illustrates the infant dummy with different neck-extension levels when restrained in the PPD. Three PPD versions provided three different initial neck angles: 100 degrees, 110 degrees, and 120 degrees. In the later texts, three PPD geometries are designated to PPD100, PPD110, and PPD120 which are corresponding to the initial neck angles. In this study, the recline angle of dummy's torso remained at 30 degrees as shown in Figure 9-1. The different neck angles were achieved by modifying the vicinity of the infant dummy's head. Removal or addition of foam caused various neck angles when dummy rested on PPD.

The study conducted by Wilson et al. [26] concluded that neck flexion tends to cause airway to collapse and neck extension is beneficial for infants up to a neck angle of 150 degrees. All three geometries were expected to keep infant dummy to maintain in extension posture. Moreover, in order to assure that PPD does not compromise CRS protection performance when infants are subjected to aggressive acceleration, like during the crash events, this geometry parametric study was conducted to seek out the optimized geometry. The following sections describe the simulation procedures and the numerical results are presented.
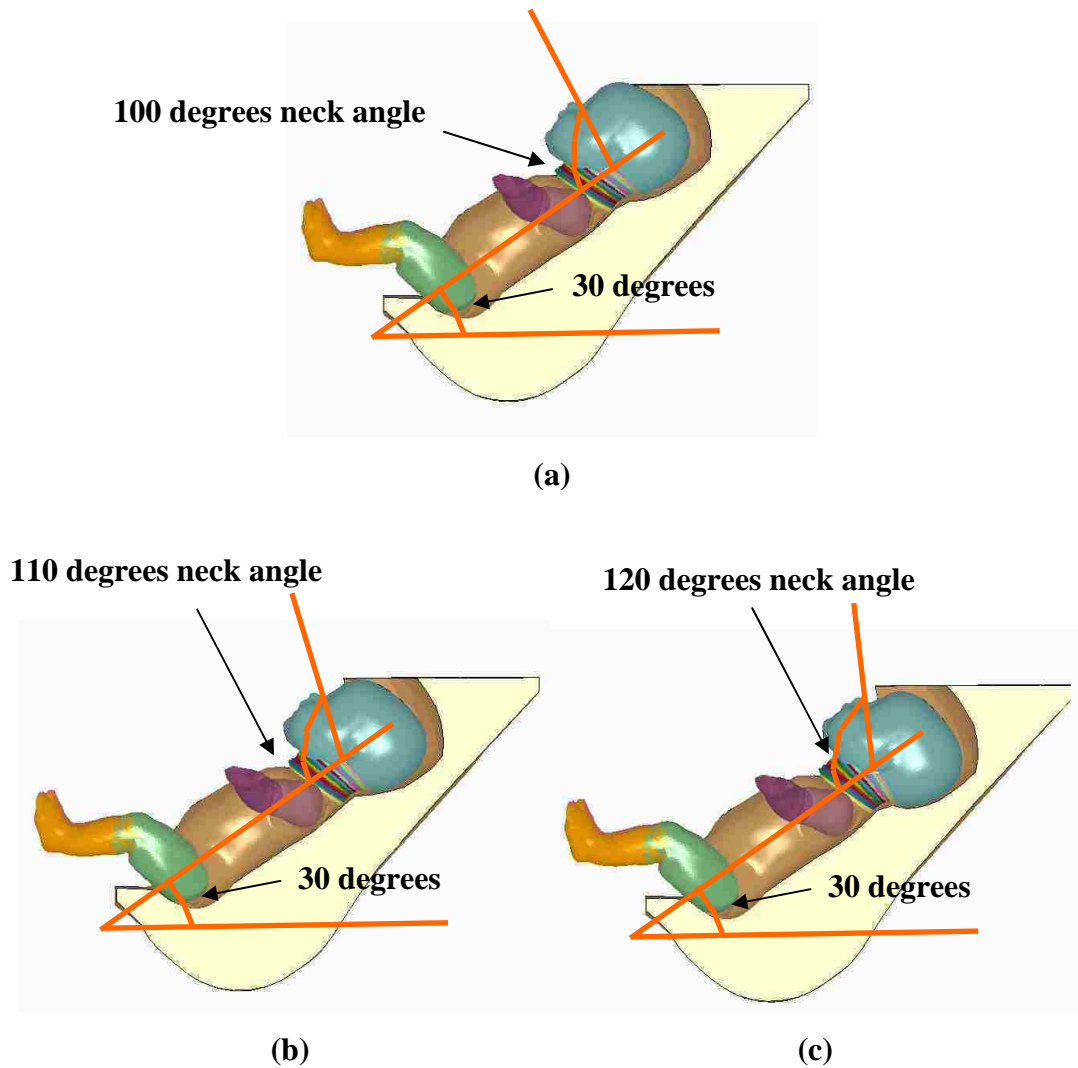
Figure 9-1. Different dummy neck-extension levels in three PPD geometries: (a) PPD100, (b) PPD110, and (c) PPD120.

9.1 Simulation procedure

It should be noted that the PPD used for the material parametric study described in previous chapters provided the initial neck angle of 110 degrees. All five scenarios were simulated and they were: side crash, frontal crash, braking, roundabout, and sharp-turn scenario. All the finite element model setup and simulation procedure, including the element formulation, contact definition, prescribed acceleration/displacement pulses were identical to the previous simulations so that the results were only affected by the difference of the PPD geometry.

The simulations were completed by utilizing the finite element analysis code LS-DYNA version 971 revision 50638 single precision (I4R4) for side crash and frontal crash simulation, and double precision (I8R8) for normal driving conditions, on a personal computer with an Intel(R) Core™2 Duo CPU T9600 with an internal clock speed of 2.8 GHz, with the system having 3.00 Gigabytes of random access memory (RAM), using a 64-bit Windows 7 operating system. Typically this type of simulation took approximately 6 hours to complete for a crash event and approximately 40 hours for a normal driving event.

9.2 Side crash
9.2.1 Neck angle

Figure 9-2 illustrates the neck angle profiles as a function of time under side crash event for three different PPD geometries. As expected, three PPD led to different initial neck angles. As shown in Figure 9-2, the initial neck angles were approximately 102, 110, and 120 degrees. Similar profiles were predicted by numerical models. Maximum neck angles were predicted to occur at t = 70 ms with maximum values of 116, 120, and 128 degrees for PPD100, PPD110, and PPD120, respectively. The final neck angles were approximately 96 degrees for all three PPD geometries. The similar finial neck angle was believed resulted from the constrained of the rigid dummy model, which did not allow any further movement of the head.
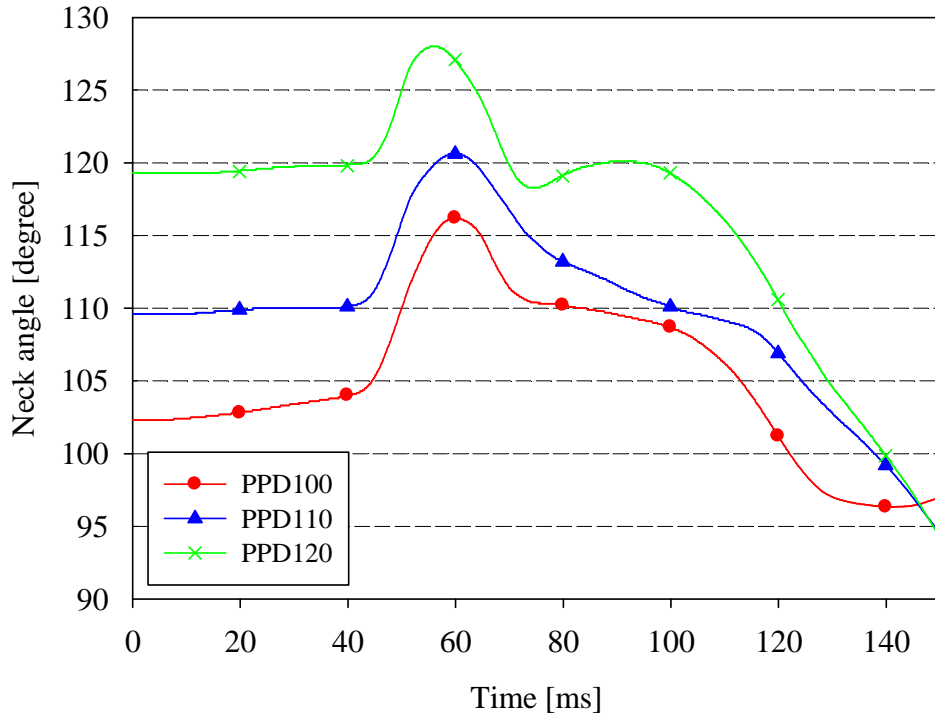
Figure 9-2. Three PPD geometries neck angles as a function of time – side crash.

9.2.2 Head acceleration

No significant differences in head acceleration profiles were predicted for three different PPD geometries. Figure 9-3 presents the head acceleration profiles as a function of time. The peak head accelerations occurred at t = 50 ms with values of 60 g's for both PPD100 and PPD110, and 55 g's for PPD120. The numerical results predicted fairly similar head acceleration profiles for three PPD geometries. The head accelerations were able to ramp down to 10 g's after t = 80 ms. Figure 9-4 illustrates the HIC_{36} profiles as a function of time. The maximum HIC_{36} values were predicted to be 185, 180 and 210 for PPD100, PPD110, and PPD120.

Figure 9-3. Three PPD geometries resultant head accelerations as a function of time - side crash.
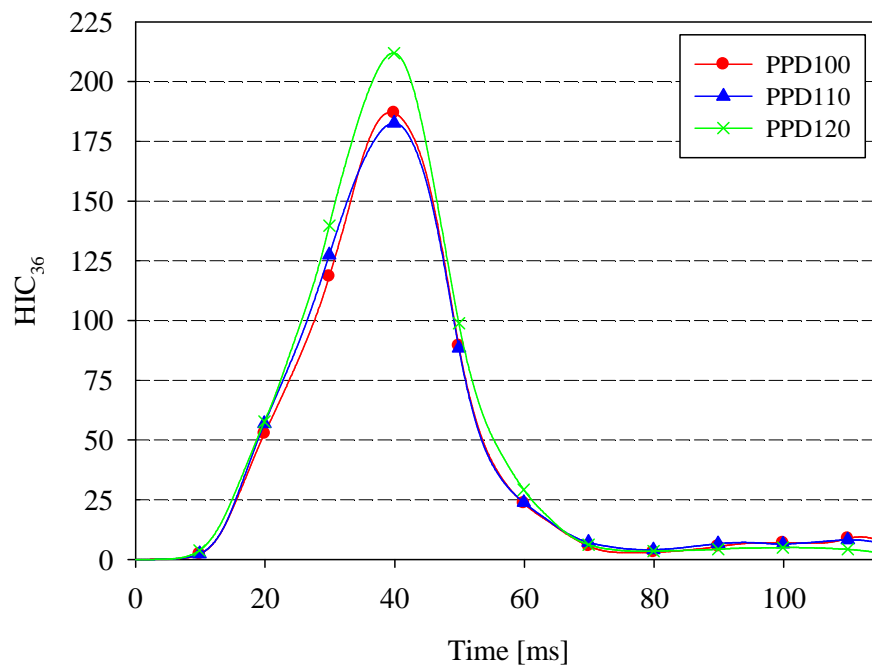
Figure 9-4. Three PPD geometries HIC_{36} as a function of time – side crash.

9.2.3 Neck joint force

Figure 9-5, Figure 9-6, and Figure 9-7 exhibit upper, middle, and lower neck joint forces as a function of time, respectively. Three PPD geometries were predicted to result in similar neck joint forces. For the upper neck joint force, PPD110 resulted largest peak neck joint force of 360 N while peak values of 300 N and 340 N were predicted for PPD100 and PPD120, respectively. The upper neck joint forces dropped and kept at a level of approximately 25 N after t = 80 ms. The maximum middle neck joint forces were predicted to be 330 N, 400 N, and 360 N for PPD100, PPD110, and PPD120, respectively. For the lower neck joint forces, the maximum neck joint forces presented at t = 50 ms with values of 500 N, 560 N, and 510 N for PPD100, PPD110, and PPD120, respectively.

Overall, three PPD geometries resulted in similar neck joint forces profile under the side crash simulation. In terms of the peak values, no large variations were predicted for three PPD geometries, 60 N for upper neck joints (between 300 N and 360 N); 70 N for middle neck joints (between 330 N and 400 N); 60 N (between 500 N and 560 N). Ouyang's [33] study indicated in his report that based upon the that the destructive tests with the pediatric head-neck complexes, the average force at failure was 726 ± 171N with a minimum force of 494 N. Although the neck joint forces predicted by the numerical models were well below the average force at failure, there is still chance for lower neck joints to failure since they were above the minimum force at failure found by Ouyang[33].

Figure 9-5. Three PPD geometries upper neck joint forces as a function of time – side crash.

Figure 9-6. Three PPD geometries middle neck joint forces as a function of time – side crash.

Figure 9-7. Three PPD geometries lower neck joint forces as a function of time – side crash.

9.3 Frontal crash

Figure 9-8 illustrates the numerical observations of the infant dummy during the frontal impact simulations when restrained in three PPD geometries (PPD100, PPD110, and PPD120). At t = 0 ms, the observed initial neck-extension levels were expected, which reflected the different PPD geometries. At t = 55 ms, maximum head extrusions were observed and maximum head accelerations were predicted as described in the subsequence section. At t = 80 ms, the contact between the dummy's head and the side wing of the PPD was observed for PPD100 when the head rebounded back after the maximum extrusion.
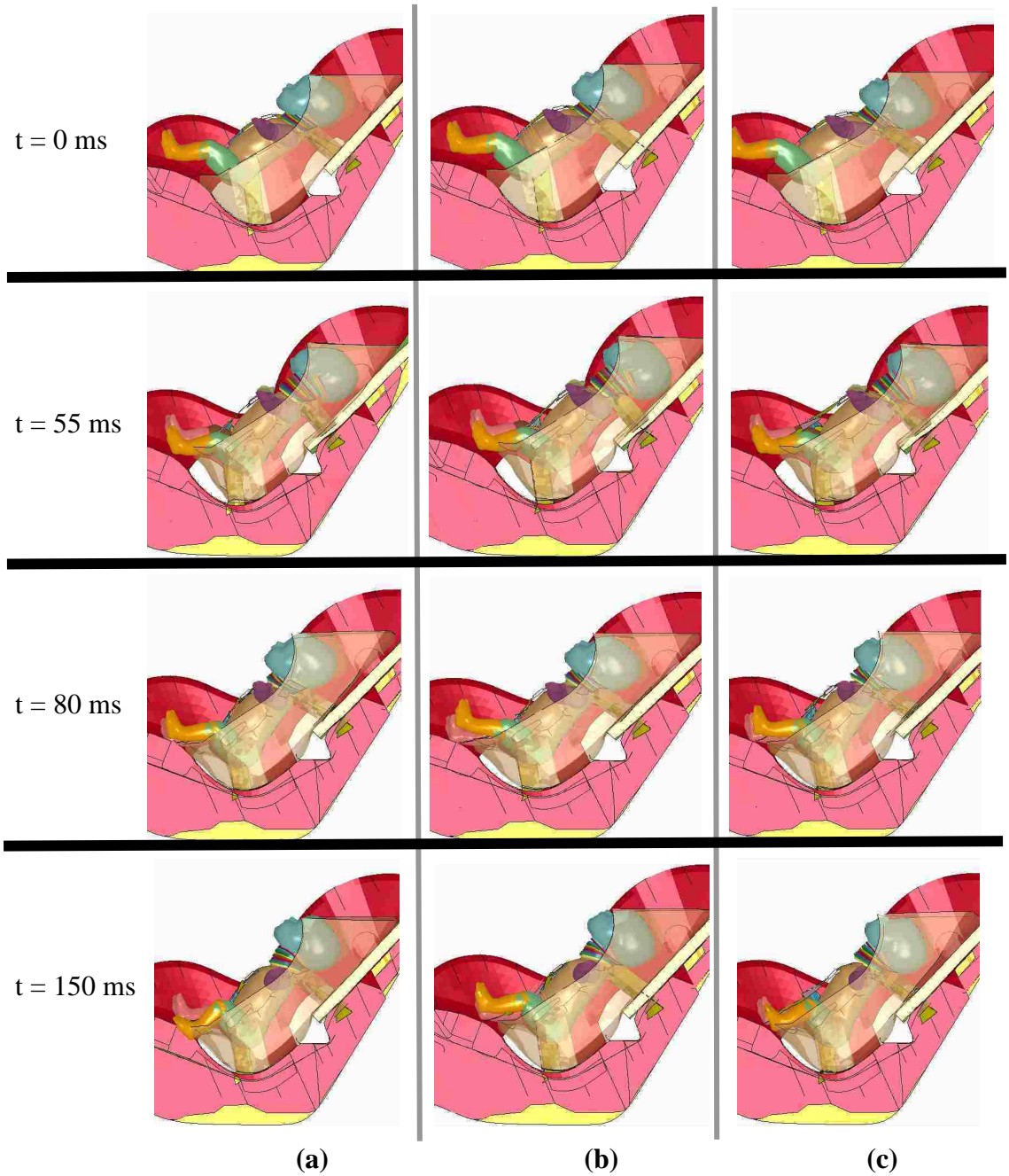
Figure 9-8. Numerical observation for PPD geometry study – frontal crash:
(a) PPD100, (b) PPD110, and (c) PPD120.

9.3.1 Neck angle

The neck angle profiles as a function of time for three PPD geometries under the frontal crash scenario were illustrated in Figure 9-9. The first peak values occurred at t = 70 ms with maximum value of 139 degrees, 142 degrees, and 152 degrees for PPD100, PPD110, and PPD120, respectively. After t = 70 ms, dummy's head rebounded toward to chest and resulted in the reduction of the neck angle. The second peak values occurred at the end with values of 145 degrees, 146 degrees, and 160 degrees for PPD100, PPD110, and PPD120, respectively. The PPD120 resulted in a high neck extension level in comparison with other two geometries. This can potentially lead to the hyper-extension issue or over-extension of the neck.
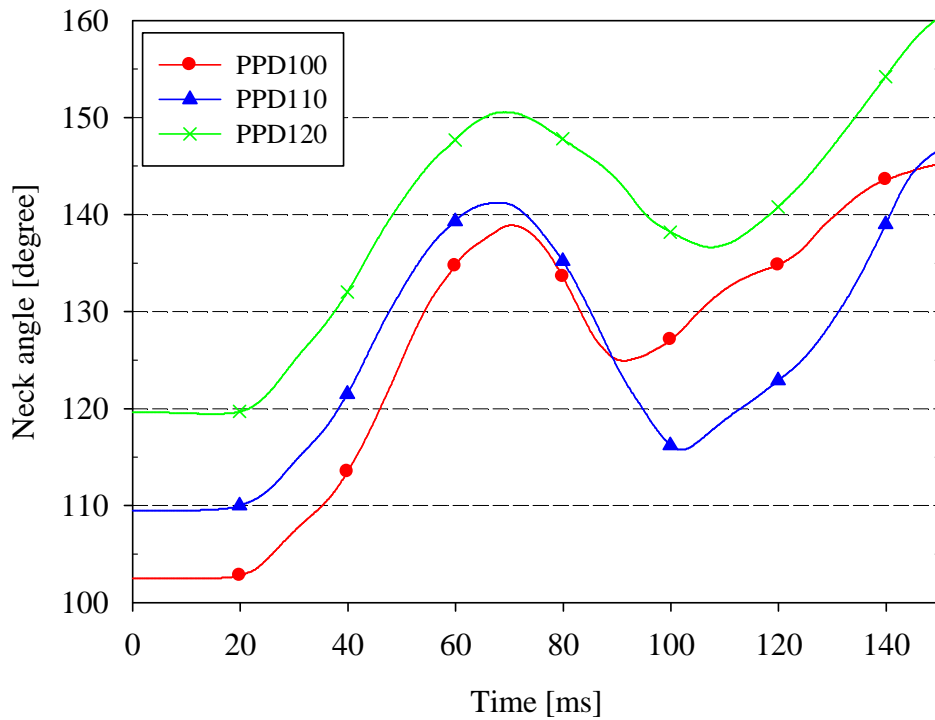
Figure 9-9. Three PPD geometries neck angles as a function of time – frontal crash.

9.3.2 Head acceleration

Figure 9-10 illustrates the resultant head acceleration profiles as a function of time for three PPD geometries under frontal crash scenario. The maximum head accelerations were predicted to be 85 g's for both PPD100 and PPD120 and 80 g's for PPD100, and occurred at t = 55 ms. PPD110 and PPD120 presented fairly close head acceleration profiles throughout entire event while there was a noticeable rising of resultant head acceleration for PPD100 at t = 80 ms. From the numerical observation, this increase of head acceleration was due to the contact between the head and the side wing of PPD100 when the dummy's head bounced back. Although contacts were also observed for PPD110 and PPD120 at later time, the contacts were not as aggressive as the one observed for PPD100. Figure 9-11 illustrates HIC_{36} results predicted by the simulations. The maximum values were predicted to be approximately 500, 410, and 380 for PPD100, PPD110, and PPD120, respectively.
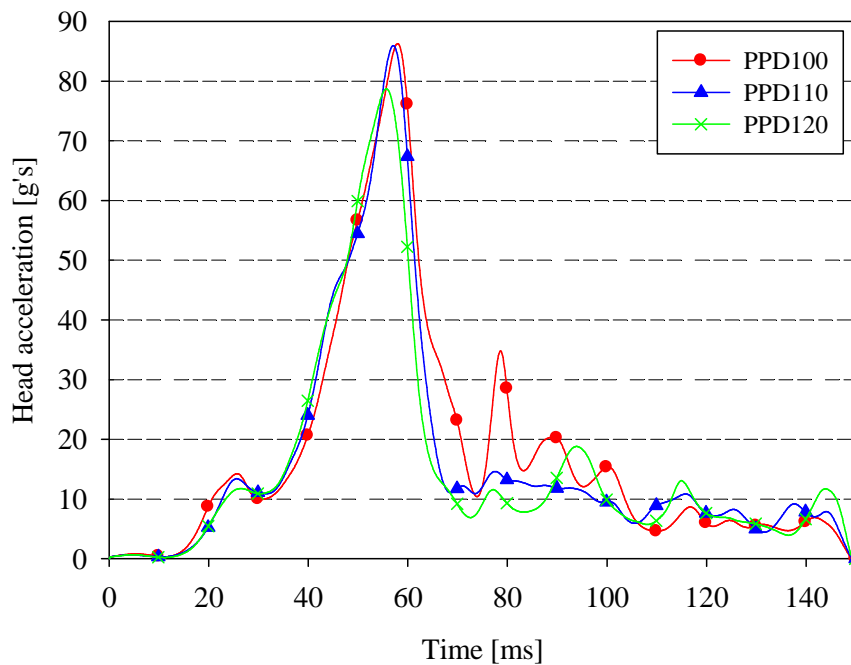
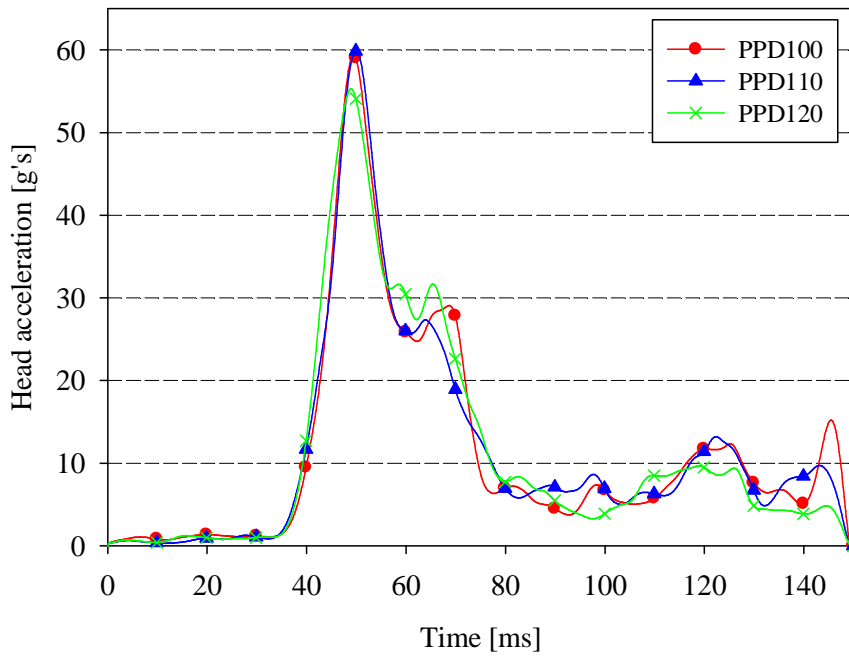**Figure 9-10.** Three PPD geometries resultant head accelerations as a function of time - frontal crash.
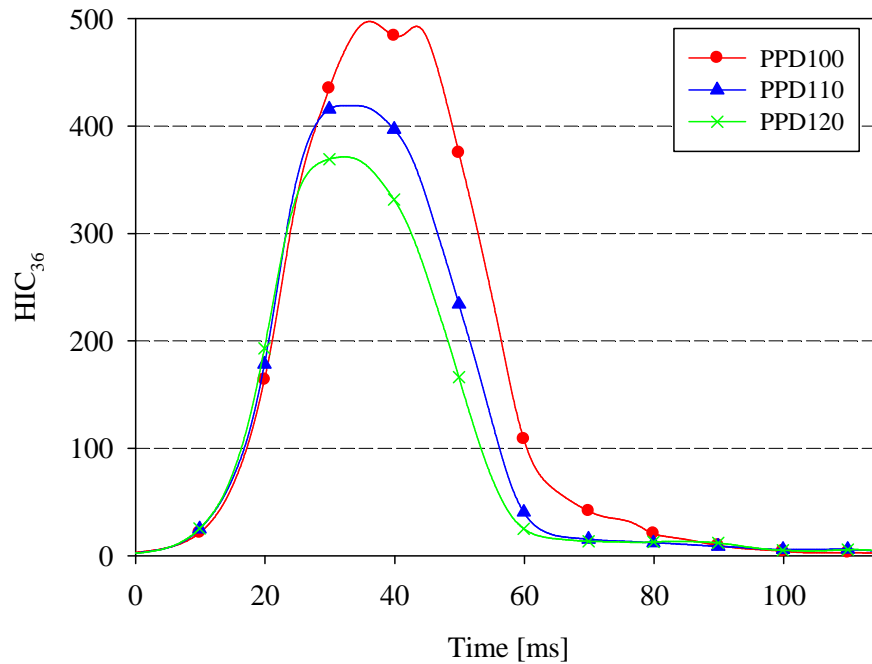
Figure 9-11. Three PPD geometries HIC$_{36}$ as a function of time – frontal crash.

9.3.3 Neck joint force

The upper, middle, and lower neck joint forces were presented in Figure 9-12, Figure 9-13, and Figure 9-14. PPD100 resulted in a largest peak upper neck joint force of 310 N while the peak upper neck joint forces were predicted to be 270 N and 230 N for PPD110 and PPD120, respectively. A noticeable increase of upper neck joint force for PPD100 was observed at t = 90 ms whereas other two PPDs kept neck joint force at lower level. More aggressive contact between the head and PPD100 was indicated by this increase. Similar results were predicted for middle neck joint forces. The maximum middle neck joint forces were predicted to be 360 N, 320 N, and 275 N for PPD100, PPD110, and PPD120, respectively. Again a noticeable rising of neck joint force was predicted for PPD 100 at t = 90 ms. Figure 9-14 illustrates the lower neck joint forces profiles. The maximum forces were predicted to be 600 N, 620 N, and 530 N for PPD100, PPD110, and PPD120, respectively. The lower neck forces exhibits similar profiles for PPD100 and PPD110. However, PPD120 exhibit very different behaviour from t = 80 ms to t = 140 ms. Three "spikes" of neck joint forces was observed for

PPD120 during this period of time whereas the other two PPDs were able to maintain neck joint forces in a relatively stable level. Based upon the numerical observation, this undamped neck joint forces phenomenon was believed to be caused by the overall kinematics of head and neck segments. The increase of the neck angle consequently led to a more recline position of the dummy's head compared with other two. Therefore, when the dummy was subjected to the frontal impact pulse, the inertia of the head caused more tension-compression behaviour for PPD120 which could contribute the uncontrollable low neck joint forces during the renounce phase.
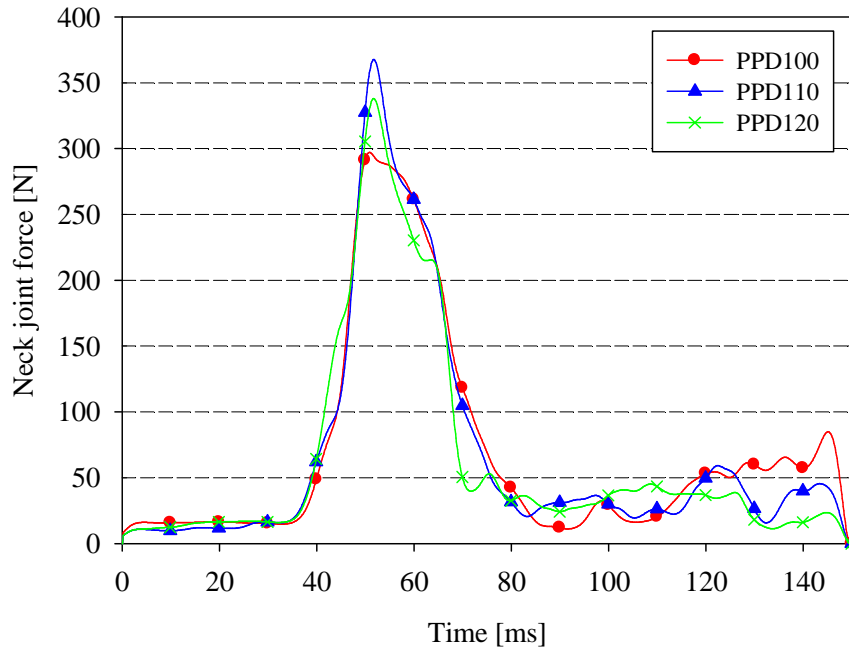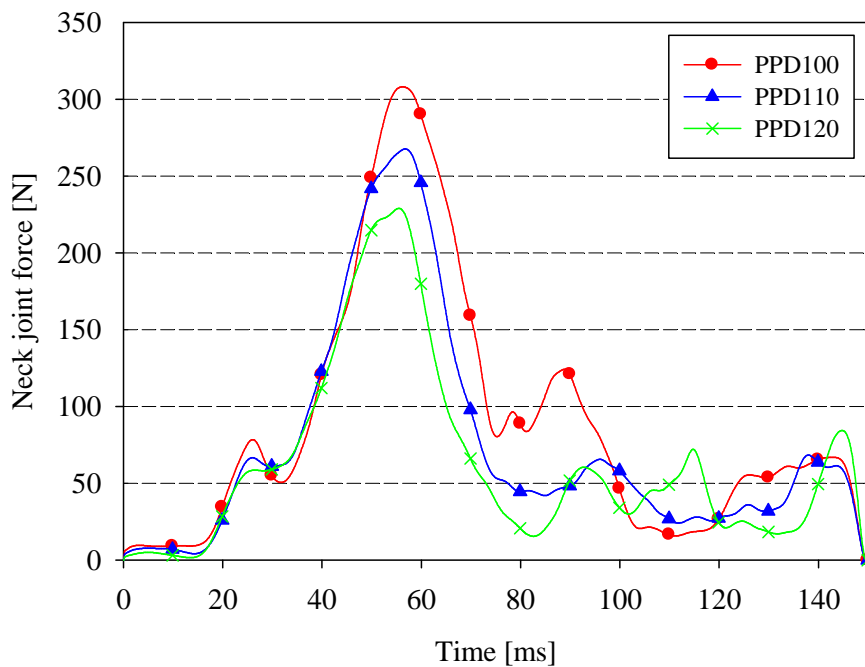

Figure 9-12. Three PPD geometries upper neck joint forces as a function of time – frontal crash.
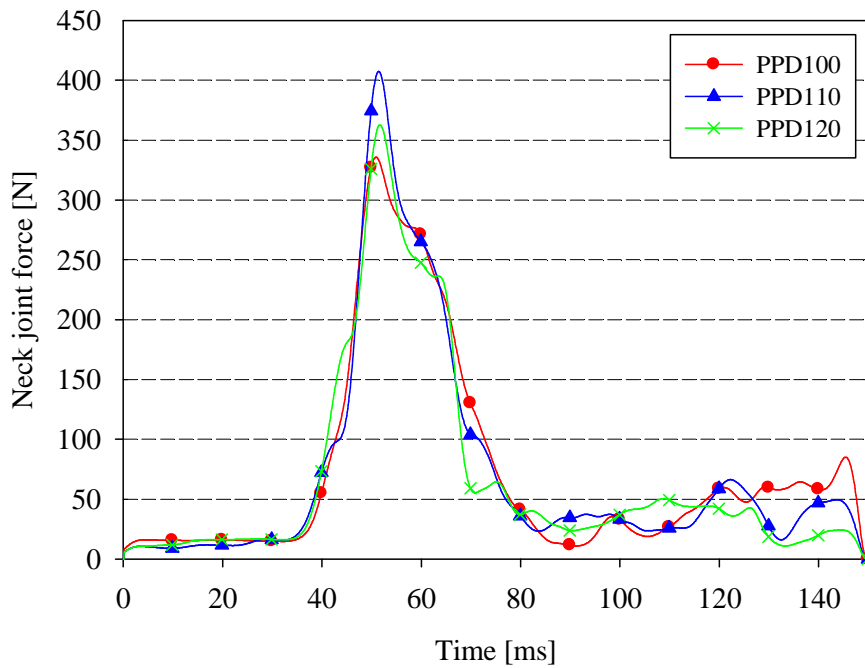
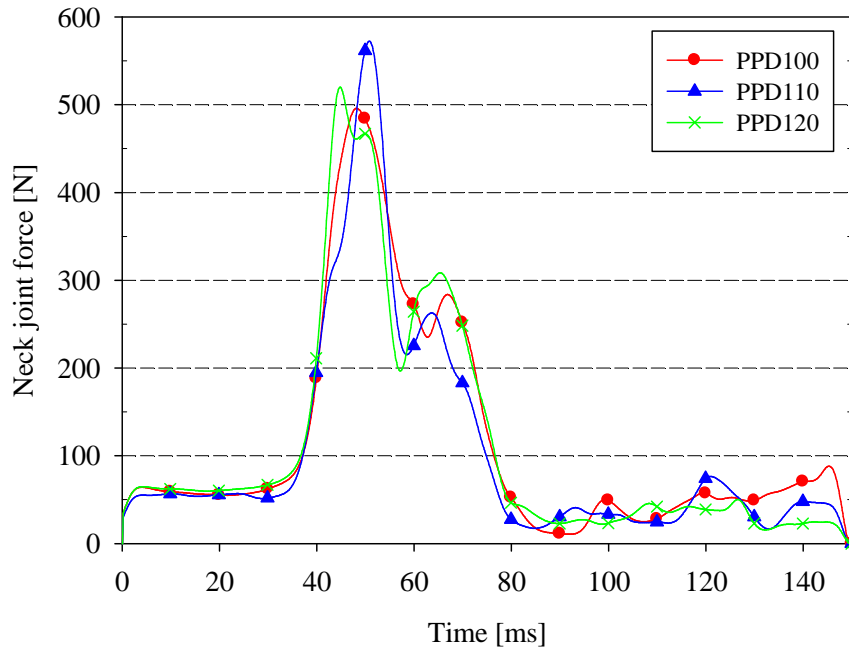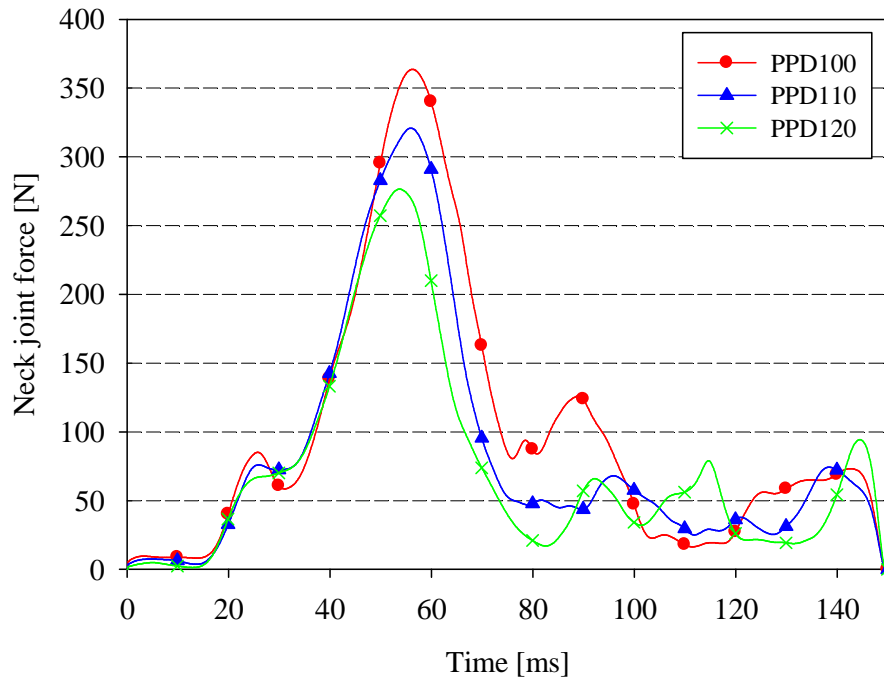**Figure 9-13.** Three PPD geometries middle neck joint forces as a function of time – frontal crash.
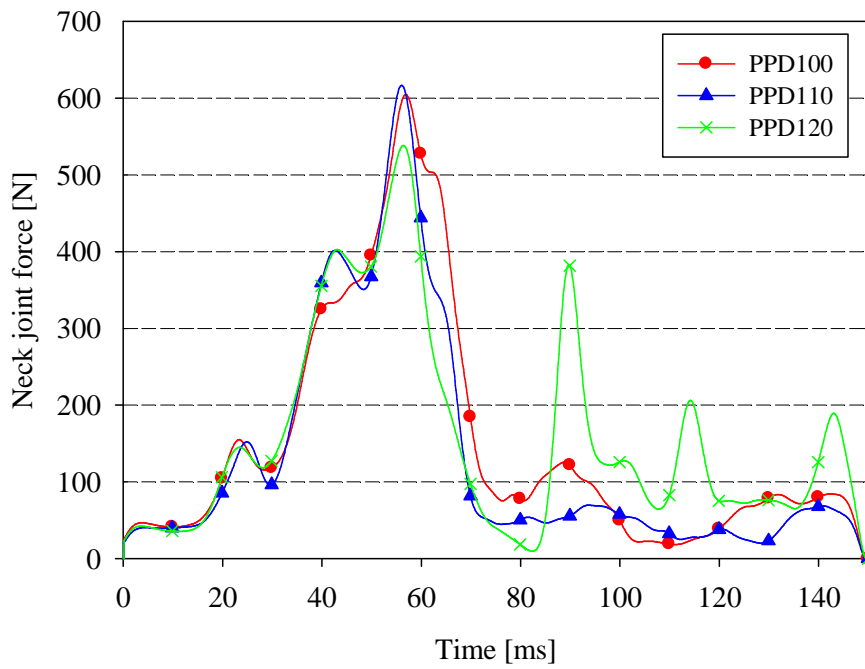
Figure 9-14. Three PPD geometries lower neck joint forces as a function of time – frontal crash.

9.4 Normal driving

Figure 9-15 presents the neck angles profiles as a function of time under the braking scenario. The neck angles were predicted to vary in a similar fashion for three PPD geometries except the initial neck angle difference. All three PPD geometries were able to assist infant dummies maintain in neck extension positions. The minimum neck angles occurred at the start with values of 103 degrees, 110 degrees, and 120 degrees for PPD100, PPD110, and PPD120, respectively. It should be reminded that the CRS was positioned in a rear-facing configuration, thus the braking load caused the infant dummy moved toward the CRS. Due to the inertia of the head under the braking load, the neck angles were continuously increasing up to maximum values. The final neck angles were predicted to be 120 degrees, 124 degrees, and 132 degrees for PPD100, PPD110, and PPD120, respectively.
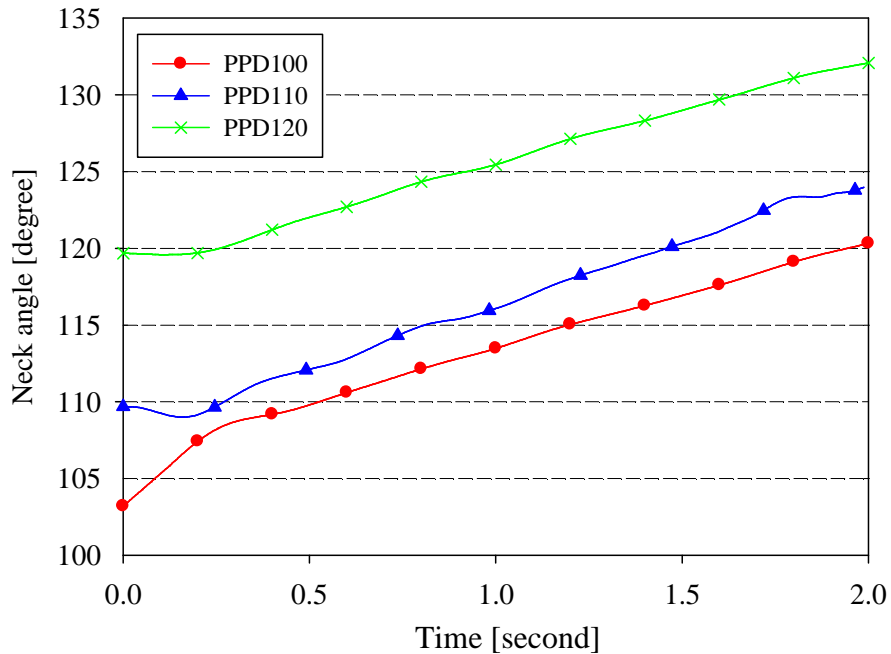
Figure 9-15. Three PPD geometries neck angles as a function of time – braking.

Figure 9-16 illustrates the neck angles as a function of time under the roundabout driving condition. Regardless of which PPD geometries was used, the infant dummy's neck angle was able to be maintained above 90 degrees, which secured a neck-extension position. The neck angle profiles for three PPD geometries exhibit very similar pattern and were offset by the initial neck angles. The neck angles were predicted to be 106 degrees, 108 degrees, and 117 degrees for PPD100, PPD110, and PPD120, respectively at the end of roundabout scenario.
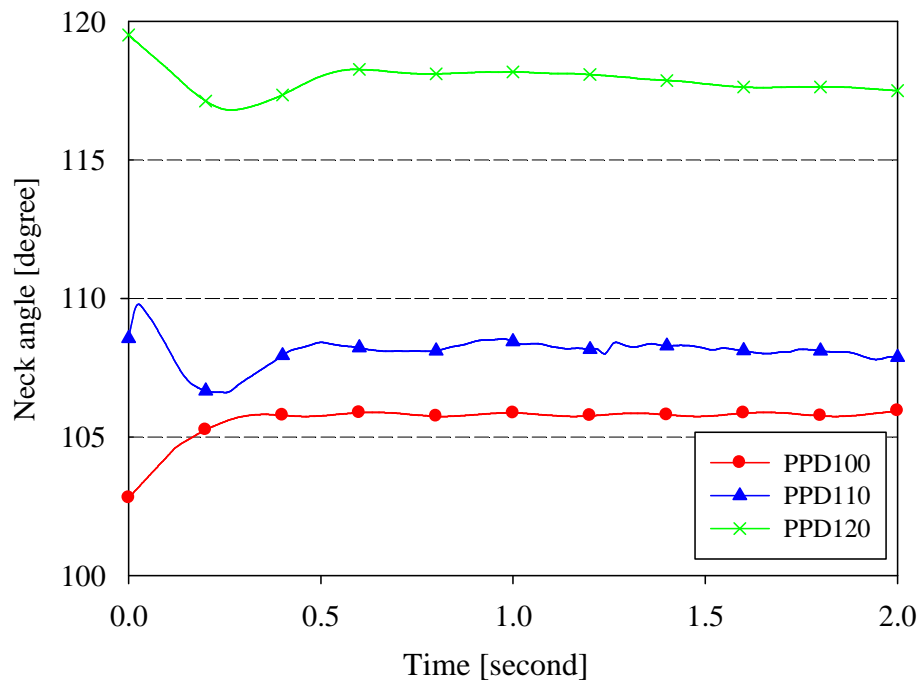
Figure 9-16. Three PPD geometries neck angles as a function of time – roundabout.

The neck angle profiles were presented in Figure 9-17 for three PDDs under the sharp-turn scenario. The acceleration prescribed to the CRS was able to cause neck-flexion. The neck angles dropped down to a value of approximately 85 degrees at the end of the sharp-turn for all three PPDs. Figure 9-18 illustrates the numerical observation of the simulations of three different PPD geometries.
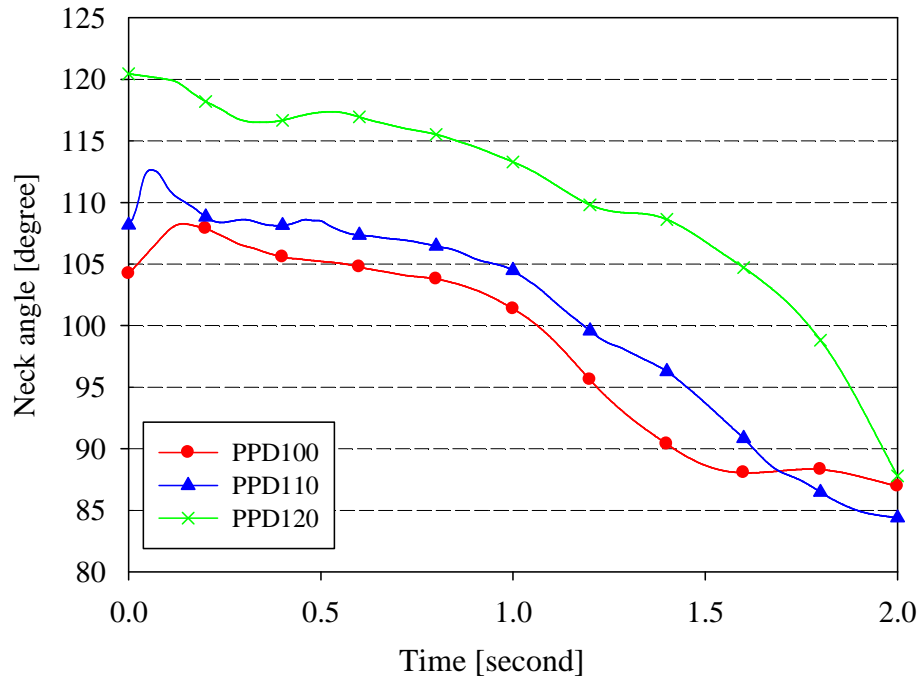
Figure 9-17. Three PPD geometries neck angles as a function of time – sharp-turn.

t = 0 ms

t = 55 ms

t = 80 ms

(a) (b) (c)
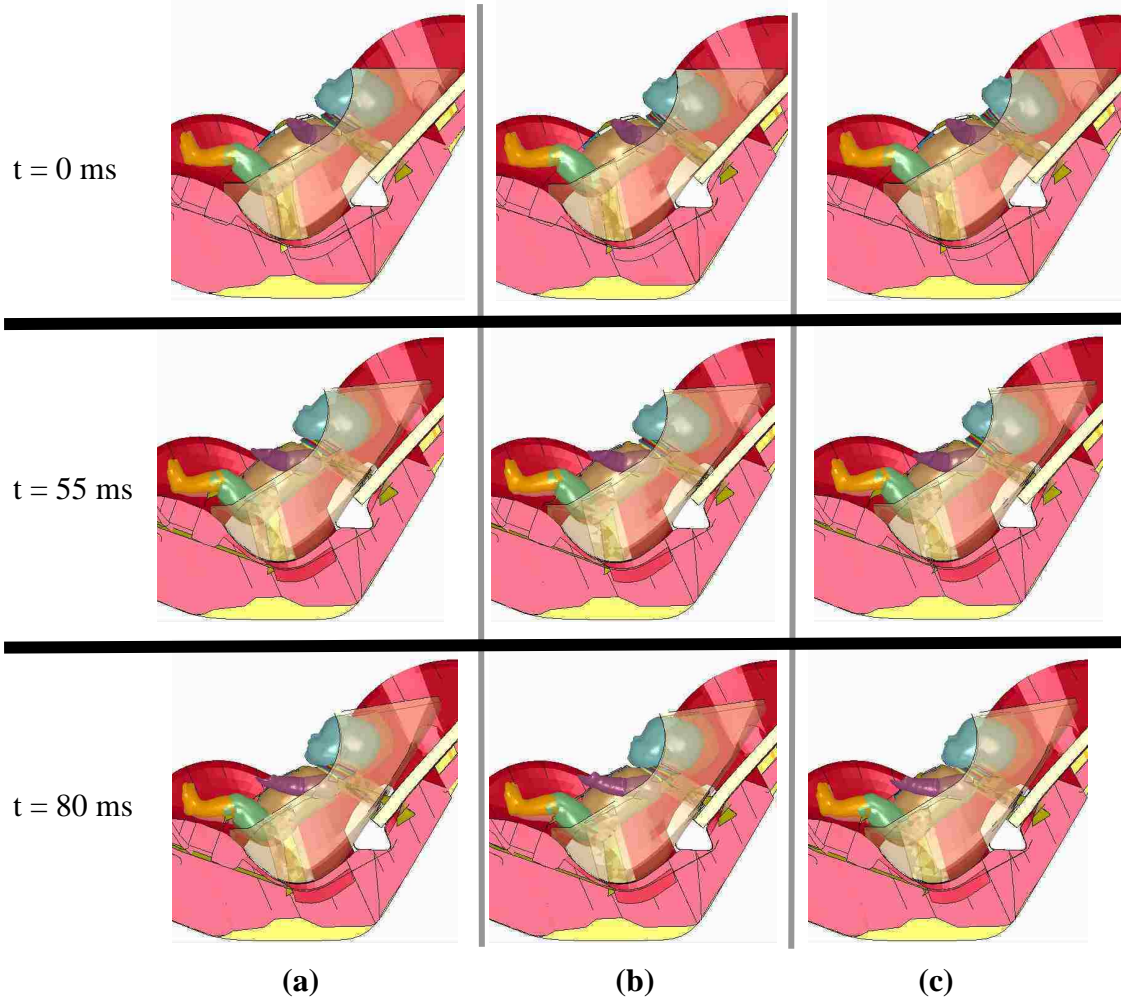
Figure 9-18. Numerical observation for PPD geometry study – sharp-turn:
(a) PPD100, (b) PPD110, and (c) PPD120.

10 The performance of the PPD in comparison with regular CRS

In this research, the incorporation of the PPD into a regular CRS as a method to reduce the risk of oxygen desaturation for low birth-weight infants when restrained in current car seat or infant seat was investigated. This chapter investigates the performance of the PPD and compares it with use of CRS only under aggressive conditions: side crash, frontal crash; and normal driving condition: braking, roundabout, and sharp-turn scenarios.

Tonkin et al. [24] reported in their study that the flexion of the head on body is a significant contributor to the episode of oxygen desaturation in preterm infants who are restrained in car seat seats. The report also indicated that the placement of a simple foam insert in a standard car seat that allow the infant to maintain the head in a neutral position on the trunk can substantially reduce the frequency of episodes of desaturation. However, it does not indicate that if the placement of a foam insert can reduce the safety protection from infant seat. Part of this research was dedicated to investigating the influence of the PPD on CRS safety performance while allow the low birth-weight infant to maintain the head in a neutral position on the trunk, which prevents the claps of airway. The effect of the PPD was assessed by analysis and comparing neck angles, head accelerations, and neck joint forces for both in the absence and presence of the PPD.

Figure 10-1 illustrates the low birth-weight infant dummy posture when restrained in the PPD and regular CRS only. It is apparent from the side view that the PPD maintained the dummy's head in a neck extension position whereas in the absence of the PPD it presented a tendency to flexion of the dummy's head. The neck angle of the dummy with the PPD was larger than the one without the PPD.

Based upon the results obtained from the material parametric study, described in chapter 6, chapter 7, and chapter 8, and the PPD geometry parametric study, described in chapter 9, the PPD110 with Foam#3 was utilized here to compare with regular CRS.

<div align="center">(a)   (b)</div>
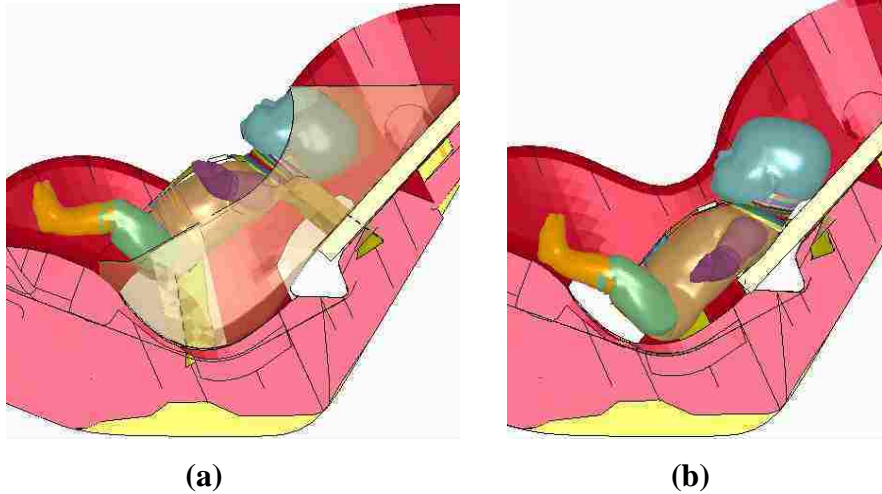
Figure 10-1. Side view of infant dummy (a) without PPD, (b) without PPD.

10.1 Side crash

Figure 10-2 illustrates the numerical observation in an event of side impact in the presence and absence of the PPD. When the infant dummy was restrained in the regular CRS without the assistance of the PPD, it was apparent that the neck-flexion position and the dummy's chine initially rest against on the CRS chest clasp. Greater head displacement was observed for the infant dummy without the PPD. Moreover longer duration of large head displacement was observed and the dummy's head was not back to the initial position, which was possible due to the weak neck mechanical properties. The PPD was able to lower the head displacement and bring dummy's head back into the initial position.

t = 0 ms

t = 50 ms

t = 80 ms

t = 150 ms

(a) **(b)**
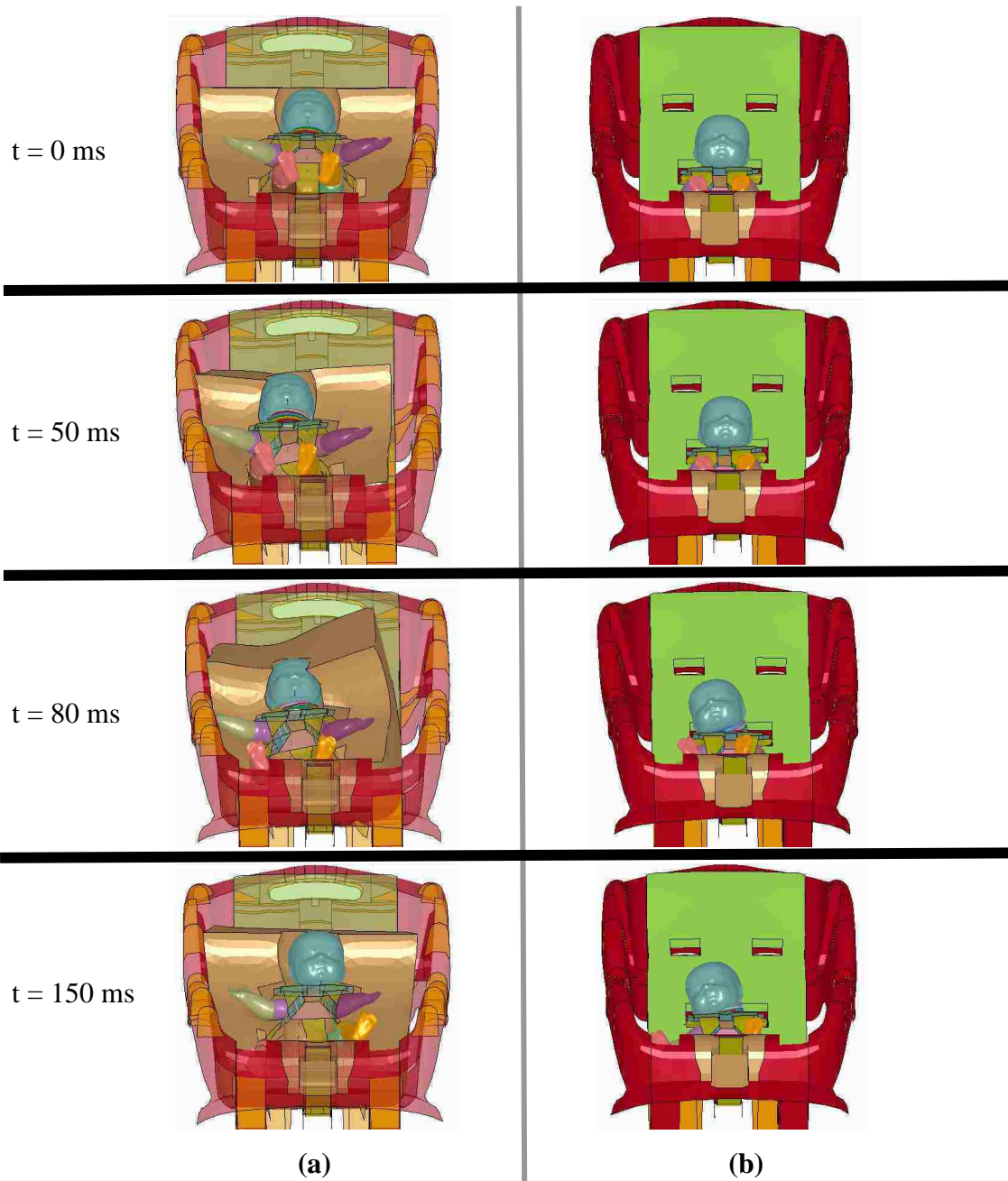
Figure 10-2. Numerical observation – side crash:

(a) with PPD, (b) without PPD.

10.1.1 Neck angle

Figure 10-3 illustrates the neck angles as a function of time under the side crash scenario both with and without the PPD. It should be noted that the initial neck angles without PPD and with PPD were 89 degrees and 110 degrees, respectively.
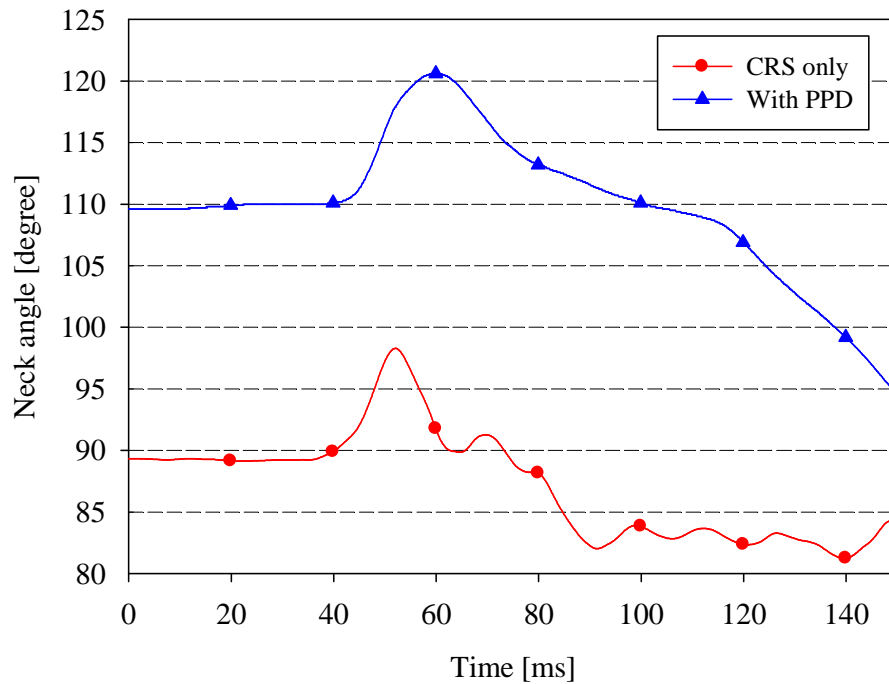
Figure 10-3. CRS with and without the PPD neck angles as a function of time – side crash.

The maximum neck angle of the infant dummy when restrained in PPD was predicted to be 120 degrees whereas 98 degrees was predicted without PPD. The neck angle for the infant dummy in CRS without PPD dropped to approximately 83 degrees and maintained in such a level, since no further flexion was permitted due to the limitation of the head and neck movements. Contact was observed between the dummy's chin and chest clasp. The neck angle of the dummy in PPD declined after t = 60 ms to a final value of 95 degrees as shown in Figure 10-3. It should be noted that the neck angle remained at approximately 83 degrees from t = 100 ms to t = 150 ms in the simulation of

the condition where the PPD was not utilized. This was believed due to the constraint of the rigid dummy model. The rigid dummy model head did not allow any deformation. With such a limitation, the predicted neck angle from the simulation was expected to be higher than the reality, since children's body segments are highly deformable. The real neck angle is expected to be smaller than what was predict in this model, which tends to increase the risk of airway collapse.

10.1.2 Head acceleration

Figure 10-4 illustrates the head accelerations as a function of time for the simulations of the conditions where CRS was used without and with the PPD under the side impact event. Same maximum head accelerations were predicted for both cases to be 60 g's. The maximum head acceleration of the dummy within PPD occurred slightly later, approximately 5 ms, than the one with the simulations of the conditions where CRS was used without the PPD. The presence of the PPD was believed to be the reason for the delayed response of the infant dummy. After t = 60 ms, the dummy's responses to the side impact acceleration were predicted to be in a totally different fashions. As shown in Figure 10-4, the head acceleration for the simulations of the conditions where CRS was used without the PPD maintains presents a high level of head acceleration whereas the acceleration for PPD case remains at a level below 10 g's most of the time. The lack of side support of the infant dummy's head and weak neck were blamed to be the causes of the high level of head acceleration. With the presence of the PPD, the infant dummy's head contacted with or was supported by the PPD when subjected to side impact acceleration pulse. The HIC_{36} profile as shown in Figure 10-5 also reflects the fact that the infant fumy sustained high acceleration for longer period of time. The maximum HIC_{36} values were predicted to be 300 and 170 for the simulations of the conditions where CRS was used without and with the PPD, respectively. The PPD was able to reduce the HIC_{36} value by approximately 43%.
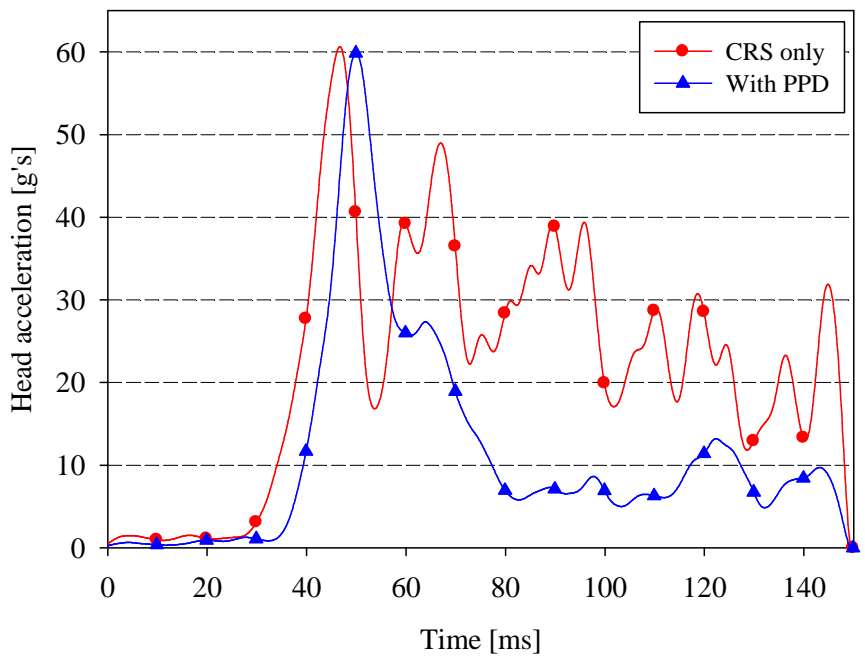
Figure 10-4. CRS with and without the PPD head accelerations as a function of time – side crash.
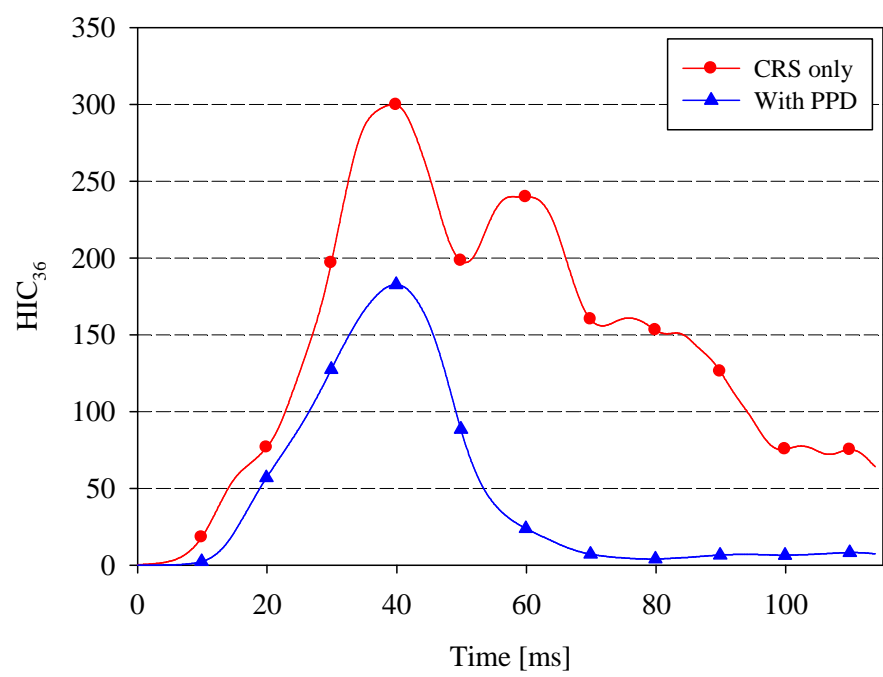
Figure 10-5. CRS with and without the PPD HIC$_{36}$ as a function of time – side crash.

10.1.3 Neck joint force

The upper, middle, and lower neck joint forces profiles as a function of time under the side impact scenario are presented in Figure 10-6, Figure 10-7, and Figure 10-8, respectively. With the presence of the PPD, for the upper neck joint forces, the maximum joint forces were predicted to be approximately 380 N and 375 N for the simulations of the conditions where CRS was used without and with the PPD, respectively. The occurrence of the peak value was delayed when PPD was present. It is apparent that when the infant dummy was placed in regular CRS without the PPD, the lower neck joint force remained at approximately 175 N between t = 80 ms and t =140 ms whereas with the presence of the PPD, the lower neck joint force was able to be controlled at significant lower level, approximately 30 N.
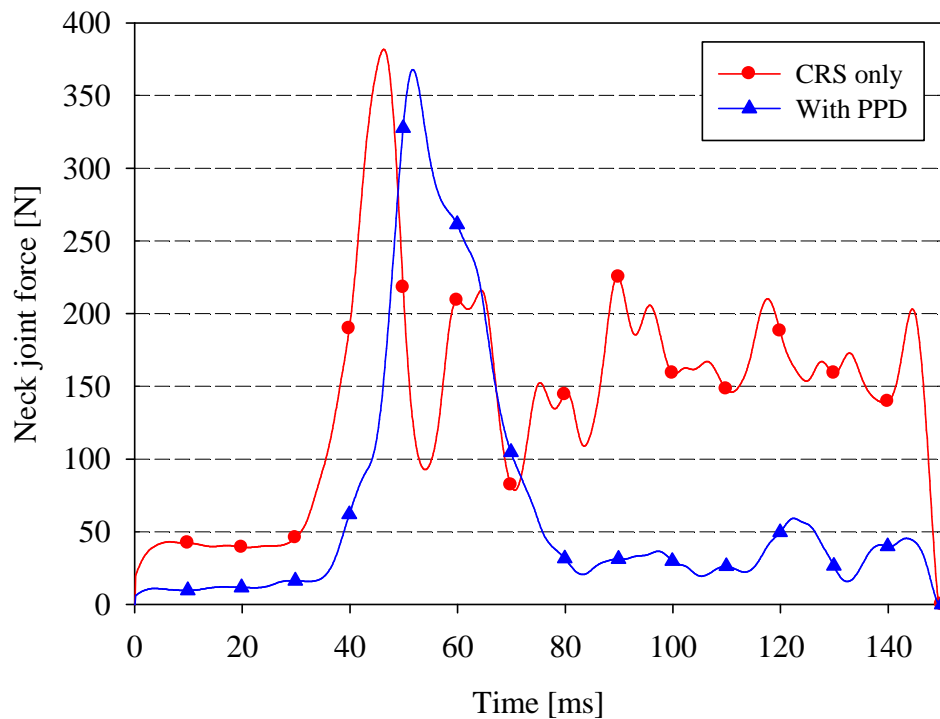
Figure 10-6. CRS with and without the PPD upper neck joint forces as a function of time – side crash.

Likely, the middle neck joint forces were predicted to have similar pattern as the upper neck joint forces. The maximum middle neck joint forces for both cases were predicted to be approximately 400 N. The peak value for the simulations of the conditions where CRS was used without the PPD occurred at t = 45 ms, approximately 10 ms earlier than the peak value with the presence of PPD. The PPD continuously reduced the middle neck joint force after the maximum value and was able to maintain it at approximately 40 N. The middle neck joint force was observed to remain at approximately 175 N after the occurrence of the peak value for the infant dummy when restrained in CRS without the PPD. The PPD was predicted to reduce the middle neck joint by 77 % after t = 80 ms.
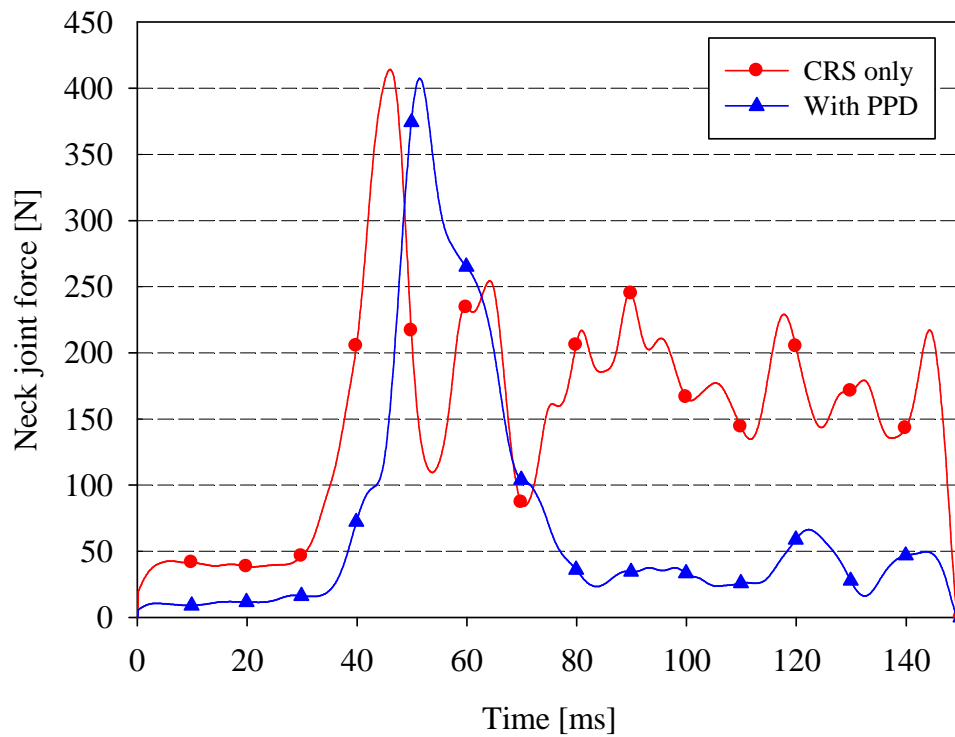
Figure 10-7. CRS with and without the PPD middle neck joint forces as a function of time – side crash.

Figure 10-8 illustrates the lower neck joint forces profiles as a function of time. The peak values were predicted to be 420 N and 570 N for the simulations of the conditions where CRS was present and absent, respectively. The PPD was predicted to increase the lower neck joint by approximately 35% compared with the condition where the PPD was not included. This was believed to be caused by the kinetic of the lower neck segment and torso. Based upon the results from previous simulations, the lower neck joint tended to exert a higher force compared to other neck joints. Like the upper and middle neck joint forces, the lower neck joint forces profiles for two cases was predicted to have very different patterns. Without the PPD, the neck joint forces remained at high load level, mostly above 200 N throughout the event, whereas the neck joint forces were able to be reduced significantly after the peak and maintain less than 100 N.

Figure 10-8. CRS with and without the PPD lower neck joint forces as a function of time – side crash.

10.2 Frontal crash

Figure 10-9 illustrates the side view of the numerical observations in an event of fontal impact in the presence and absence of the PPD. Overall, more head displacement for the dummy restrained in the PPD was observed due to introduction of the foam material between the infant dummy and the CRS. The maximum head displacements were observed at approximately t = 55 ms. Contact between chine and the CRS chest clasp was predicted at t = 95 ms for the dummy without the PPD when the head rebounded back from maximum extrusion.

t = 150 ms

(a)   (b)
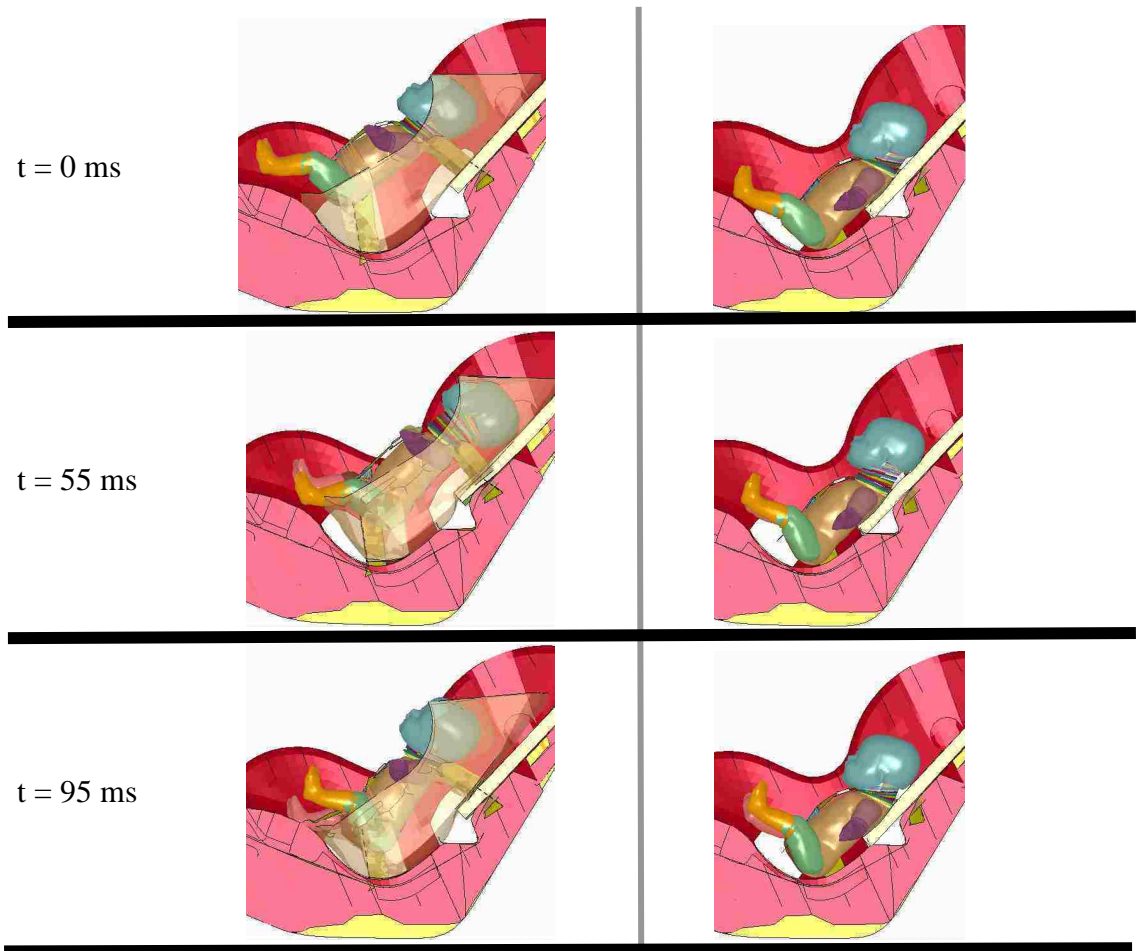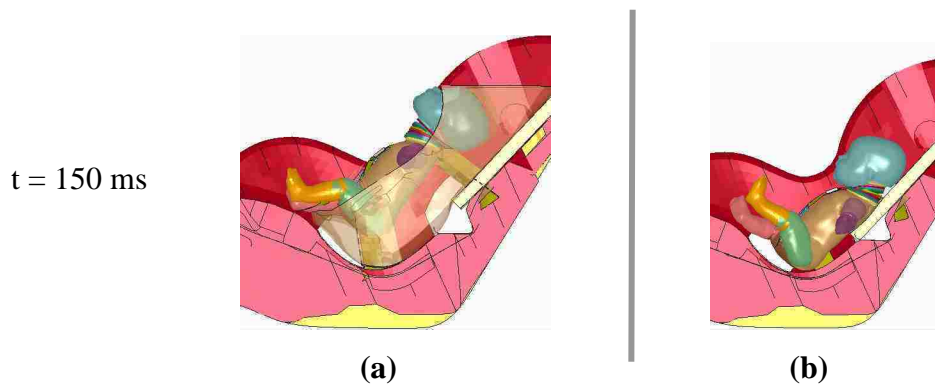
Figure 10-9. Numerical observation – frontal crash: (a) with PPD, (b) without PPD.

10.2.1 Neck angle

The infant dummy's neck angle profiles under the frontal impact condition as a function of time are illustrated in Figure 10-10. The utilization of the PPD resulted in a much larger neck angles cross the entire event than the case when only CRS was used to restrain infant dummy. More head rotation was predicted when the PPD was used since the presence of the PPD allowed dummy's head push into the when subjected to the frontal impact acceleration pulse, whereas motion of the infant dummy was limited in CRS without the PPD. The maximum neck angle for the simulations of the conditions where CRS was used without the PPD was predicted to be 97 degree at t = 60 ms while with the PPD two peaks of neck angle were predicted to occur at t = 60 ms and 150ms, with values of 142 degrees and 146 degrees, respectively. No significant neck angle change was predicted for the simulation of the condition where no PPD was utilized as a result of the rigid body dummy model. The rigid dummy model head did not allow any deformation. With such a limitation, the predicted neck angle from the simulation was expected to be higher than the reality, since children's body segments are highly deformable. The real neck angle is expected to be smaller than what was predicted in this model, which tends to increase the risk of airway collapse.
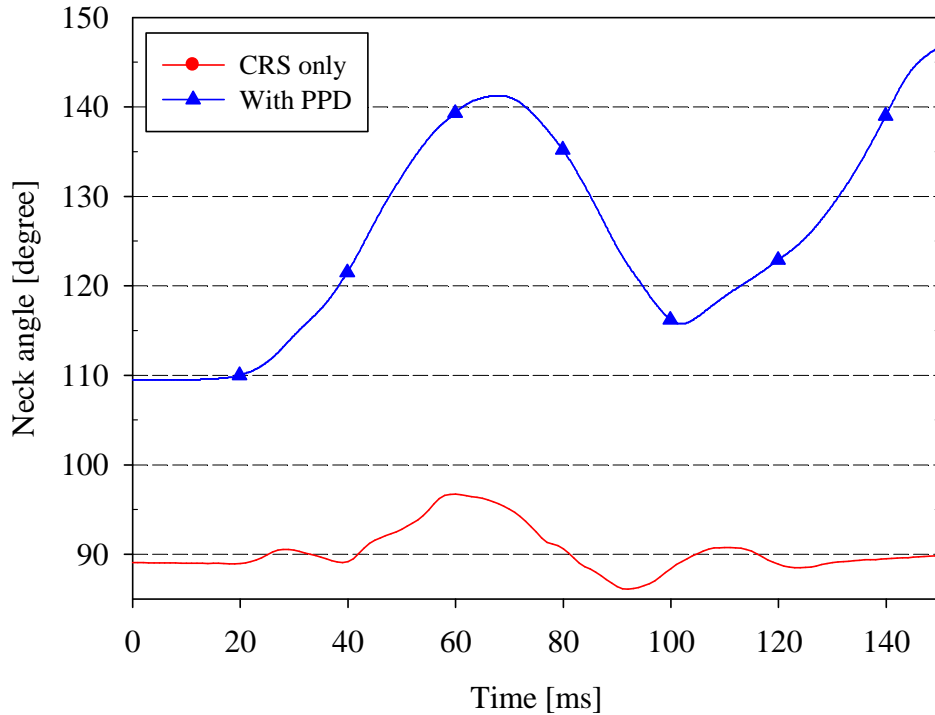
Figure 10-10. CRS with and without the PPD neck angles as a function of time – frontal crash.

10.2.2 Head acceleration

Figure 10-11 illustrates the head acceleration profiles as a function of time during the frontal impact simulations for both cases. The maximum head accelerations were predicted to be 70 g's and 85 g's for the simulations of the conditions where CRS was used without and with the PPD, respectively. Two profiles have very different patterns as shown. The head acceleration profile for the simulation of the condition where no PPD was used exhibits three significant peaks from t = 40 ms and t = 80 ms. Based upon the numerical observation shown in Figure 10-9, the first peak at t = 40 ms occurred when contact between the dummy's head and back foam pad of the CRS was observed. The maximum head displacement was observed at = 55 ms when second peak with value of 62 g's was predicted. After t = 58 ms, the infant dummy's head started to bounce back. The third peak head acceleration at t = 78 ms was resulted from the contact between the

chine and the CRS chest clasp. As shown in the numerical observations in Figure 10-9, contact was observed during the phase of head rebounding. With the presence of the PPD, higher maximum head acceleration was predicted. However, the PPD was able to decrease the head acceleration after the peak value occurrence and kept it remain at approximately 10 g's.   The HIC_{36} profiles were illustrated in Figure 10-12.   The maximum HIC_{36} was predicted to be 385 and 420 for the simulations of the conditions where CRS was used with and without the PPD, respectively.
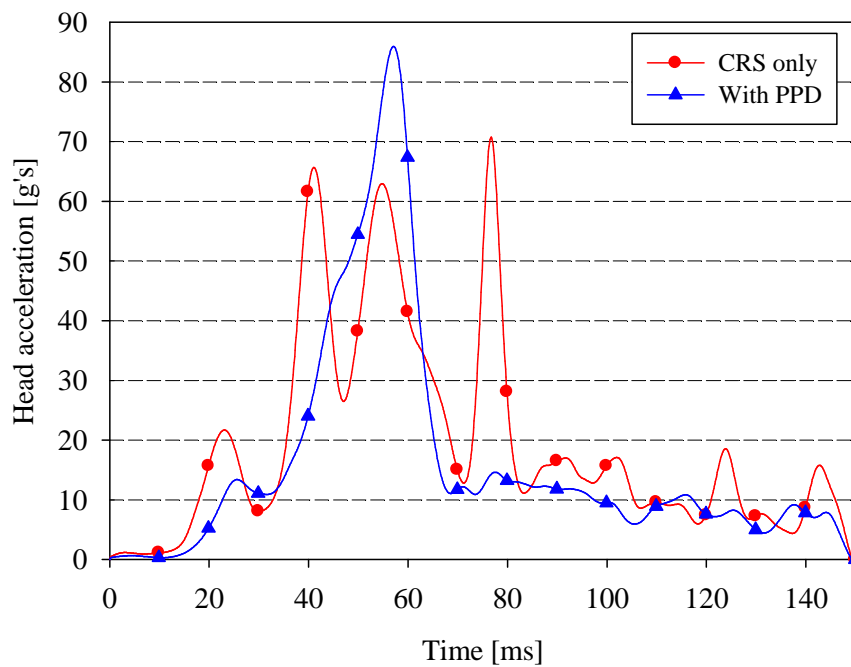
Figure 10-11. CRS with and without the PPD head accelerations as a function of time – frontal crash.
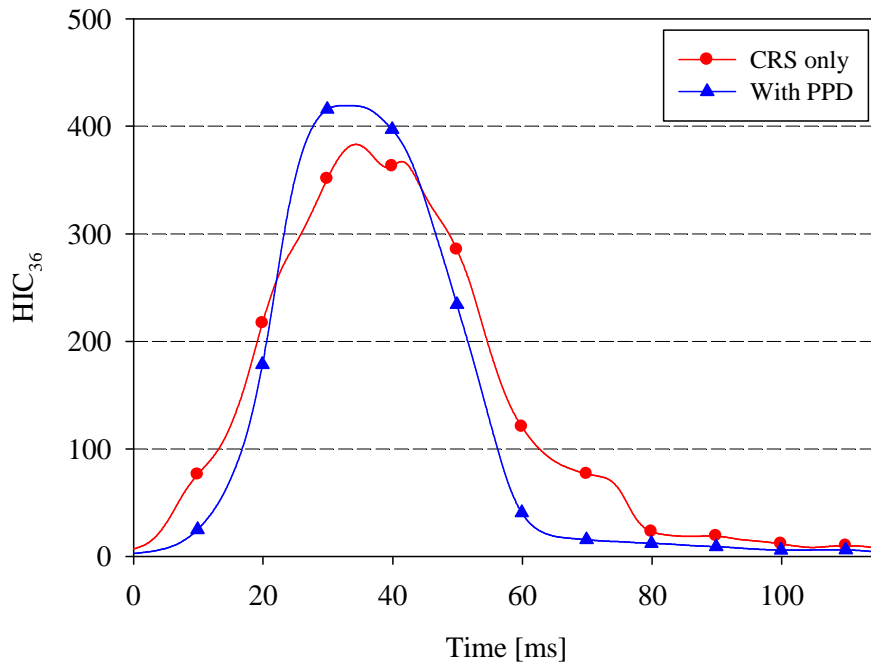
Figure 10-12. CRS with and without the PPD HIC_{36} as a function of time – frontal crash.

10.2.3 Neck joint force

Figure 10-13, Figure 10-14, and Figure 10-15 compares the upper, middle, and lower neck joint forces in the presence and absence of the PPD, when the infant dummy was subjected to the frontal impact acceleration. For the upper neck joint, a higher initial joint force (approximately 25 N) was predicted for simulations of the conditions where CRS was used without the PPD at $t = 0$ ms while the initial neck joint was approximately 5 N when the PPD was utilized. The neck-flexion position of the infant dummy when restrained in the CRS was assumed to be the cause of the higher neck joint forces, since the PPD was able to allow the infant dummy remain in a more neck neutral posture. The maximum upper neck joint force was predicted to be 250 N and 270 N for the simulations of the conditions where CRS was used without and with the PPD, respectively. Similar profiles were observed after the peak value occurrence.
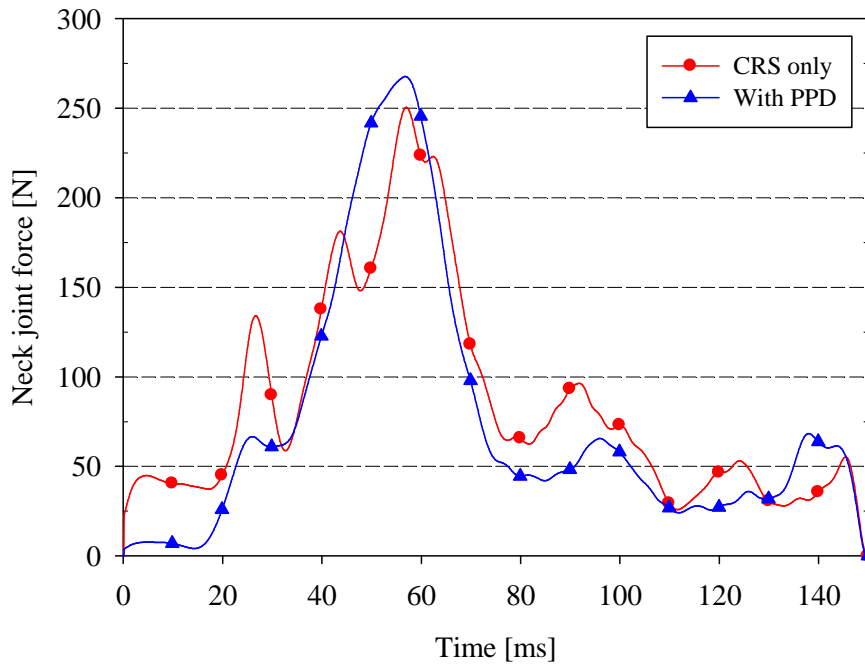
Figure 10-13. CRS with and without the PPD upper neck joint forces as a function of time – frontal crash.

Similar pattern was predicted for middle neck joint forces. The PPD resulted in a higher peak neck joint force of 320 N while in the absence of the PPD the peak force was predicted to be approximately 250 N. Again, this higher value was believed to be the introduction of more cushion room behind infant dummy when the PPD was utilized.
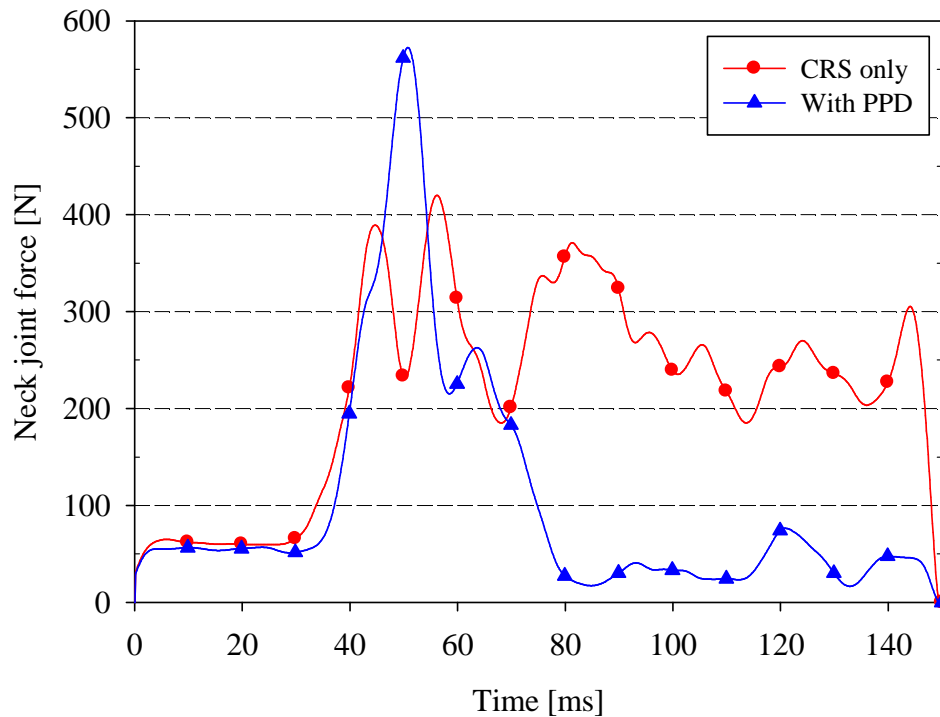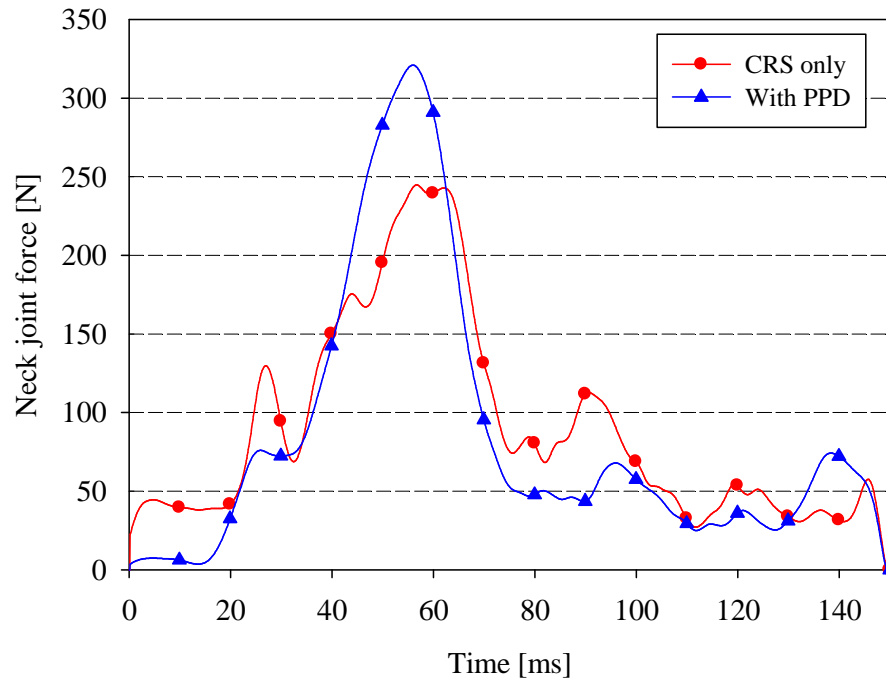
Figure 10-14. CRS with and without the PPD middle neck joint forces as a function of time – frontal crash.

Figure 10-15 illustrates the lower neck joint force profiles at the frontal impact condition as a function of time for the simulations of the conditions where CRS was used without and with the PPD. The maximum neck joint force was predicted to be approximately 260 N and 610 N for the simulations of the conditions where CRS was used without and with the PPD, respectively. Significant higher peak force and also longer duration of high force were observed in the presence of the PPD. More cushion material involved between the infant dummy and the CRS was the rational of this higher neck force. Moreover, the presence of the PPD resulted in more neck-extension. Therefore, when the infant dummy was subjected to the frontal crash, the infant dummy restrained in the PPD was more prone to head movement compared to the infant dummy restrained in the regular CRS directly, which in turn led to a higher neck joint force.
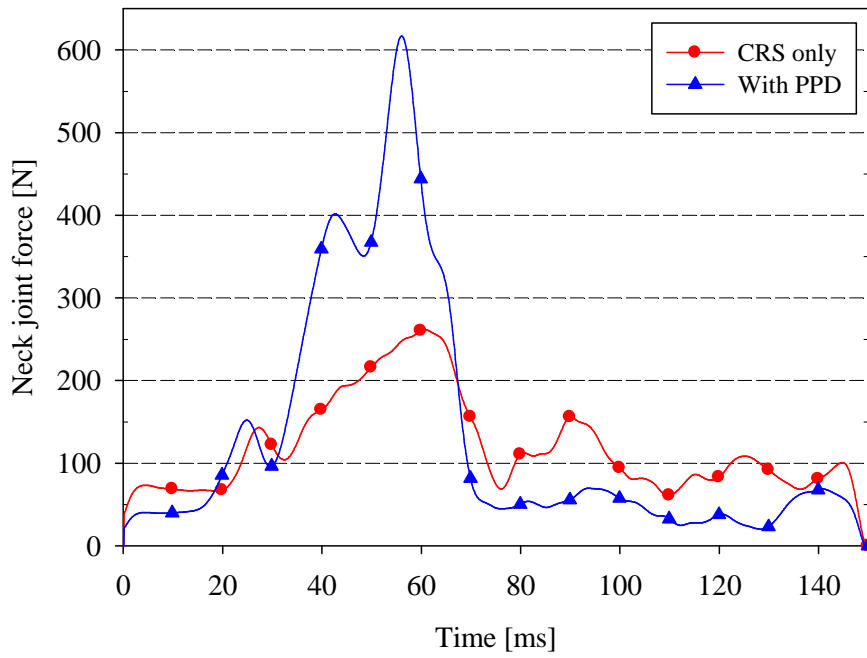
Figure 10-15. CRS with and without the PPD lower neck joint forces as a function of time – frontal crash.

10.3 Normal driving

Figure 10-16 compares the neck angles between the simulations of the conditions where CRS was used without and with the PPD in the braking scenario. The neck angle of the infant dummy who was constrained in the CRS without the PPD remained almost at a constant value of 87 degrees throughout the entire event. Due to the low braking acceleration and the support of the back foam pad, no significant movement or rotation were expected for dummy's head. With the presence of the PPD, the neck angle raised from initial value of 110 degrees up to 124 degrees. The soft foam material and large cushion zone at the back of the dummy's head allowed more movement and rotation of the head. It is apparent from the neck angle responses that the PPD was able to assist dummy with maintaining the neck-extension posture over the entire braking event, whereas the dummy constrained in the regular CRS stayed in a neck-flexion position throughout the duration of the event as a result of the rigid dummy model.
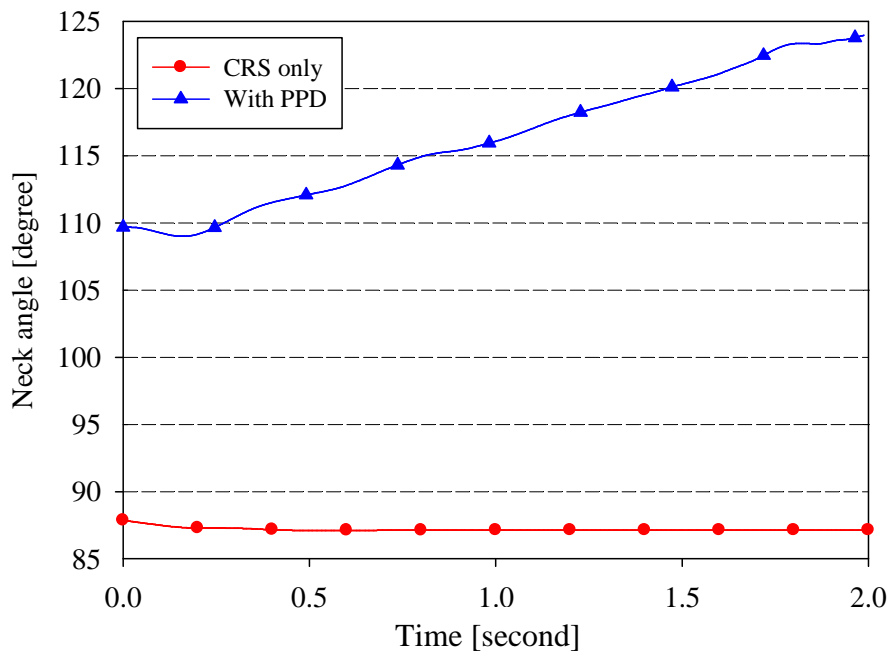
Figure 10-16. CRS with and without the PPD neck angles as a function of time – braking.

Figure 10-17 illustrates the neck angle profiles as a function of time for both restraint configurations during the roundabout driving condition. No significant changes in neck angle were predicted for both cases. Slight fluctuations with magnitude of 4 degrees were observed for the infant dummy in the PPD during first 0.5 second. Without the PPD the infant dummy's neck angle remained below 90 degrees, which is defined as neck-flexion configuration, while the PPD was able to assist infant dummy to stay in a neck-extension position at the roundabout driving condition. The PPD increased the neck angle by approximately 20 degrees.
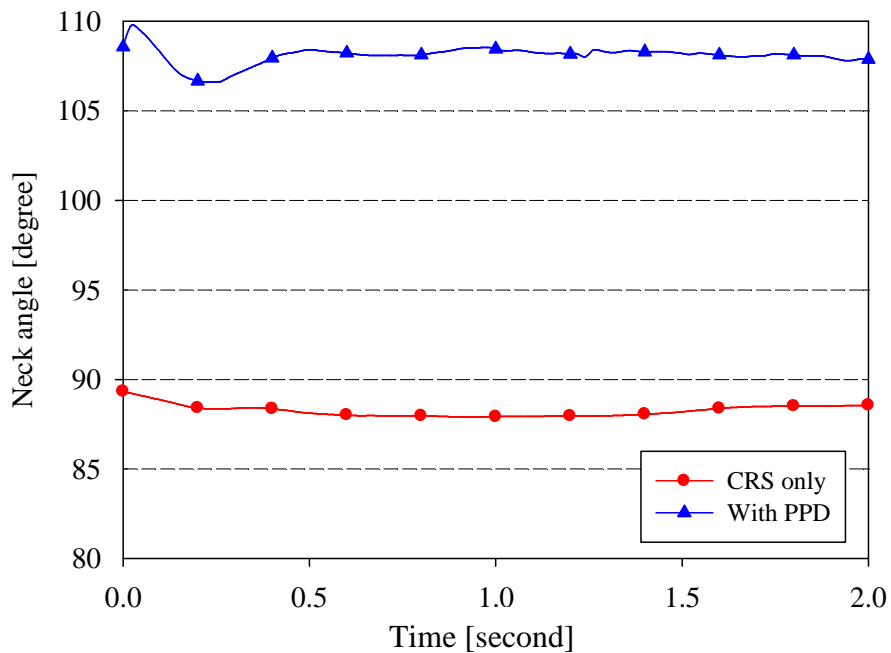
Figure 10-17. CRS with and without the PPD neck angles as a function of time – roundabout.

The neck angles under the sharp-turn driving condition were compared between the simulations of the conditions where the PPD was present and absent in Figure 10-18. The acceleration resulted in the dummy's head to flex toward chest regardless of the use of the PPD. In both cases, the neck angle was reduced to approximately 85 degrees, where the chine had contacted with the chest clasp and no further flexion would be possible. The PPD was managed to keep neck angle above 90 degrees for the first 1.6 second whereas without the PPD the neck angle stayed below 90 degrees throughout the entire event.
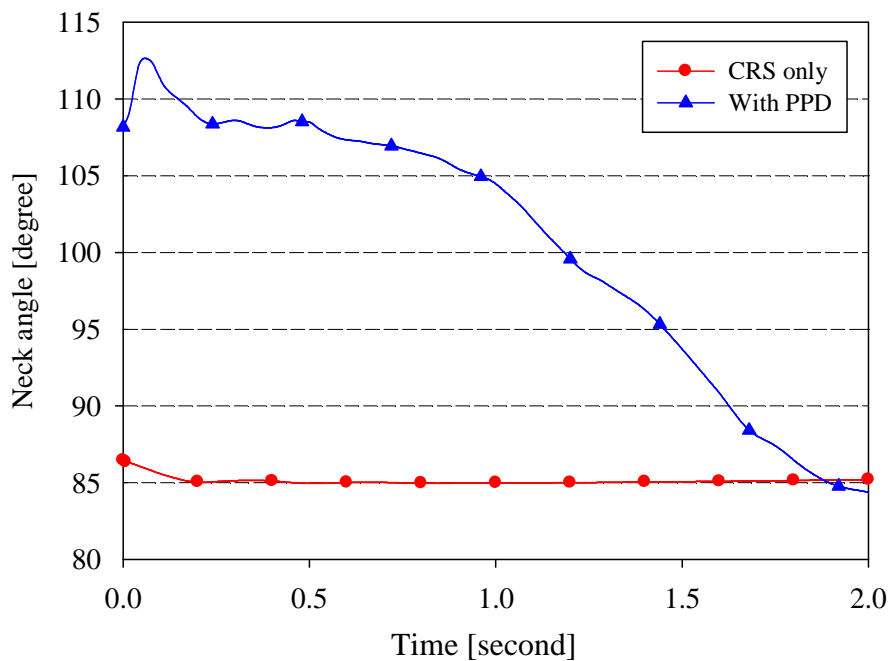
Figure 10-18. CRS with and without the PPD neck angles as a function of time – sharp-turn.

Overall, under the simulations of the normal driving conditions, the PPD was able to improve the neck angle significantly. The study by Wilson et al. [26] suggested that, neck flexion raised closing pressure, making the airway more susceptible to collapse, whereas neck extension lowered closing pressure, making the airway more resistant to collapse. Based upon this conclusion, the PPD was expected to decrease the risk of airway collapse, therefore, improve the infant's respiratory stability.

11. CONCLUSIONS AND FUTURE WORK

The preemie positioning device has been designed, developed, and investigated in a multi-disciplinary approach in collaboration with engineers, medical professionals, and industrial partner. Extensive numerical investigations have been completed incorporating a new developed low birth-weight dummy model. A foam material parametric study, PPD geometry parametric study, and comparison between the simulations of the condition where the PPD was utilized and the condition where the PPD was not present have been conducted. Based upon the quantitative and qualitative analysis of the numerical testing, the following conclusions can be stated:

11.1 Material parametric study

Three foam candidates were selected to implement into finite element model for various simulations. Five scenarios were simulated for this material parametric study. They were side impact, frontal impact, normal driving conditions including braking, roundabout, and sharp-turn. Analyses of the predication and observations acquired from numerical simulations indicated the following:

11.1.1 Material parametric study – side impact

i) The difference of the maximum neck angles for three foam candidates was less 5 degrees. Moreover, the neck angle profiles exhibited similar time history among three foam materials.

ii) No significant difference of the maximum head accelerations were predicted among the three foam candidates. A noticeable increase of the head acceleration when the foam A9_002 was utilized was observed over time from t = 100 ms to t = 130 ms. This was due to the contact between the dummy's head and the PPD. Similar HIC_{36} values were reported, varying between 175 and 200.

iii) The stiffest foam material A9_002 was able to reduce the peak neck joint force by approximately 22% compared to #12@500 mm/min. However, foam A9_002 resulted in a second contact when the dummy's head rebounded back and in turn caused the raising of the neck joint force at t = 110 ms. Foam A2@500 mm/min caused a moderate neck joint forces.

11.1.2 Material parametric study – frontal impact

i) Three foam candidates resulted in similar neck angles profiles. Foam A9_002, the stiffest foam among three, resulted in least peak neck angle, approximately 10 degrees less than other two foam candidates.

ii) The maximum head acceleration for foam A9_002 was 24 % and 18% less than foam #12@500 mm/min and A2_500@ mm/min, respectively. The stiffer foam illustrated a beneficial effect on the maximum head acceleration.

iii) The maximum neck joint forces were benefited from a stiffer foam material property. For both upper and middle neck joint forces, foam #12@500 mm/min and A2@500 mm/min were predicted to have 10% and 6% elevation respectively in maximum neck forces compared with foam A9_002. An increase of 50% and 65% in lower neck joint force was predicted for foam #12@500 mm/min and A2@500 mm/min, respectively.

iv) Significant increases of the neck joint forces were observed for foam A9_002 and A2@500 mm/min. The least stiff foam #12@500 mm/min was able to decrease the neck joint forces and keep the neck joint forces at low load level after the peak occurrence.

11.1.3 Material parametric study – normal driving condition

i)   During the braking scenario, all three foam candidates managed to assist the dummy with maintaining a neck-extension posture. Foam #12@500 mm/min, the least stiff foam among three, led to a final neck angle of 124 degree, which is 3 degrees and 10 degrees greater than foam A2@500 mm/min and A9_002, respectively. The less stiff foam material was predicted to be beneficial to the neck angle, which in turn decreases the infant's respiratory risks.

ii)   All three material candidates were able to keep infant dummy in neck-extension position. Similar final neck angles, varying between 106 degrees and 108 degrees were predicted for three foam candidates.

iii) No significant differences were observed for three candidates. Due to the direction of the acceleration pulse measured in the sharp-turn event, the neck angles dropped below 90 degrees after approximately t = 1.5 seconds regardless of which foam was utilized.

11.2 PPD geometry parametric study

Three different PPD configurations were generated to result in different neck angles when infant dummy was restrained. In order to study only the effect of various neck angles, the torso recline angle was kept same as the one investigated in the previous material parametric study. Three initial neck extension levels were investigated and they were 100 degrees, 110 degrees, and 120 degrees. Simulations were conducted on these three PPD configurations. The simulation events were side impact, frontal impact and normal driving conditions (braking, roundabout, and sharp-turn). Based upon finding from the simulations, the following conclusions can be stated:

11.2.1 Configuration parametric study – side impact

i)   Three PPD configurations resulted in similar neck angle in the side impact simulations.   The maximum values were 128 degrees, 120 degrees, and 116 degrees for PPD120, PPD110, and PPD110, respectively.   The final neck angles for three PPD configurations were predicted to be close to 96 degrees.

ii)   No significant differences were predicted for the resultant head accelerations. PPD120 reduced the peak acceleration by 5 g's compared with other two PPD configurations.   However, PPD120 exhibited longer duration of the high head acceleration, which was indicated by the higher HIC_{36} value.

iii)   In general, neck joint forces profiles present very similar results for three PPD configurations.   PPD110 led to maximum peak neck joint forces among three configurations, approximately 370 N, 400 N, and 560 N for upper, middle, and lower neck joints, repectively.

11.2.2 Configuration parametric study – frontal impact

i)   Maximum neck angles were predicted to occur at the end of the frontal impact simulations.   Both PPD100 and PPD110 were predicted to result in peak neck angles of approximately 145 degrees.   Peak value of the neck angle for PPD120 was predicted to be 160 degrees, which exceeds the limit of the extension level illustrated in Figure 2-5.

ii)   A reduction of 10 g's in the peak head acceleration was predicted for PPD120 compared to PPD100 and PPD110.   Both PPD100 and PPD110 resulted in similar peak head accelerations (approximately 85 g's).   A noticeable increase of head acceleration was observed for PPD100 at t = 80 ms.   PPD100 illustrated more fluctuations and greater head acceleration after the peak value occurrence.

iii) PPD120 resulted in least peak neck joint forces compared to PPD100 and PPD1120. However, significant increase and fluctuation of the lower neck joint forces were observed for PPD120 after t = 80 ms due to greater neck-extension level. Overall PPD110 exhibited very good dampening characteristics of the neck joint forces, which led to lower and stable neck joint force compared to other two configurations while had moderate peak neck joint force (approximately 270 N, 320 N, and 610 N for upper, middle, and lower neck joints, respectively).

11.2.3 Geometry study – normal driving condition

i) In braking and roundabout driving conditions, regardless of what type of PPD was utilized, the infant dummy was able to remain at neck-extension posture. Profiles in both conditions illustrated similar patterns among three PPD configurations, only differenced by the initial neck angles.

ii) In the sharp-turn simulation, the final neck angles were predicted to be approximately 87 degrees for three PPD configurations. In general, three PPDs were able to keep neck-extension posture for a considerable duration of the event.

11.3 Influence of PPD

The influence of the utilization of PPD100 incorporating foam #12@500 mm/min was investigated. The observations and results in the absence and presence of the PPD were compared under the same five testing conditions previous defined. The following conclusions can be stated:

11.3.1 Influence of PPD – side impact

i) For the infant dummy restrained in the PPD, an elevation of approximately 20% of the peak neck angle was predicted. The PPD was able to increase the neck angle by 20 degrees.

ii) Although the peak head accelerations were predicted to be 60 g's in both cases (with and without the PPD), significant high head acceleration level was predicted to remain over the simulation for the dummy restrained in regular CRS without the PPD due to a lack of side support and weak neck characteristics. The presence of the PPD reduced the after-peak head acceleration dramatically by approximately 68%. A reduction of 40% in the HIC_{36} was predicted for the use of the PPD.

iii) Similar peak values of the upper and middle neck joint forces were predicted for both cases. The addition of the PPD was predicted to have a reduction of 80% in the initial neck joint forces and be able to decrease and remain the after-peak neck joint forces at a relative low level (approximately 25% of the neck joint forces for the simulations of the conditions where CRS was used without the PPD).

iv) The addition of the PPD resulted in a greater lower neck joint force (approximately 150 N greater) due to the combination of movement in both torso and neck-head segment, which was not present in the simulations of the conditions where CRS was used without the PPD. However, without the PPD, the lower neck joint forces illustrated high level of force over the entire event while the presence of the PPD was able to decrease the neck joint force after the peak value and the forces generally were below 50 N.

11.3.2 Influence of PPD – frontal impact

i) A much greater neck angle was predicted when the PPD was utilized due to more head movement allowance introduced by the PPD. A peak value of 145 degrees was reported for the dummy in the PPD.

ii) An increase of 21% in peak head acceleration was predicted when the PPD was present. However, three head acceleration peaks were observed for the dummy

restrained in the simulations of the conditions where CRS was used without the PPD. The contact between chin and CRS chest clasp was observed, which was rational for the notably high head acceleration. A reduction of 20 in the HIC_{36} value was predicted for the simulation of the condition where the PPD was applied.

iii)   In general, the utilization of the PPD increased the neck joint forces due to more movements of the dummy's head. The placement of the PPD between the infant dummy and the CRS introduced more cushion zone in the vicinity of the dummy's head, which eventually led to more head extrusion.

11.3.3 Influence of PPD – normal driving condition

i)   The addition of the PPD was predicted to be beneficial in keeping infant dummy's neck-extension level in all normal driving conditions investigated here. For both braking and roundabout events, the final neck angles were predicted to remain at approximately 124 degrees and 107 degrees, respectively. Without the utilization of the PPD, the neck angle generally stayed below 90 degrees, i.e. neck-flexion posture, which is more prone to airway compromise.

ii)   In the sharp-turn driving condition, due to the acceleration direction which tended to flex the dummy's head, even with the presence of the PPD, the neck angle fell below 90 degrees at approximately t = 1.5 seconds. The PPD still was beneficial to the neck posture most of the time in term of airway compromise risk.

11.4 Future work

Future work for this research includes an investigation in a utilization of a multi-density foam. The PPD with different mechanical properties depending on the loading direction can be achieved by utilizing a multi-density foam. For example, stiffer foam can be applied in the vicinity of the back of an infant's head to dissipate impact energy more efficiently. Moreover, further research is needed to model a strain-rate-dependent foam material. Ideally, soft foam property is favorite during normal daily driving condition for the reason of providing comfort and stiffer foam can be rewarding during an aggressive disturbance, such as an event of crash. The strain-rate dependent foam can potentially serve and result in good results under both conditions.

At present, the PPD configuration parametric study has been only considering varying the neck angle of the dummy. Further research is needed to investigate or optimize both torso angle and neck angle. An experiment of design can be performed to investigate more thoroughly the influence of the torso angle, neck angle, and materials to achieve an optimized combination.

Further study is needed to improve the infant dummy model. With more biomechanical data available in the future, the important joint properties, like neck joint property, can be modified with updated data. The overall neck segments kinematics can be modified and improved accordingly. Additionally, utilization of deformation body segments instead of rigid part can further improve the capability of the infant dummy model and provide better results of investigating the risk of infants' airway collapse.

Appendix A

Material foam Mathcad script (provided by Dr. W. Altenhof from University of Windsor)

$A \equiv \text{READPRN}(\text{"test\_HR\_A2.txt"})$ $\qquad\qquad$ $B \equiv \text{READPRN}(\text{"r14"})$

$Disp12 := \left(A^{\langle 1 \rangle}\right) \cdot mm$ $\qquad\qquad$ $Disp_{sim} := \left(B^{\langle 1 \rangle} - 3\right) \cdot mm$

$F12 := A^{\langle 2 \rangle} \cdot N$ $\qquad\qquad$ $F_{sim} := B^{\langle 2 \rangle} \cdot \dfrac{kg \cdot mm}{s^2}$

$L12 := 380mm$ $\qquad$ $W12 := 380mm$ $\qquad$ $H12 := 100 \cdot mm$ $\qquad$ $mass := 544.1gm$

$Area12 := L12 \cdot W12$

$Density := \dfrac{mass}{Area12 \cdot H12}$ $\qquad$ $Density = 3.768 \times 10^{-8} \cdot \dfrac{kg}{mm^3}$

$Stress12 := \dfrac{F12}{Area12}$ $\qquad$ $Strain12 := \dfrac{Disp12}{H12}$

$Stress_{sim} := \dfrac{F_{sim}}{Area12}$ $\qquad$ $Strain_{sim} := \dfrac{Disp_{sim}}{H12}$

Force versus Displacement

$P_1 := 100$ $\qquad$ $P_2 := 250$

134
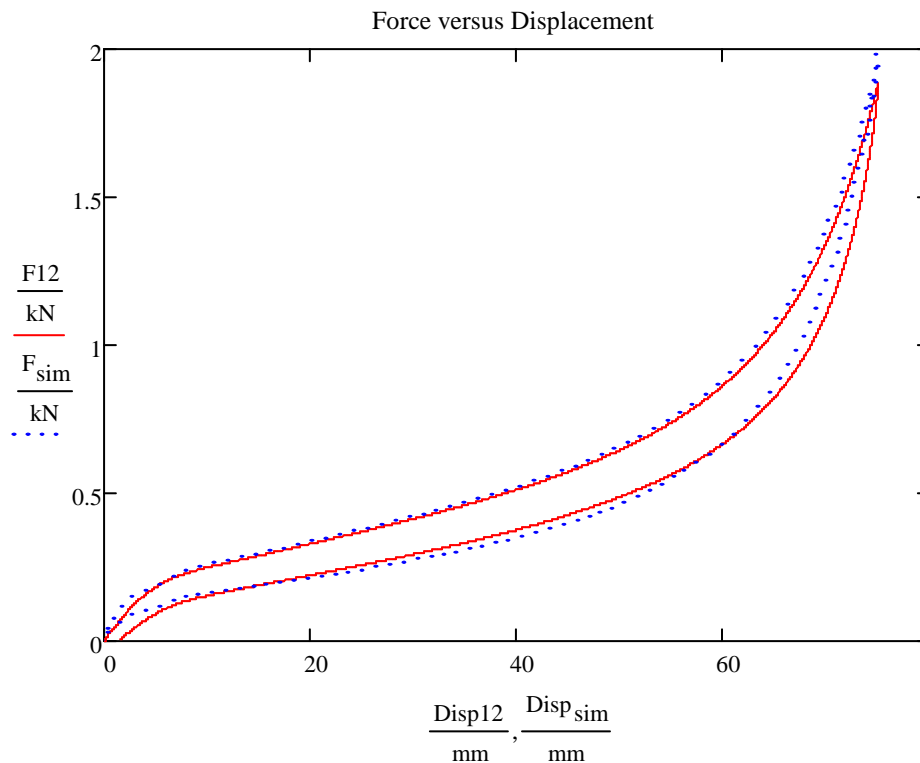
$$\text{ORIGIN} \equiv 1 \qquad \text{kN} \equiv 1 \cdot 10^3 \cdot \text{N} \qquad \text{MPa} \equiv 1 \cdot 10^6 \cdot \text{Pa} \qquad \text{offset}(D, F, Fc) \equiv \begin{vmatrix} j \leftarrow \text{rows}(F) \\ n \leftarrow 1 \\ \text{while } F_n < Fc \\ \quad n \leftarrow n + 1 \\ D_n \end{vmatrix}$$

$$\text{kPa} \equiv 1 \cdot 10^3 \cdot \text{Pa}$$

$$\text{INT}(D, F) \equiv \begin{vmatrix} j \leftarrow \text{rows}(D) - 1 \\ \text{for } i \in 1..j \\ \quad \begin{vmatrix} E_i \leftarrow 0 \cdot J \text{ if } i = 1 \\ E_i \leftarrow E_{i-1} + (F_i) \cdot \left(\dfrac{D_{i+1} - D_{i-1}}{2} \right) \text{ if } i \neq 1 \wedge i \neq j \\ E_i \leftarrow E_{i-1} \text{ otherwise} \end{vmatrix} \\ E \end{vmatrix}$$

Engineering Stress vs. Strain
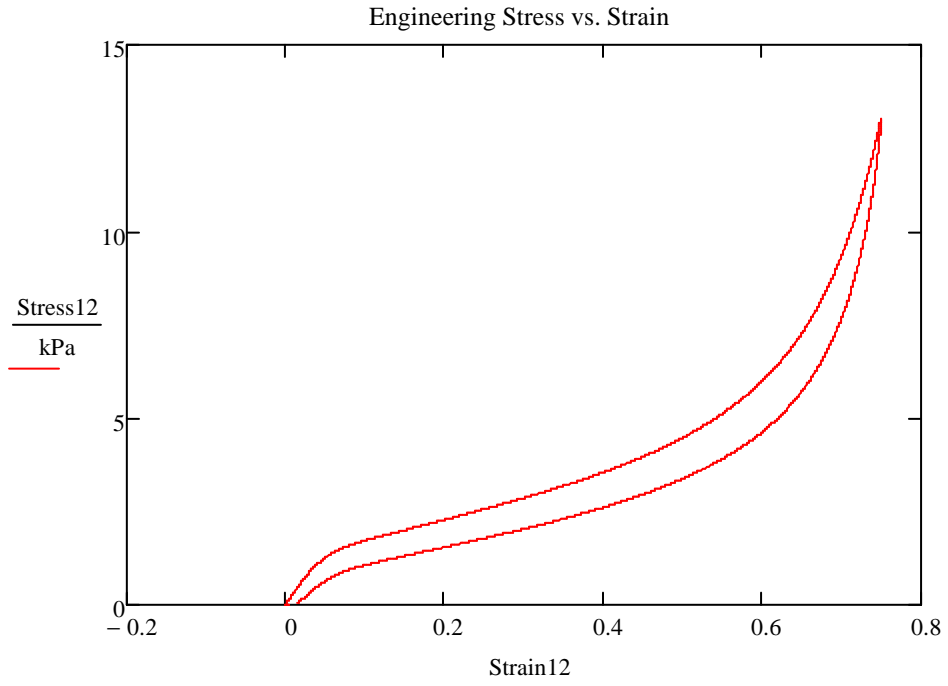
$$\text{strain}_{\text{interval}} := \frac{\text{max}_{\text{strain}}}{\text{n}_{\text{points}} - 1}$$

$$\text{e4}_j := (j - 1) \cdot \text{strain}_{\text{interval}}$$

$$\text{S4}_j := \text{fit}\left(\text{e4}_j\right)$$

Engineering Stress vs. Strain

$$\frac{\text{Stress12}}{\text{kPa}}$$

$$\frac{\text{Stress12}_{P_{\text{end}}}}{\text{kPa}}$$

✖·✖

$$\frac{\text{Stress12}_{P_1}}{\text{kPa}}$$

+ +

$$\frac{\text{Stress12}_{P_2}}{\text{kPa}}$$

⊟-⊟

$$\frac{\text{S2}}{\text{kPa}}$$

● ●

$$\frac{\text{fit}(\text{e3})}{\text{kPa}}$$

- - - -

$$P_3 := 800$$

$$P_4 := 1500$$

$$P_{\text{end}} := 4680$$

$$i := 1, 2 .. 16$$

$$\text{Strain12}, \text{Strain12}_{P_{\text{end}}}, \text{Strain12}_{P_1}, \text{Strain12}_{P_2}, \text{e2}, \text{e3}$$
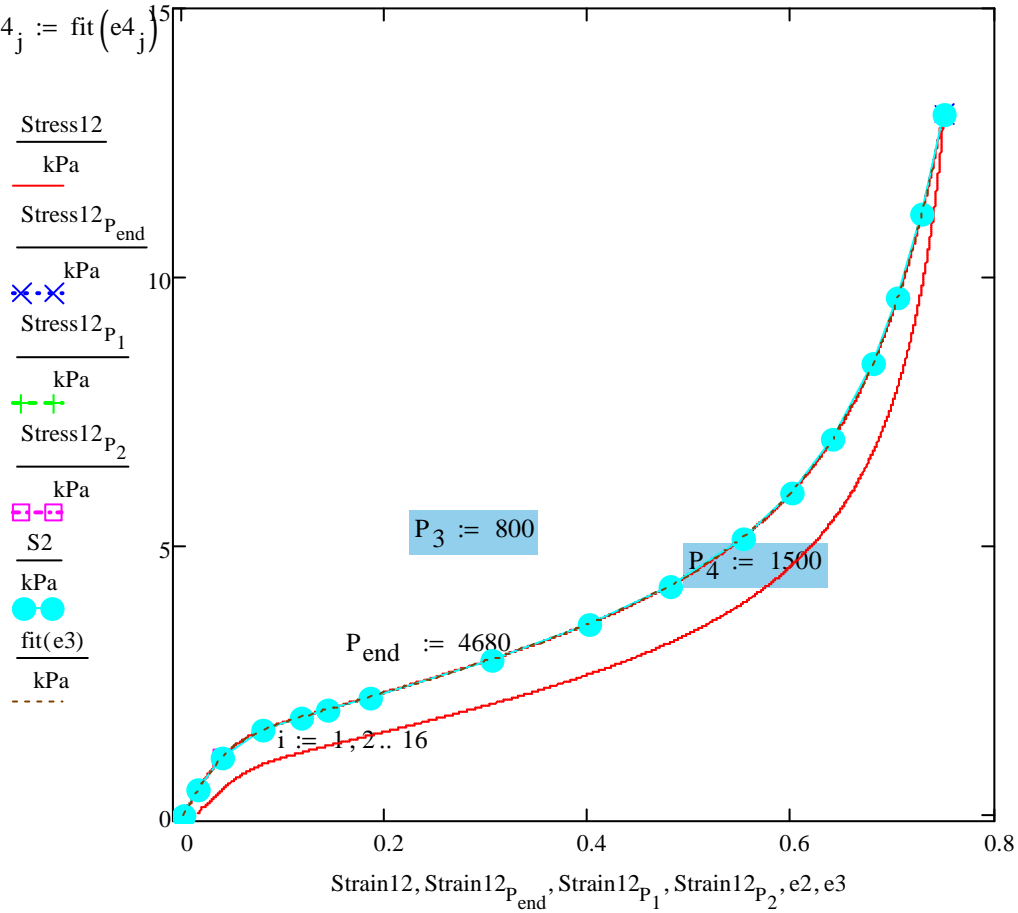
$$\text{e2}_1 := 0.0 \qquad \text{e2}_{i+1} := \text{Strain12}_{k_i} \qquad\qquad \text{S2}_1 := 0.0 \cdot \text{kPa}$$

$$\text{S} := \text{cspline}\left(\text{e2}, \frac{\text{S2}}{\text{kPa}}\right) \qquad\qquad \text{S2}_{i+1} := \text{Stress12}_{k_i}$$

$$\text{fit}(x) := \text{interp}\left(\text{S}, \text{e2}, \frac{\text{S2}}{\text{kPa}}, x\right) \cdot \text{kPa}$$

$$\text{e3} := 0, 0.01 .. \max(\text{Strain12})$$

$$\text{n}_{\text{points}} := 30 \qquad j := 1, 2 .. \text{n}_{\text{points}}$$

$$\text{max}_{\text{strain}} := \frac{\text{ceil}((\max(\text{Strain12} \cdot 100)))}{100} \qquad \text{max}_{\text{strain}} = 0.75 \qquad \text{max}_{\text{strain}} := 0.80$$

136

DATA OUTPUT TO FILE "stress_strain_data.txt" FOR MATERIAL MODEL #57 (LOW_DENSITY_FOAM) MATERIAL MODEL

$$\text{augment}\left(e4\,,\dfrac{S4}{\dfrac{kg}{mm\cdot s^2}}\right) =$$

	1	2
1	0	0
2	0.02758621	0.81129371
3	0.05517241	1.33987907
4	0.08275862	1.61120416
5	0.11034483	1.7832477
6	0.13793103	1.935079
7	0.16551724	2.08629272
8	0.19310345	2.23834313
9	0.22068966	2.3931595
10	0.24827586	2.55174205
11	0.27586207	2.71501826
12	0.30344828	2.88391561
13	0.33103448	3.0596985
14	0.35862069	3.24498938
15	0.3862069	3.44275291
16	0.4137931	...

$$\text{WRITEPRN (\text{"HR\_A2\_stress\_strain\_data.txt"}} \quad) := \text{augment}\left(e4\,,\dfrac{S4}{\dfrac{kg}{mm\cdot s^2}}\right)$$

Engineering Stress vs. Strain
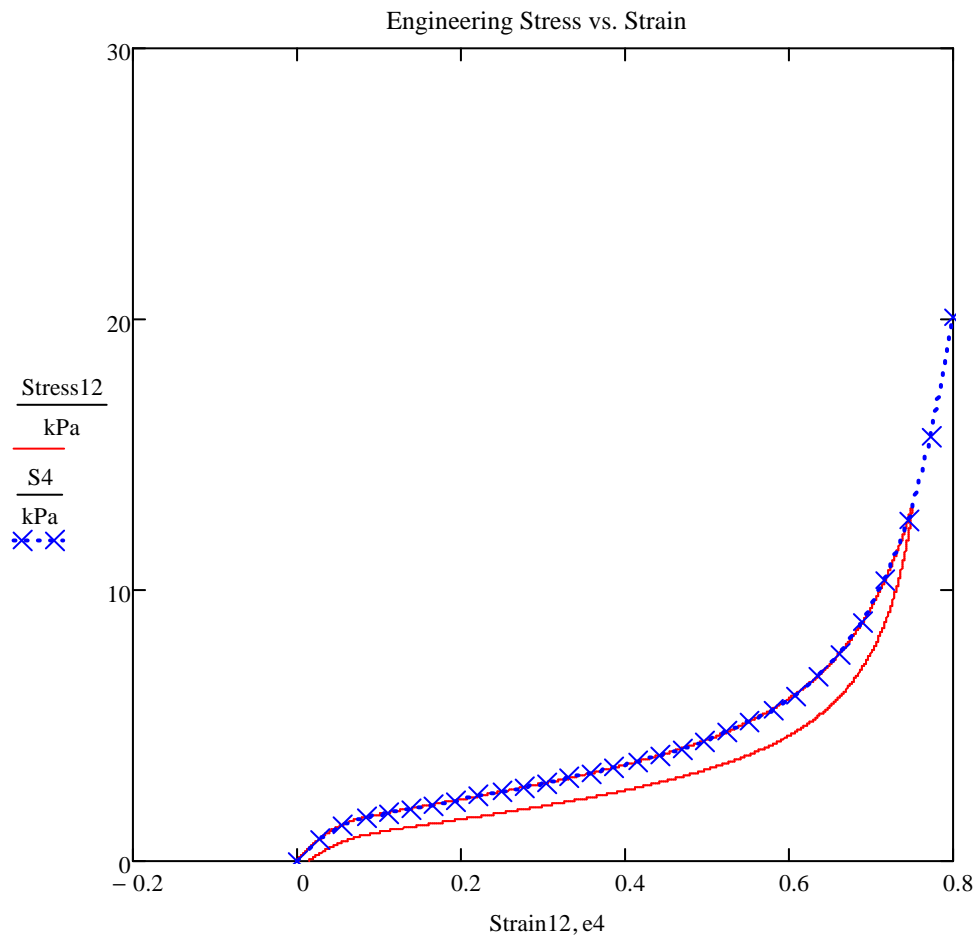
Appendix B

In-vehicle on-road experiments data analysis

	Validation metrics - velocity		
	Braking	Roundabout	Sharp turn
X	0.987	N/A	0.923
Y	N/A	0.977	0.986
Z	0.979	N/A	0.906

(a)

	Validation metrics – Displacement		
	Braking	Roundabout	Sharp turn
X	0.991	N/A	0.901
Y	N/A	0.861	0.991
Z	0.985	N/A	0.927

(b)

Table B-1. (a) Velocity (b) displacement validation metrics.

Figure B-1. The acceleration pulse input curve in y-direction for roundabout event.

(a)

(b)
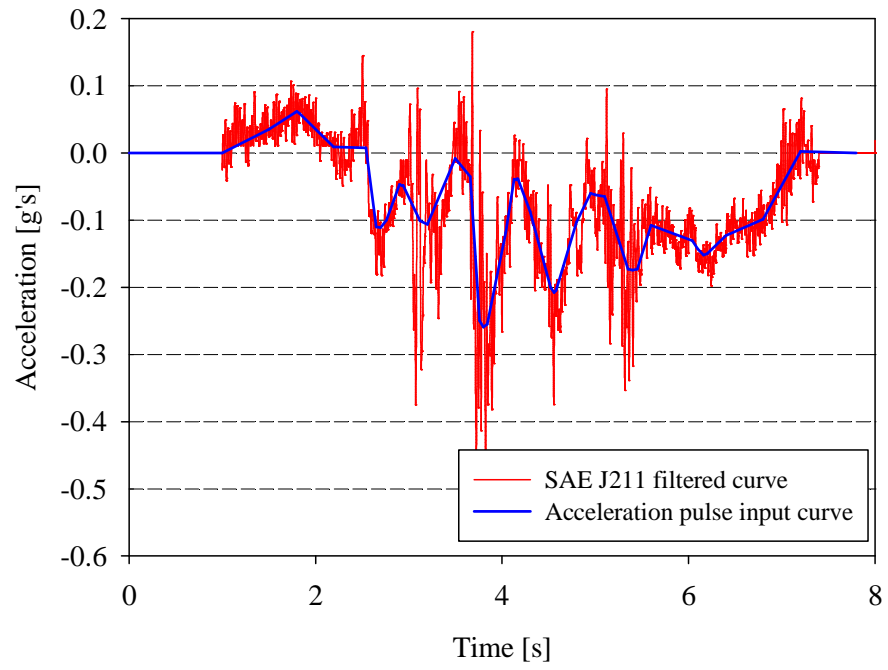
Figure B-2. The acceleration pulse input curve in (a) x direction (b) y-direction (c) z-direction, for sharp turn event.

Infant dummy neck angle calculation Mathcad script

Neck angle

$\text{ORIGIN} \equiv 1$

$\text{P1x} \equiv \text{READPRN(} \text{ "p1x.txt"} \quad)$

$\text{P2x} \equiv \text{READPRN(} \text{ "p2x.txt"} \quad)$

$\text{P3x} \equiv \text{READPRN(} \text{ "p3x.txt"} \quad)$

$\text{P1y} \equiv \text{READPRN(} \text{ "p1y.txt"} \quad)$

$\text{P2y} \equiv \text{READPRN(} \text{ "p2y.txt"} \quad)$

$\text{P3y} \equiv \text{READPRN(} \text{ "p3y.txt"} \quad)$

$\text{P1z} \equiv \text{READPRN(} \text{ "p1z.txt"} \quad)$

$\text{P2z} \equiv \text{READPRN(} \text{ "p2z.txt"} \quad)$

$\text{P3z} \equiv \text{READPRN(} \text{ "p3z.txt"} \quad)$
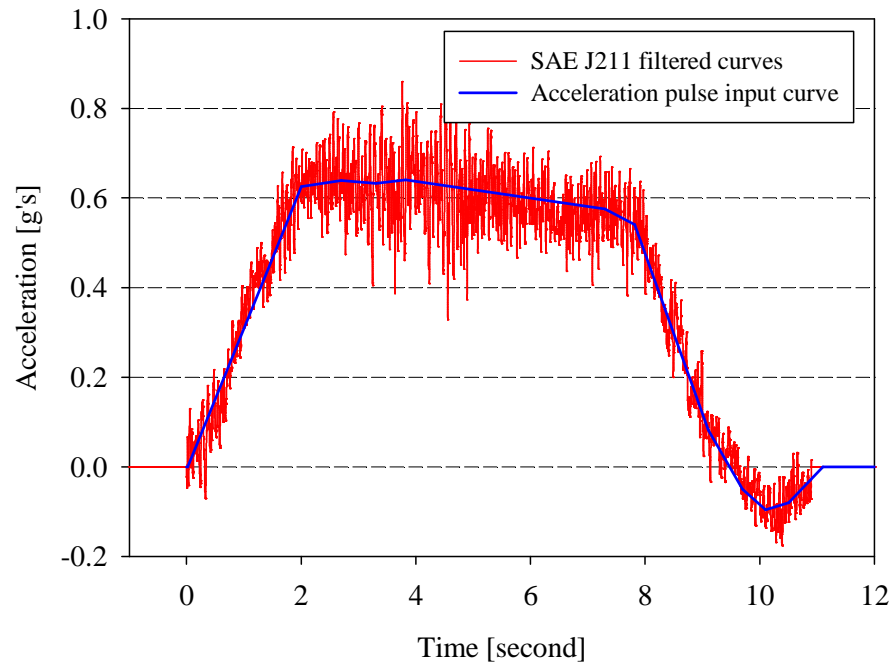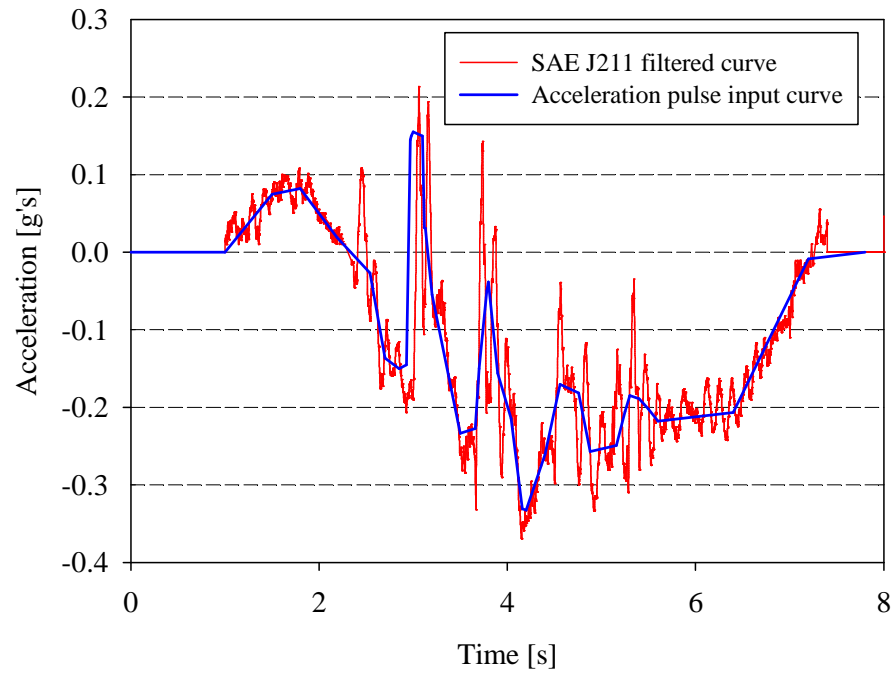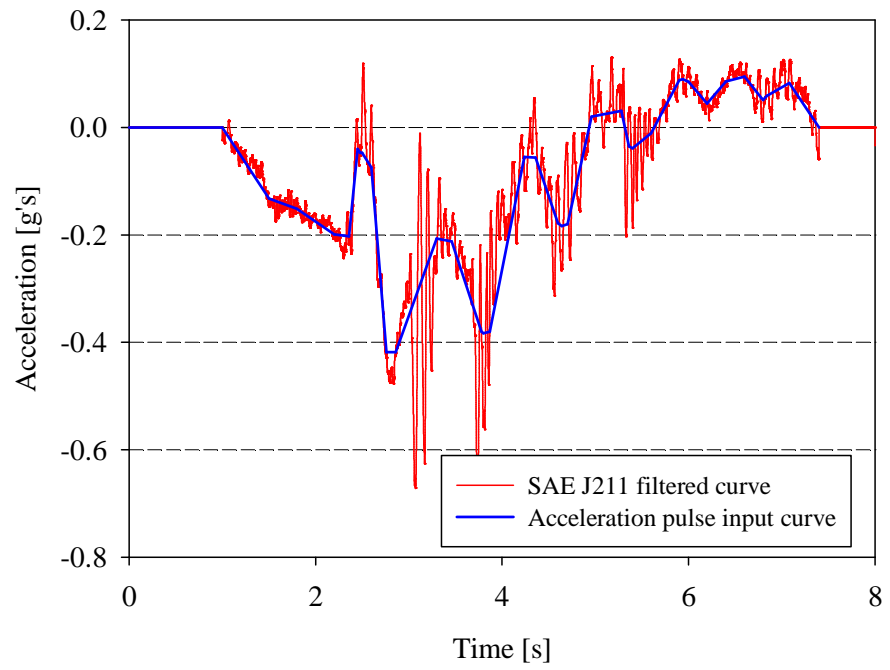
$\text{P4x} \equiv \text{READPRN(} \text{ "p4x.txt"} \quad)$

$\text{P5x} \equiv \text{READPRN(} \text{ "p5x.txt"} \quad)$

$\text{P6x} \equiv \text{READPRN(} \text{ "p6x.txt"} \quad)$

$\text{P4y} \equiv \text{READPRN(} \text{ "p4y.txt"} \quad)$

$\text{P5y} \equiv \text{READPRN(} \text{ "p5y.txt"} \quad)$

$\text{P6y} \equiv \text{READPRN(} \text{ "p6y.txt"} \quad)$

$\text{P4z} \equiv \text{READPRN(} \text{ "p4z.txt"} \quad)$

$\text{P5z} \equiv \text{READPRN(} \text{ "p5z.txt"} \quad)$

$\text{P6z} \equiv \text{READPRN(} \text{ "p6z.txt"} \quad)$

$t := \text{P1x}^{\langle 1 \rangle} \cdot 1000$

$$\text{P12x} := \frac{\text{P1x}^{\langle 2 \rangle} + \text{P2x}^{\langle 2 \rangle}}{2}$$

$$\text{P12y} := \frac{\text{P1y}^{\langle 2 \rangle} + \text{P2y}^{\langle 2 \rangle}}{2}$$

$$\text{P12z} := \frac{\text{P1z}^{\langle 2 \rangle} + \text{P2z}^{\langle 2 \rangle}}{2}$$

$\text{V1x} := \text{P3x}^{\langle 2 \rangle} - \text{P12x}$

$\text{V1y} := \text{P3y}^{\langle 2 \rangle} - \text{P12y}$

$\text{V1z} := \text{P3z}^{\langle 2 \rangle} - \text{P12z}$

$$\text{P45x} := \frac{\text{P4x}^{\langle 2 \rangle} + \text{P5x}^{\langle 2 \rangle}}{2}$$

$$\text{P45y} := \frac{\text{P4y}^{\langle 2 \rangle} + \text{P5y}^{\langle 2 \rangle}}{2}$$

$$\text{P45z} := \frac{\text{P4z}^{\langle 2 \rangle} + \text{P5z}^{\langle 2 \rangle}}{2}$$

$VM1^{\langle 1 \rangle} := V1x \qquad VM1^{\langle 2 \rangle} := V1y \qquad VM1^{\langle 3 \rangle} := V1z$

$VM1 := VM1^{T}$

$VM2^{\langle 1 \rangle} := V2x \qquad VM2^{\langle 2 \rangle} := V2y \qquad VM2^{\langle 3 \rangle} := V2z$

$VM2 := VM2^{T}$

$VM1 := VM1^{T}$

$i := 1, 2 .. \quad rows \ (P1x)$

$$PV_i := \frac{VM1^{\langle i \rangle} \cdot VM2^{\langle i \rangle}}{\left| VM1^{\langle i \rangle} \right| \cdot \left| VM2^{\langle i \rangle} \right|}$$

$$NeckAngle_i := acos\ (PV_i) \cdot \frac{180}{\pi}$$
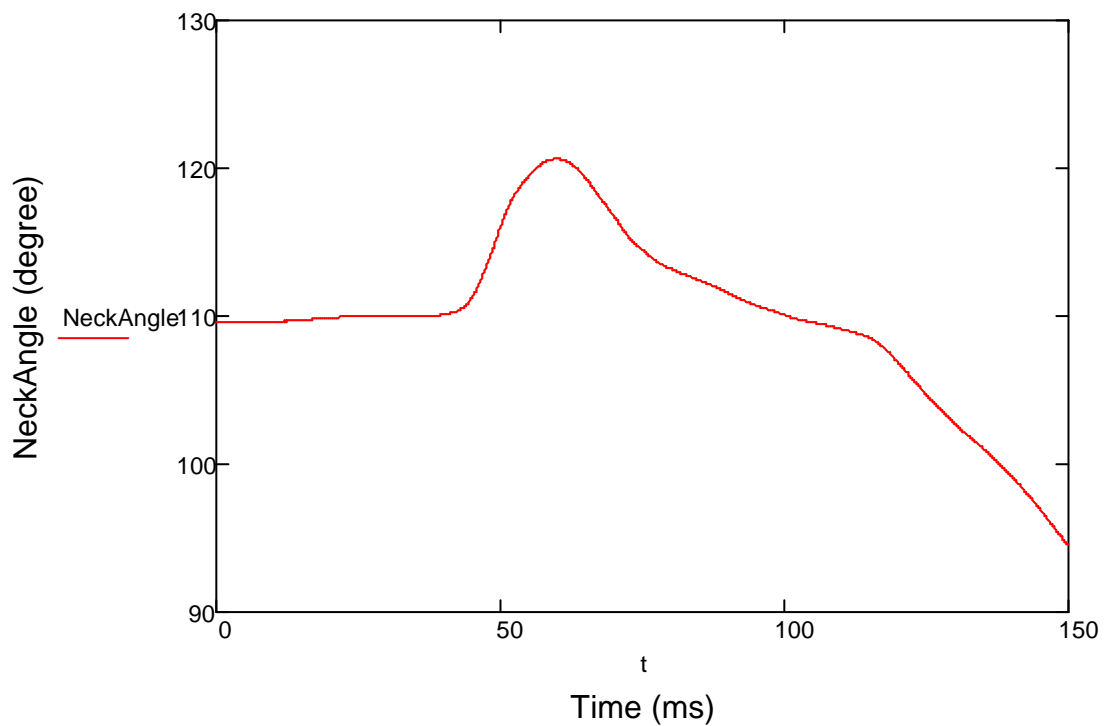
REFERENCES

1. SMARITRISK. (2009). The economic burden of injury in Canada. SMARTRISK: Toronto, ON; 1-5.

2. Transport Canada (2006). Canadian motor vehicle traffic collision statistics: 2005. (TP 3322). Catalogue Number T 45-3/2005.

3. Weber K. (2000). Crash protection for child passenger: A review of best practice. Research Review, 31, 1-27

4. Wegner M.V. and Girasek, D.C. (2003). How readable are child safety seat installation instructions. Pediatrics, 11, 588-591.

5. Pediatrics (1990). Safe transportation of newborns discharged from the hospital. American Academy of Pediatrics Committee on Accident and Posion Prevention. 86:486-7.

6. Walid A.S., Asif K., Jon E.T., Sharon C., Jan S., Beverly G., Linda F., Karen R. (2007). Car seat or car bed for very low birth weight infants at discharge home. J Pediatr 2007;150:224-8.

7. National SAFE KIDS Campaign (NSKC) (2004). Motor vehicle occupant injury fact sheet. Washington (DC): NSKC.

8. Willett L.D., Leuschen M.P., Nelson L.S., Nelson R.M. Jr. (1986). Risk of hypoventilation in premature infants in car seats. J Pediatr. 1986 Aug;109(2):245-8.

9. Bull, M.J. & Stroup, K.B. (1985). Premature infants in car seats. Pediatrics, 75, 336–339.

10. Bull M.J., Engle W.A. (2009). Safe transportation of preterm and low birth weight infants at hospital discharge. Pediatrics. 2009;123:1424-1429

11. Bass J.L., Mehta K.A., Camar J. (1993). Monitoring premature infants in car seats: implementing the American Academy of Pediatrics policy in a community hospital. Pediatrics. 1993;91:1137-41.

12. Willett L.D., Leuschen M.P., Nelson L.S., Nelson R.M. Jr. (1989). Ventilatory changes in convalescent infants positioned in car seats. J Pediatr. 1989;115:451-5.

13. Ojadi V.C., Petrova A., Mehta R., Hegyi T (2005). Risk of cardio-respiratory abnormalities in preterm infants placed in car seats: a cross-sectional study. BMC Pediatr. 2005;5:28.

14. Final rule (2003). Federal Motor Vehicle Safety Standards 213: Child Restraint Systems. 49 CFR Part 571, Docket No. HGTSA-03-15351, Federal Register, Vol. 68, No. 121, pp. 1-40.

15. Transport Canada (1998). Canadian Motor Vehicle Safety Standard No. 213: Child Restraint Systems. Canada Gazette Part II, Vol. 132, No. 7.

16. Bull MJ, Weber K, Stroup KB. Automotive restraint systems for premature infants. J Pediatr. 1988;112:385-8.

17. American Academy of Pediatrics Committee on Injury and Poison Prevention and Committee on Fetus and Newborn (1996). Safe transportation of premature and low birth weight infants. Pediatrics. 1996; 97: 758-60.

18. Bull M., Agran P., Larague D., Pollack S.H., Smith G.A., Spivak H.R., Tenenbein M., Tully S.B., Brenner R.A., Bryn S., Neverman C., Schieber R.A., Stanwick R., Tinsworth D., Tully W.P., Garcia V., Katcher M.L. (1999). American Academy of

Pediatrics Committee on Injury and Poison Prevention. Transporting children with special health care needs. Pediatrics. 1999;104:988-92.

19. Kinane T.B. et al. (2006). Comparison of respiratory physiologic features when infants are placed in car safety seats or car beds. Pediatrics. 2006;118:522-527.

20. National Highway Traffic Safety Administration. (2006). Traffic safety facts 2006 (DOT HS 810 631 pp. 1-224). U.S. Department of Transportation.

21. Bondy M., Chen X., and Altenhof W. (2011). Aspects of child safety in automobiles. Engineering Dimensions. 2011 July/August;53-55.

22. Merchant JR et al. (2001). Respiratory instability of term and near-term healthy newborn infants in car safety seats. Pediatrics. 2001;108:647-652.

23. Bass JL, Mehta KA. (1995). Oxygen desaturation of selected term infants in car seats. Pediatrics. 1995;96:288-290.

24. Tonkin S.L. et al. (2003). Simple Car Seat Insert to Prevent upper airway narrowing in preterm infants: A pilot study. Pediatrics. 2003;112:907-913.

25. Thach BT, Stark AR. (1976). Spontaneous neck flexion and airway obstruction during apneic spells in preterm infants. J Pediatr. 1976;86:982-985.

26. Wilson S.L. et al. (1979). Upper airway patency in the human infant: influence of airway pressure and posture. J. Appl. Physiol: Rcspirat. Environ. Exercis Physiol. 48(3):500-504.

27. Du Bois P., Chou C.C., Fileta B.B., Khalil T.B., King A.I., Mahmood H.F., Mrtz H.J., Wismans, J. (2004). Vehicle crashworthiness and occupant protection, American Iron and Steel Institute, Southfield, Michigan, pp. 1-388.

28. De Jager K., Van Ratingen M., Lesire, P., Guillemot H., Pastor C., Schnottale B., Tejera G., Lepretre J. Assessing new child dummies and criteria for child occupant protection in frontal impact. EEVC WG12&WG18. 05-0157

29. Tanya K., Altenhof W., Howard A., Rasico J., Zhu F. (2008). Methods to mitigate injuries to toddlers in a vehicle crash. Accident Analysis & Prevention. Volume 40, Issue 6, pp. 1880-1892.

30. American Standard of Testing Methods. (2004). Standard test methods for tensile properties of plastics [Metric]. (Designation: D638M). Annual book of ASTM standards, Philadelphia, PA, USA.

31. ASTM international (2005). Standard test methods for flexible cellular materials – slab, bonded, and molded urethane foams.

32. Oberkampf W.L., Trucano T.G (2002). Verification and validation in computational fluid dynamics. Progress in Aerospace Sciences 38 (2002)209 – 272.

33. Jun Ouyang et al. (2005). Biomechanical assessment of the pediatric cervical spine under bending and tensile loading. SPINE. Volume 20, Number 24, pp. E716-E723.

34. DeSantis-Klinich K. et al. (1996). Techniques for developing child dummy protection reference values. NHTSA Event Report, Docket Submission # 74-14 Notice 97 Item 069.

35. Eppinger R. et al. (1999). Development of improved injury criteria for the assessment of advanced automotive restraint systems – II. National Highway and Traffic Safety Administration.

36. Livermore software technology corporation (2003). LS-Dyna keyword user's manual. April 2003, Version 970. Livermore Software Technology Corporation.

37. J. Luck, R. Nightingale, A. Loyd, M. Prange, A. Dibb, Y. Song, L. Fronheiser, B. Myers. Tensile mechanical properties of perinatal and pediatric PMHS osteoligamentous cervical spine. Stapp Car Crash Journal. Vol 52, 2008.

38. Livermore software technology corporation (2006). LS-Dyna theory manual. Livermore Software Technology Corporation.

39. Mathcad user's guide with reference manual (2001). Match Soft Engineering & Education, Inc.

40. Q0 user Manual (2008). First Technology Safety Systems, Plymouth, Michigan.

41. Model 3711B1110G Series 371x DC Response Accelerometers Installation and Operating Manual.

VITA AUCTORIS

Mr. Xilin Chen was born in December 1986 in Shanghai, China to Mr. Liang Chen. His father is Mr. Liang Chen. His mother is Mrs. Wenqing Ye. He has one younger brother, Zhiqi Chen (b. 1999). He graduated from Lu Wan High School, Shanghai in 2005. From there he went to University of Windsor where he obtained a Bachelors of Applied Science in Mechanical Engineering with Automotive/co-op option in 2009. He is currently a candidate for the Master's degree in Mechanical Engineering at University of Windsor and hopes to graduate in Fall 2011.